Transient Analysis of a Hypergolic Bipropellant Thruster using Discrete Phase Modelling and Finite Rate Chemistry

Performance and Flow Characterisation for Upper Stage Applications

Master Thesis

Maximilian Pfohl

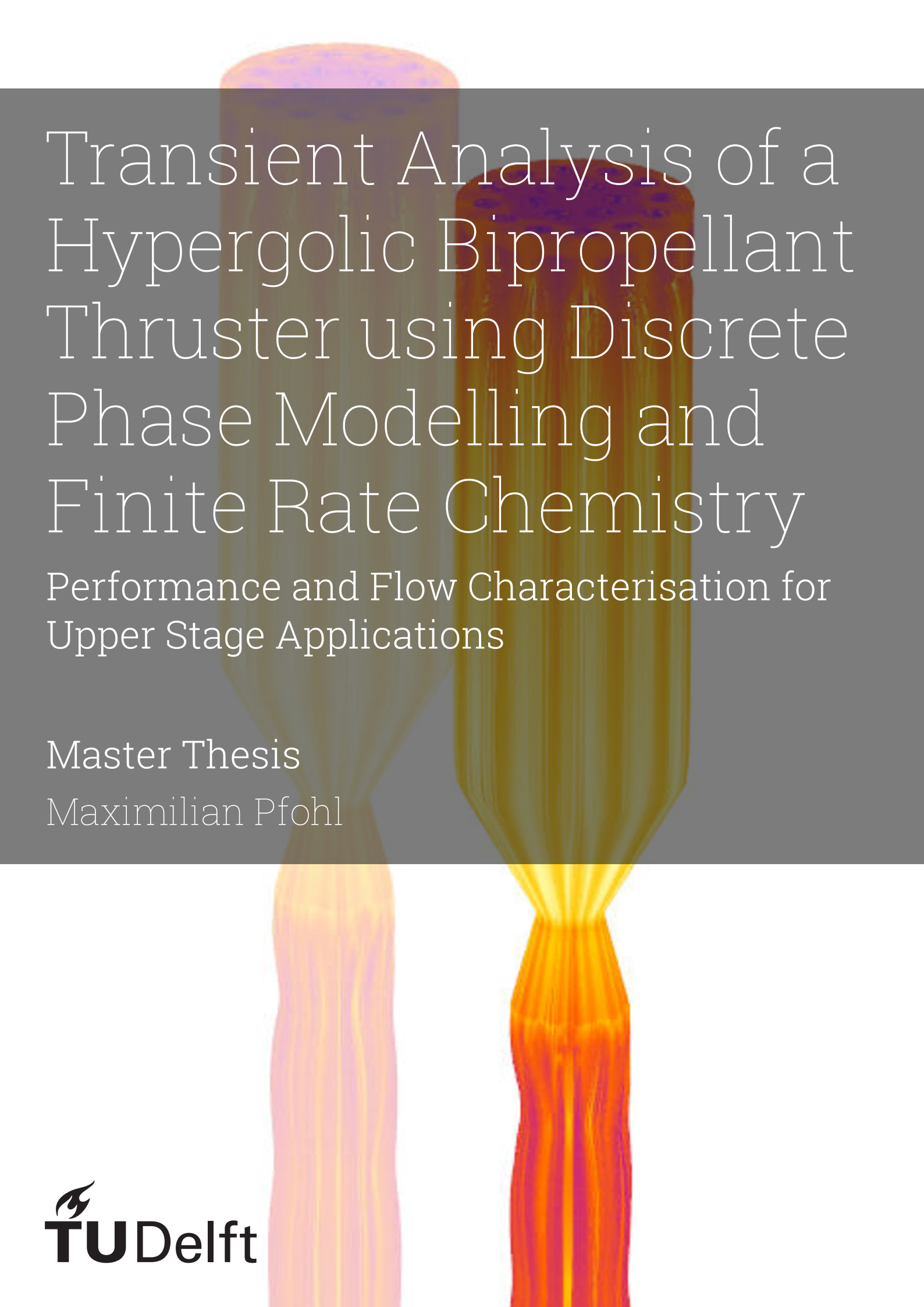

TU Delft

Transient Analysis of a Hypergolic Bipropellant Thruster using Discrete Phase Modelling and Finite Rate Chemistry

Performance and Flow Characterisation for Upper Stage Applications

by

Maximilian Pfohl

to obtain the degree of Master of Science

at the Delft University of Technology,

to be defended publicly on Tuesday, October 1, 2024 at 2pm.

Project duration:	January 22, 2024 – September 17, 2024	
Thesis committee:	Prof. Dr. L.L.A. Vermeersen	TU Delft, Chair
	Prof. Dr. B.V.S. Jyoti	TU Delft, Supervisor
	Dr. P. Jindal	TU Delft, Supervisor
	M.Ş. Uludağ	TU Delft, External Examiner

An electronic version of this thesis is available at https://repository.tudelft.nl/.

TU Delft

Preface

The last two years in Delft have been an amazing experience. While I came here to study space engineering, I have learned so much, not just about this field, but also about many other disciplines — although electronics will forever remain a mystery to me. I met people with vastly different and inspiring background stories, had the chance to work on exciting projects and to visit different countries. I really hope to continue on this path in the future.

I would like to thank my thesis supervisors, Botchu Vara Siva Jyoti and Prakhar Jindal, who entrusted me with this work despite my initially very limited knowledge of fluid dynamics and combustion when they first discussed this project with me about a year ago; who guided me throughout the last eight months, and who patiently addressed my concerns regarding pretty much everything.

Delft would not have been the same without my friends. They made me feel at home, struggled alongside me through coursework and thesis writing, and most importantly, shared the breaks from studying, making them so much more enjoyable.

Mein größter Dank gilt meinen Eltern und meinem Bruder, die mich schon immer in allen meinen Vorhaben unterstützen, mich ermutigen, Ambitionen zu verwirklichen, und Neues zu wagen.

I would like to acknowledge the use of computational resources of the DelftBlue supercomputer, provided by Delft High Performance Computing Centre (`https://www.tudelft.nl/dhpc`). *SolvGE is recognised for providing the design of the thruster used in this thesis.*

Maximilian Pfohl
Delft, October 2024

Abstract

With the space industry growing, environmental considerations become increasingly important, especially with respect to the propulsion systems used to launch satellites into space and control their position in orbit. Since traditional satellite propellants are highly toxic, there is an increased demand for green, i.e., environmentally friendly, substitutes like hydrogen peroxide.

This work explored the modelling of hypergolic bi-liquid thrusters in the framework of the Greenlam project, which aims to develop a $100N$ hydrogen peroxide kerosene thruster. While previous works were either experimental or focused on staged H_2O_2–RP-1 engines with a catalyst bed, this thesis investigated a numerical approach and focused on unstaged engines, aiming to identify and validate models viable to simulate the decomposition of hydrogen peroxide and subsequent combustion with kerosene with the aid of a catalyst.

Transient three-dimensional simulations were performed. k-ω SST, the Peng Robinson real-gas equation of state and Species Transport with Finite Rate chemistry were employed to model turbulence, gas properties and reactions, respectively. The effect of the catalyst was represented by adapting the Arrhenius rate parameters. Propellants were injected using the Discrete Phase Model. The Eulerian model was shown not to be suitable to simulate the propellant injection and atomisation.

A coaxial, an impinging-jet and a pintle injector were considered. Simulations with the coaxial injector showed good agreement with data obtained from CEA and with other rocket engines. Simulations with the impinging-jet and pintle injector failed to capture droplet impingement and consequent atomisation and thus could not be validated.

Both stoichiometric and fuel-rich propellant mixtures and H_2O_2 concentrations of 95% and 98% were simulated. Thrust was between 62 and $63N$ under sea-level conditions, equivalent to 103 to $105N$ in vacuum and hence approximately $3-5\%$ higher than anticipated. Chamber temperature reached up to $2763K$. Chamber pressure was $7.6bar$. The stoichiometric mixtures showed higher thrust output, higher chamber temperature and higher wall temperature than the fuel-rich mixtures. The higher concentrations led to higher chamber and wall temperatures. Analysing the kerosene mass fraction in the exhaust showed that in any case at least 9% of the injected kerosene was ejected unburnt due to a lack of mixing, and most of the additional kerosene in the fuel-rich mixtures was also simply ejected. The chamber walls reached temperatures of up to $3271K$, about $500K$ higher than bearable by the material. While the coaxial injector was shown to be a cause for the high wall temperatures due to unfavourable propellant distribution, an adiabatic wall boundary condition was assumed which likely also led to an overestimation of the temperature.

A set of models applicable for simulating hypergolic bi-liquid rocket engines was found and validated. More work is required in terms of injector design and modelling, confirmation of reaction rate parameters and wall modelling.

Contents

List of Figures

List of Tables

Nomenclature

Abbreviations

Abbreviation	Definition
CEA	NASA Chemical Equilibrium with Applications
CFD	Computational Fluid Dynamics
DLR	German Aerospace Centre
DNS	Direct Numerical Simulation
EBU	Eddy Break-Up
EU	European Union
FDM	Finite Difference Method
FVM	Finite Volume Method
HTP	High-Test-Peroxide
IDT	Ignition Delay Time
KAIST	Korea Advanced Institute of Science and Technology
LEM	Linear Eddy Model
LEO	Low Earth Orbit
LES	Large Eddy Simulation
MMH	Monomethylhydrazine
NTO	Nitrogen Tetroxide
O/F	Oxidiser-to-Fuel-Ratio
OMS	Orbital Maneuvering System
PDF	Probability Density Function
RANS	Reynolds Averaged Navier Stokes Equations
RCS	Reaction Control System
SKE	Standard k-ϵ
SST	(k-ω) Shear-Stress Transport
UHTCMC	Ultra High Temperature Ceramic Matrix Composite
VOF	Volume of Fluid

Symbols

Symbol	Definition	Unit
A	Pre-Exponential Factor	[K$^{-\beta}$]
A_t	Throat Diameter	[m^2]
$\mathbf{B}$	Body Forces per Unit Volume	[$kg\ m^{-2}\ s^{-2}$]
D	Droplet Diameter	[m]

Symbol	Definition	Unit
c	Mass Fraction	[$-$]
c^*	Characteristic Velocity	[ms^{-1}]
D_t	Throat Diameter	[m]
D_c	Local Chamber Diameter	[m]
E_A	Activation Energy	[J]
F	(Thrust) Force	[N]
g_0	Standard Gravitational Acceleration	[$m\ s^{-2}$]
h	Convective Heat Transfer Coefficient	[$W\ m^{-2}K^{-2}$]
I_{sp}	Specific Impulse	[s]
$I_{sp,sl}$	Specific Impulse at sea-level	[s]
$I_{sp,vac}$	Specific Impulse in vacuum	[s]
k	Turbulent Kinetic Energy	[$J\ kg^{-1}$]
k_r	Forward Rate Constant	[$-$]
l	Characteristic Length	[m]
M	Molar Mass	[$kg\ mol^{-1}$]
$\dot{m}$	(Total) Mass Flow Rate	[$kg\ s^{-1}$]
$\dot{m}_{fuel}$	Fuel Mass Flow Rate	[$kg\ s^{-1}$]
$\dot{m}_{ox}$	Oxidiser Mass Flow Rate	[$kg\ s^{-1}$]
Ma	Mach Number	[$-$]
Ma_e	Mach Number at Nozzle Exit	[$-$]
p	(Static) Pressure	[Pa]
p_0	Total Pressure	[Pa]
p_a	Ambient or Atmospheric Pressure	[Pa]
p_c	Chamber Pressure	[Pa]
p_e	Nozzle Exit Pressure	[Pa]
Pr	Prandtl Number	[$-$]
p_{sat}	Saturation Pressure	[Pa]
r	Radius	[m]
R	Universal Gas Constant	[$J\ mol^{-1}K^{-1}$]
Re	Reynolds Number	[$-$]
T	Temperature	[K]
T_0	Stagnation Temperature	[K]
T_c	Chamber Temperature	[K]
T_w	Wall Temperature	[K]
v	Velocity (Magnitude)	[$m\ s^{-1}$]
v_e	Nozzle Exit Velocity	[$m\ s^{-1}$]
$\mathbf{v}$	Velocity (Vector)	[$m\ s^{-1}$]
We	Weber Number	[$-$]
y^+	y-plus	[$-$]
α	HTP Concentration	[$-$]
β	Temperature Exponent	[$-$]
ϵ	Turbulent Kinetic Energy Dissipation Rate	[$J\ kg^{-1}s^{-1}$]
μ	Dynamic Viscosity	[$Pa\ s$]

Symbol	Definition	Unit
ρ	Density	[$kg\ m^{-3}$]
Σ	Sum	[-]
σ	Surface Tension	[$N\ m^{-1}$]
τ	Shear Stress	[Pa]
Φ	Equivalence Ratio	[$-$]
φ	Heat Transfer Correction Factor	[$-$]
ω	Specific Turbulent Kinetic Energy Dissipation Rate	[s^{-1}]

1

Introduction

1.1. Historic Background

Humans have always dreamed of expanding their frontiers and exploring space. Rockets were first proposed in the 19th century to enable this exploration. In the early 20th century, rocket technology was advanced by researchers like Tsiolkovsky, Goddard and Oberth, to name a few. During the 1930s, larger rocket programmes with militarist intentions were started to support the Nazi warfare. The Space Race during the Cold War between the United States and the Soviet Union led to a surge in rocketry development, culminating with the first human in space in 1961 and the first humans landing on the moon in 1969. A few years after the moon landing, the two countries started collaborating, in 1993, plans for a joint space station were announced, and five years later, the first module of the International Space Station was launched. In 2008, the first rocket developed by a private company was launched to space and orbited Earth: SpaceX's Falcon 1. Since then, spaceflight has become increasingly commercial, with space agencies sourcing out more and more development and launches to private companies. The number of orbital launches has increased more than threefold since 2008 (Figure 1.1) [1].

This so-called "New Space" industry keeps growing. Being commercially rather than institutionally driven, it is defined by comparatively low regulations in the development phase, more frequent testing and shorter development times, thus keeping costs low. With this, more and more smaller companies enter the market. There is a trend towards smaller systems like cubesats, cubic satellites with an edge length of $10cm$, and even smaller "PocketQubes" with half the edge length have been launched since their introduction in 2009 [2], being more affordable per unit and requiring less initial investment, such that even student teams can launch a satellite. These miniaturised systems also enable the construction of distributed systems, covering locations on the ground from space more frequently or offering more communication nodes in space. Hence, the industry continues to grow.

In recent years, environmental considerations in space flight applications have become more and more important and started being included as central design objectives. Especially the Global Warming driven by combustion products, but also the toxicity to flora and fauna inherent to many propellants, drive the need for so-called *Green Propellants*, propellants with a lower carbon footprint and lower

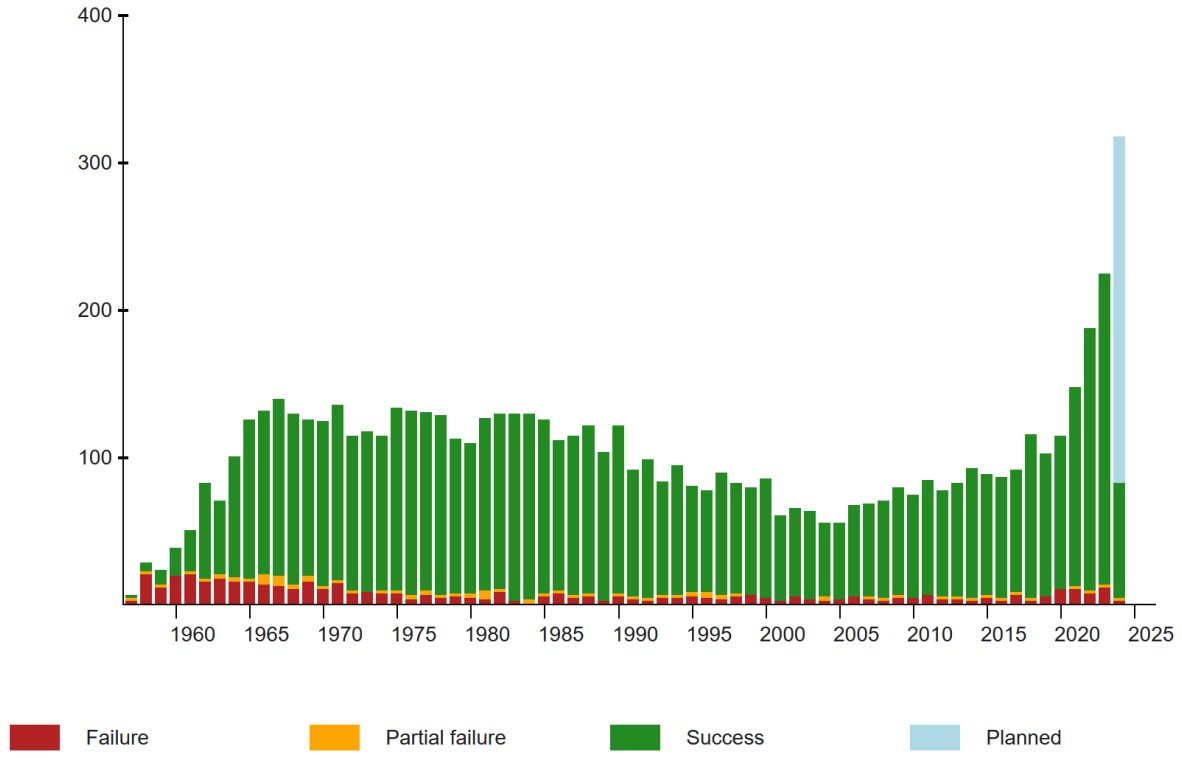

Figure 1.1: Orbital launches per year from 1957 to 2024 [1]

toxicity compared to conventional propellants.

Rocket engines for upper stages and especially for in-space applications require high-performance propellants with good storability. Although (semi-)cryogenic propellant combinations like kerosene and liquid oxygen or liquid hydrogen and liquid oxygen can deliver that performance, keeping them in a liquid state requires permanent cooling and thus a lot of energy, making them unsuitable candidates for longer missions.

Hydrazine based propellants, most commonly monomethylhydrazine (MMH) or unsymmetrical dimethylhydrazine (UDMH) as fuel with nitrous oxide (NTO) as oxidiser address this issue, being storable even at ambient temperatures and pressures. This propellant combination has another advantage: hypergolicity. Upon contact with each other, the propellants ignite without the need for a dedicated ignition system to deliver the initial activation energy. This is again especially useful for upper stage and on-orbit engines, where often several burns and thus several ignitions are required. The downside of hydrazine is its high toxicity, which is why a lot of research is done to find suitable alternatives that bring the advantages of propellants like hydrazine (storability, hypergolicity, performance) while being environmentally friendly.

Hydrogen peroxide (H_2O_2), usually used in a solution with water, is one such propellant. It can be decomposed exothermically into water and oxygen and is used both as monopropellant and as oxidiser in liquid rocket engines. Hydrogen peroxide has been researched as monopropellant for over 60 years, mainly for use in reaction control systems, but also as oxidiser primarily in combination with kerosene [3]. Engines were developed in the United States, Russia, South Korea and Europe, for example the Gamma engine for the Black Arrow launch vehicle and the Black Knight missile. Currently, the UK based company Skyrora develops a hydrogen peroxide-kerosene engine [4].

1.2. Research Motivation

There is an ongoing project named *Greenlam*, supported by the EU and conducted within the Space Systems Engineering Group of the Faculty of Aerospace Engineering at the Delft University of Technology, which aims to develop a new hypergolic bipropellant thruster. The engine shall achieve $1 - 100N$ thrust, relying on green propellants, i.e., hydrogen peroxide and kerosene, and using Ultra-High Temperature Ceramic Matrix Composites (UHTCMC) for the chamber structure. The system shall be optimised for a lightweight, environmentally friendly and cost efficient design, manufacturing and operation while maintaining high performance and improved reliability compared to other systems. The project shall combine multi-physics numerical simulations with experiments to eventually be able to test a prototype. The findings of this research are meant to directly address the European Green Deal and contribute to more sustainable spaceflight [5]. The aim of this thesis is to predict and characterise the fluid flow and combustion in this engine with a new design and new propellant combination by means of simulation.

1.3. Report Outline

Subsequent to the *Introduction* (Chapter 1), this report is structured into the chapters *Literature Review* (Chapter 2), *Research Plan & Methodology* (Chapter 3), *Modelling & Validation* (Chapter 4), *Results & Discussion* (Chapter 5) and *Conclusion* (Chapter 6).

In Chapter 2, the current state of the art of rocket propulsion in general and hydrogen peroxide in rocket engines in particular are described, as well as ways of simulating the flow and the combustion in rocket engines.

From this, a research plan is derived before introducing the methodology in Chapter 3. Consequently, Chapter 4 describes the evaluation, selection and validation of different models, before the final simulations and their results are described and discussed in Chapter 5.

Chapter 6 provides a summary of the findings of this report, discusses their relevance and lines out sensible steps for future research.

2

Literature Review

This chapter provides the background for the research performed in this thesis and introduces relevant concepts, before identifying a research gap, based on which the subsequent research was conducted.

2.1. Liquid Rocket Engines - State of the Art

2.1.1. Fundamentals of Rocket Propulsion

Thermo-chemical rocket propulsion combines various physical and chemical problems. The equation for thrust (Equation 2.1) and Tsiolkovsky's rocket equation (Equation 2.2) [6] describe the fundamental working principle of a rocket engine.

$$F = \dot{m}\ v_e \tag{2.1}$$

$$\Delta v = v_e\ ln\frac{m_{str} + m_{prop}}{m_{str}} = I_{sp}\ g_0\ ln\frac{m_{str} + m_{prop}}{m_{str}} \tag{2.2}$$

Propellant mass is expelled on one side of a rocket with a certain force, or thrust, F, causing the rocket to move in the opposite direction. The higher the exhaust (or exit) velocity v_e and the higher the ratio of propellant mass to structural mass $\frac{m_{prop}}{m_{str}}$, the higher the acceleration of the propelled object, e.g., a rocket, and its gain in velocity Δv. The exhaust velocity can also be expressed as the product of the specific impulse I_{sp} and the standard gravitational acceleration $g_0 = 9.80665\frac{m}{s^2}$. The specific impulse describes how much impulse or momentum can be gained per unit propellant mass, normalised by the standard gravitational acceleration. This quantity depends primarily on the propellant composition, but also engine design parameters like the chamber pressure, and is frequently used as a measure of efficiency of a propulsion system [7].

2.1.2. Rocket Engine Propellants

There are different ways of obtaining the necessary exhaust velocity. Simple cold gas thrusters store a gas under high pressure and, by releasing it through a convergent-divergent nozzle, converting the pressure to velocity according to Bernoulli's equation (Equation 2.3). The standard form of the equation is only viable for incompressible, inviscid and low-velocity flows. For compressible flows, the ratio of specific heats needs to be considered (Equation 2.4) [8].

$$p_0 = p + \frac{1}{2}\rho v^2 \tag{2.3}$$

$$\frac{v^2}{2} + \frac{\gamma}{\gamma - 1}\frac{p}{\rho} = \frac{\gamma}{\gamma - 1}\frac{p_0}{\rho_0} \tag{2.4}$$

For high velocities, further considerations need to be made depending on the Mach number of the flow, which will not be elaborated here.

In chemical rocket engines, propellants, usually a fuel and an oxidiser, react with each other exothermically, converting their chemical energy into pressure and then into velocity. Rocket engines can be categorised by the number of propellants they use, i.e., most commonly mono-propellant or bi-propellant, or by the state of propellant they use, either gaseous, liquid, solid or hybrid, the latter combining propellants of different state. Gaseous mono-propellant thrusters are usually used for attitude control, whereas bi-liquid engines provide the highest performance. Table 2.1 [9] lists a few rockets and their engines, including the propellant used and the specific impulse as performance metric. It shows that the combination of liquid oxygen and liquid hydrogen has the highest performance per propellant mass. However, storability of this propellant combination is difficult. The propellants need to be cooled constantly to stay liquid and the low density of hydrogen leads to the need for the tank to be comparatively heavy to sustain high pressures. Hence, another performance metric often used instead of specific impulse is the density specific impulse ρI_{sp}, i.e., the product of average propellant density and propellant specific impulse.

Table 2.1: Propellant specification and performance of rocket engines [9]

Rocket	Stage	Engines	Propellant	Specific impulse
Atlas/Centaur	0	Rocketdyne YLR89-NA7 (x2)	LOX/RP-1	259 s sl/292 s vac
(1962)	1	Rocketdyne YLR105-NA7	LOX/RP-1	220 s sl/309 s vac
	2	P&WRL-10A-3-3 (x2)	LOX/LH 2	444 s vac
Titan II	1	Aerojet LR-87-AJ-5 (x2)	NTO/Aerozine 50	259 s sl/285 s vac
(1964)	2	Aerojet LR-91-AJ-5	NTO/Aerozine 50	312 s vac
Saturn V	1	Rocketdyne F-1 (x5)	LOX/RP-1	265 s sl/304 s vac
(1967)	2	Rocketdyne J-2 (x5)	LOX/LH 2	424 s vac
	3	Rocketdyne J-2	LOX/LH 2	424 s vac
Space Shuttle	0	Thiokol SRB (x2)	PBAN solid	242 s sl/268 s vac
(1981)	1	Rocketdyne SSME (x3)	LOX/LH 2	363 s sl/453 s vac
	OMS	Aerojet OMS (x2)	NTO/MMH	313 s vac
	RCS	Kaiser Marquardt R-40 & R-1E	NTO/MMH	280 s vac
Delta II	0	Castor 4A (x9)	HTPB solid	238 s sl/266 s vac
(1989)	1	Rocketdyne RS-27	LOX/RP-1	264 s sl/295 s vac
	2	Aerojet AJ10-118K	NTO/Aerozine 50	320 s vac

Liquid rocket engines cover a wide range of applications and performance levels. They are used on the first stages of launch vehicles, providing very high thrust for a comparatively short duration at sea level and in the lower atmosphere; on upper stages, delivering lower thrust over longer durations and potentially throughout seperate firings; on launch escape systems, where near instantaneous and high thrust is required to safely evacuate astronauts; or on tes for repeated low thrust and low duration firings to control attitude and orbit. Depending on the application, different engines and propellants are required. Table 2.2 [10] provides a comparison between high thrust (boost propulsion) and low thrust (auxiliary propulsion) engines.

Table 2.2: Comparison of high thrust (boost) and low thrust (auxiliary) propulsion systems, taken from [10]

Purpose/Feature	Boost Propulsion	Auxiliary Propulsion
Mission	Impart significant velocity to propel a vehicle along its flight path	Attitude control, minor space maneuvers, trajectory corrections, orbit maintenance
Applications	Booster stage and upper stages of launch vehicles, large missiles	Spacecraft, satellites, top stage of antiballistic missile, space rendezvous
Total impulse	High	Low
Number of thrust chambers per engine	Usually 1; sometimes 4, 3, or 2	Between 4 and 24
Thrust level per thrust chamber	High; 4,500 N up to 7,900,000 N	Small; 0.001 up to 4,500 N
Feed system, typical	Mostly turbopump type; occasionally pressurized feed system for smaller thrusts	Pressurized feed system with high-pressure gas supply
Tank pressure range	0.138–0.379 MPa	0.689–17.23 MPa
Most common cooling method	Propellant cooled	Radiation cooled
Propellants	Cryogenic and storable liquids	Storable liquids, monopropellants, and/or stored cold gas
Chamber pressure	2.4–21 MPa	0.14–2.1 MPa
Number of starts during a single mission	Usually no restart; sometimes one, but up to four in some cases	Several thousand starts for some space missions
Cumulative duration of firing	Up to a few minutes	Up to several hours
Shortest firing duration	Typically 5–40 sec	0.02 sec typical for pulsing small thrusters
Time elapsed to reach full thrust	Up to several seconds	Usually very fast, 0.004–0.080 sec
Life in space	Hours, days, or months	Up to 15 years or more in space

As already discussed in Chapter 1, there is a trend towards using more environmentally friendly propellants, regardless of application. This is both in terms of greenhouse gas emissions, air pollution and toxicity.

2.1.3. Hydrogen Peroxide in Liquid Rocket Engines

On orbit, i.e., on launch vehicle upper stages or on satellites, the ability to ignite the engine multiple times and the long-term storability of the propellant are critical. For that reason, the propellant combination MMH and NTO is commonly used, being hypergolic, i.e., igniting upon contact with each other and being storable at ambient temperature and pressure, whereas the propellant combination kerosene and liquid oxygen, commonly used on first stages, has a higher performance but requires an ignition system and needs to be constantly cooled for the oxygen not to evaporate.

Because of its favourable properties (see below), hydrogen peroxide can be used to replace the toxic MMH/NTO:

- Under specific conditions (see Section 2.1.3), it is hypergolic, making ignition systems obsolete.
- It is liquid at ambient conditions, i.e., it is easily storable.

- It is considered green, i.e., it is significantly less toxic compared to hydrazine and it emits less carbon dioxide compared to an engine using liquid oxygen.
- Its performance is similar to that of hydrazine (see Table 2.4)

Decomposition of Hydrogen Peroxide

Hydrogen peroxide is usually stored in a solution with water. Commercially available concentrations are around 3-30%, used for cleaning and disinfection.

At ambient conditions, hydrogen peroxide decomposes exothermically into water and oxygen (Equation 2.5). With molar masses of hydrogen peroxide, water and oxygen of $M_{H_2O_2} \approx 34g/mol$, $M_{H_2O} \approx 18g/mol$ and $M_{O_2} \approx 32g/mol$, respectively, this results in a decomposition by mass as per Equation 2.6.

$$H_2O_2 \rightarrow H_2O + 0.5\ O_2 \tag{2.5}$$

$$H_2O_2 \rightarrow 0.53\ H_2O + 0.47\ O_2 \tag{2.6}$$

For hydrogen peroxide solutions at concentrations above approximately $74wt\%$ (the rest being water and sometimes additives), the decomposition reaction heat becomes sufficient to vaporise all liquid [11]. In solutions with even higher concentrations, above 85% - referred to as High-Test-Peroxide (HTP) - it is thus used as a monopropellant. HTP can also be used as oxidiser in bipropellant systems. With many fuels, it is hypergolic, i.e., ignites upon contact. Hypergolicity has the advantage that an ignition system becomes obsolete. Especially in upper stage and on-orbit missions where several engine ignitions are necessary, this significantly improves reliability and decreases complexity of the propulsion system.

To speed up the decomposition reaction, or, in a rocket engine, reduce the ignition delay time, a catalyst can be added. The role of the catalyst is to lower the activation energy of the hydrogen peroxide decomposition. Table 2.3 shows reaction parameters from experiments and theoretical derivations of H_2O_2 decomposition with and without catalyst. Inserting, for example, the values given by [12] into the Arrhenius equation (Equation 2.19, Section 2.2.2) shows an increase in reaction rate by a factor of 1073 when adding a catalyst, in this case MnO_2. Other organic or non-organic (metallic) catalysts may be used.

The reaction given in Equation 2.5 is usually heterogenous, i.e., includes a phase transition, opposed to a homogeneous reaction which happens within a single phase. For example, the hydrogen peroxide might be liquid initially and decompose into gaseous oxygen and water. This may become clearer when considering that this reaction is a useful model, but a strong simplification: In reality, there appear to be several quasi-simultaneous physical and chemical reactions, the interaction of which is not exactly clear. Over the last years, catalytic decomposition for application in rocket engines, which is usually considered to be heterogeneous, has been strongly researched. Adding a catalyst or other materials not only speeds up decomposition but also increases the number of possible reactions, all depending on ambient conditions, concentration and, if applicable, the properties of the catalyst. An intermediate reaction might release energy that leads to vaporisation, before the subsequent reaction happens.

In [17], decomposition with manganese oxide is investigated and a non-comprehensive list of possible reaction steps is provided (Figure 2.1).

Table 2.3: Arrhenius reaction parameters for H_2O_2 decomposition

Catalyst	Phase	Pre-Exponential Factor A [s^-1]	Activation Energy E_A [$kJ\ mol^-1$]	Source
MnO_2	liquid	N.A.	58	[12]
-	liquid	N.A.	75	[12]
TiO_2	liquid	18	37	[13]
Y_2O_3	liquid	6.23E+03	47	[13]
Fe_2O_3	liquid	2.2E+03	47	[14]
CeO_2	liquid	1.40E+03	40	[14]
CuO	liquid	3.50E+09	76	[14]
HfO_2	liquid	1.10E+07	60	[14]
Gd_2O_3	liquid	3.40E+06	63	[14]
-	supercritical	2.51E+13	180	[15]
-	supercritical	7.94E+14	209	[15]
-	vapour	1.00E+13	201	[15]
-	vapour	3.16E+13	207	[15]
-	vapour	3.16E+14	203	[15]
-	liquid	3.98E+03	49	[15]
-	liquid	6.31E+05	71	[15]
-	liquid	4.00E+03	49	[15]
Catalyst bed (unspecified)	liquid	1.00E+08	52.5	[16]

$$H_2O_2 + [\equiv M\text{-}O]OH \rightarrow [\equiv M\text{-}O]OH\text{–}H_2O_2$$
$$[\equiv M\text{-}O]OH\text{–}H_2O_2 \leftrightarrow [\equiv M\text{-}O] + {}^{\cdot}OOH + H_2O$$
$$[\equiv M\text{-}O] + {}^{\cdot}OOH \rightarrow [\equiv M\text{-}O]H + O_2\ (g)\uparrow$$
$$[M\text{-}O]H + H_2O_2 \rightarrow [M\text{-}O]OH + H_2O$$
$$[\equiv M\text{-}O] + H_2O_2 \rightarrow [\equiv M\text{-}O]H + OOH^-$$
$$[\equiv M\text{-}O] + H_2O_2 \rightarrow [\equiv M\text{-}O]O + H_2O$$
$$[\equiv M\text{-}O]O + H_2O_2 \rightarrow [\equiv M\text{-}O]OH + OOH^-$$
$$2[\equiv M\text{-}O]O \rightarrow 2[\equiv M\text{-}O] + O_2(g)\uparrow$$
$$[\equiv M\text{-}O]OH + OOH^- \rightarrow [\equiv M\text{-}O] + H_2O + {}^{\cdot}O_2^-$$
$$H_2O_2 + {}^{\cdot}OOH \rightarrow {}^{\cdot}O_2^- + H_2O + OH^-$$
$$OOH^{\cdot} \leftrightarrow {}^{\cdot}O_2^- + H^+ \quad pk_a = 4.8$$
$$OH^- + {}^{\cdot}OOH \leftrightarrow {}^{\cdot}O_2^- + H_2O^{\cdot}$$
$$OOH^{\cdot} + {}^{\cdot}O_2^- \rightarrow HOO^- + O_2(g)\uparrow$$

Figure 2.1: Possible reaction mechanism of manganese oxide and hydrogen peroxide [17]

While adding a catalyst changes the pre-exponential factor and the activation energy of the reaction, it is evident from the Arrhenius equation (Equation 2.19, Section 2.2.2) that another parameter has an influence on the reaction rate: temperature. Hydrogen peroxide decomposition can indeed also be induced thermally, i.e., by the addition of heat. This process combines homogeneous decomposition in the liquid phase, vaporisation and homogeneous decomposition in the gaseous phase, but significantly less insight has been gained into purely thermal decomposition [11]. Often both approaches, catalytic

and thermal decomposition, are combined. [18] have conducted experiments with a hydrogen peroxide monopropellant thruster, using manganese oxide as a catalyst for the decomposition. They found that up to $150°C$, increasing the inlet temperature significantly reduces the pressure rising time, correlated to the decomposition rate, in the chamber.

Engine design for Use with Hydrogen Peroxide

To use hydrogen peroxide in a rocket engine, there are generally two types of engine design (Figure 2.2):

- The chamber is staged (**a**). In the first stage, HTP is led through a catalyst bed, i.e., a porous geometry with as high a surface to volume ratio as possible. This surface made from, e.g., silver, platinum or manganese [19], exothermically decomposes the HTP into gaseous water and oxygen. Decomposing, for example, 85%-H_2O_2 at standard conditions produces gas at temperatures of about $920°C$ [20]. The catalyst bed can be heated to improve the decomposition efficiency. The temperature of the resulting gas is well above the autoignition temperature of fuels like kerosene (around $568K$ or $295°C$). [21]. Thus, inserting the hot decomposition products from the first stage into the main combustion chamber together with liquid kerosene or other propellants leads to autoignition. This configuration can be used in bipropellant mode or in monopropellant mode, since the decomposed and hot hydrogen peroxide itself already provides thrust. Some designs can operate both as a mono- or bipropellant thruster.
- HTP is directly injected into the main combustion chamber in its liquid state and mixes with a fuel (**b**). Either the fuel is inherently hypergolic with hydrogen peroxide, or the hypergolicity is induced by a catalyst in form of small organic or metal particles which are added to the fuel, leading to ignition upon contact.

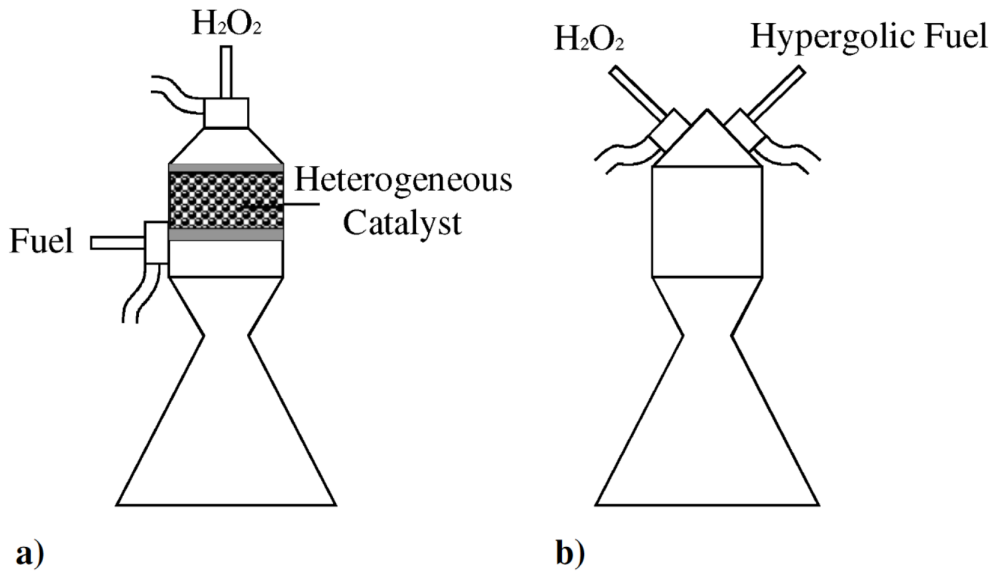

Figure 2.2: Thruster configurations using H_2O_2: a) decomposition by catalytic bed and b) decomposition by hypergolic fuel [22]

Type a) is used much more often, given the advantages that such engines can be operated in two modes (mono- and bipropellant) and that the staged configuration effectively decouples the HTP decomposition from the combustion, facilitating development.

Table 2.4 [23] shows hydrogen peroxide with a selection of fuels and the performance of the mixture. A catalyst is added to the alcohols to induce hypergolicity. MMH-NTO is added to the list as a benchmark, being the traditional propellant combination for use in satellites. The alcohol-HTP combinations do not quite reach the performance of the toxic propellants but achieve an I_{sp} of about 8% less. An advantage is the significantly lower chamber temperature. Specific impulse and chamber temperature appear to increase with increasing complexity of the hydrocarbon, i.e., longer carbon chains.

Table 2.4: Performance of different fuels with hydrogen peroxide and $20wt\%$ manganese based catalyst [23]

Oxidiser	**Fuel**	r_{opt}	$I_{sp,vac}[s]$	$\rho\ I_{sp,vac}[\frac{g\ s}{cm^3}]$	$T_C[K]$
NTO	MMH	2.1	313.6	372.2	3314
98%H2O2	Methanol	2.81	284.3	353.9	2682
98%H2O2	Ethanol	3.79	288.9	367.7	2761
98%H2O2	1-Propanol	4.29	291.2	374.9	2798
98%H2O2	2-Propanol	4.3	290.6	372.8	2790
98%H2O2	1-Butanol	4.6	292.4	378.6	2817
98%H2O2	2-Butanol	4.61	291.9	377.9	2811
98%H2O2	t-Butanol	4.62	291.4	375.8	2804

Hydrogen Peroxide & Kerosene

Most commonly, H_2O_2 is used in combination with kerosene or RP-1 (Rocket Propellant 1, a highly refined kerosene). Kerosene is not a single chemical species but consists of several species. Table 2.5 [24] gives an incomplete overview of the major components of RP-1.

Table 2.5: Components of RP-1 identified with chromatography-mass spectrometry-infrared spectrophotometry [24]

RP-1 Components		
2,6-dimethylnonane	2,6-dimethyldecane	2,6-dimethylundecane
x,y-dipropylcyclopentane	2-syn-methyldecalin	4-methyldodecane
1-ethyl-2-propylcyclohexane	1,3-dimethylbutylcyclohexane	2-methyldodecane
trans-decahydronaphthalene	5-methylundecane	7-methyltridecane
2-methyldecane	2-methylundecane	tridecane
3-methyldecane	5-ethyldecane	1-methylnaphthalene
n-undecane	1-methyl-l,2-pentylcyclohexane	6-methyltridecane
2-methyl-trans-decalin	n-dodecane	2-methyltridecane

Since kerosene is not a single chemical species but a mixture of several hydrocarbons, there is no single formula to describe it. It is however often described with a formula representative of the average hydrocarbon with a ratio of hydrogen to carbon atoms of approximately 2:1. Ansys Fluent by default uses the formula $C_{12}H_{23}$.

The propellants have a performance and storability similar to that of hydrazine while being significantly less toxic and thus have been researched a lot as a propellant for modern rocket engines. Like with other hydrocarbons, the mixture is not inherently hypergolic, so either a catalytist bed, a catalytic additive or a dedicated ignition system is required.

The combined reaction of hydrogen peroxide decomposition and subsequent combustion with kerosene can be summarised by Equation 2.7.

$$C_{12}H_{23} + 35.5\ H_2O_2 \rightarrow 12\ CO_2 + 47\ H_2O \tag{2.7}$$

To determine the oxidiser to fuel mass ratio (O/F), the molar masses of kerosene and hydrogen peroxide ($M_{C_{12}H_{23}} \approx 167g/mol$, $M_{H_2O_2} \approx 34g/mol$) and the concentration of hydrogen peroxide α, which for high-test-peroxide is usually between 85% and 98%, need to be taken into account to arrive at the stoichiometric O/F ratio, i.e., the ratio of HTP to kerosene mass flow rate (Equation 2.8).

$$O/F_{stoichiometric} = \frac{\dot{m}_{HTP}}{\dot{m}_{Kerosene}} \approx \frac{7.23}{\alpha} \tag{2.8}$$

2.2. Modelling Liquid Rocket Engines

To analyse the performance of a rocket engine in detail, several subdisciplines need to be considered: **Fluid dynamics** (Section 2.2.1) describe the propellant flow, which, given the high velocities, is usually highly turbulent. Often, not only gases are involved but also liquids or solids, for example in the form of cryogenic oxygen entering the combustion chamber before evaporating and combusting, or soot leaving the chamber as a combustion product, making this a multiphase problem. Thermodynamics describe the significant changes in temperature and pressure caused by the **combustion** (Section 2.2.2) process, which itself depends on the chemical composition and can consist of tens to hundreds of species and hundreds to thousands of intermediate reactions [25, 26]. Variations in any of the flow properties can locally temporarily amplify the combustion, leading to pressure and temperature peaks and thus varying performance, but more importantly, increased **structural and thermal loads** on the engine, potentially damaging or destroying the engine. Simulating these interactions demands excessive computational performance, making simplifications and model reductions necessary [25].

2.2.1. Fluid Dynamics

The Navier-Stokes equations describe the motion, specifically the conservation of momentum, of fluids. In their general form however, which is applicable for most problems involving compressible and viscous flows, they cannot be solved analytically, which is why detailed flow analyses must usually be approached numerically. The in reality continuous flow domain is discretised into small volumes, or Finite Volumes, for which a linear function is assumed to describe the variation of the flow properties within each volume. Based on an initial guess, the solution is iteratively improved until convergence is reached, i.e., until the errors are below an acceptable level and the difference from one iteration to the next is acceptably low. The solutions for all volumes (or cells) are approximated simultaneously. The discretisation of the continuous flow field leads to a discretisation (or numerical) error. The more the mesh, i.e., the discretised cells, approaches the continuum, the lower is the discretisation error. Usually a grid independence study is conducted where the mesh is refined until the difference in results between the meshes is negligible [27]. Depending on whether the analysis is two- or three-dimensional, two or three equations must be solved for the conservation of momentum - one per spatial dimension. Equation 2.9 describes the conservation of momentum in vectorial form for compressible viscous flow.

$$\frac{\partial (\rho \mathbf{v})}{\partial t} + \mathbf{v} \cdot \nabla (\rho \mathbf{v}) = -\nabla p + \mu \nabla^2 \mathbf{v} + \mathbf{B} \tag{2.9}$$

Likewise, the conservation of mass, i.e., the continuity equation, and, depending on the models chosen, further equations have to be solved for each cell, for example, conservation of energy, conservation of turbulent kinetic energy, conservation of species etc.

Turbulence

Turbulent flow is characterised by chaotic behaviour, causing fluctuations in pressure and velocity and dissipation of kinetic energy. In combustion, turbulence is crucial as it causes non-premixed propellant streams to mix, enabling the combustion process. A common measure of whether flow is laminar is the Reynolds number, which defines the ratio of inertial to viscous forces (Equation 2.10). It can also be seen as the ratio of a destabilising influence on the flow, the momentum, to a stabilising or damping influence, the viscosity [28]. If the flow exceeds a critical value, the laminar flow destabilises and transitions to turbulent. To give an order of magnitude: for internal pipe flows, the critical Reynolds number is between $2,000$ and $2,300$, for boundary layers it is around $200,000$ [28, 29].

$$Re = \frac{\rho v l}{\mu} \tag{2.10}$$

For internal flows, the characteristic length l is usually replaced by the diameter of, for example, the flow inlet or the choke point. For boundary layers, it can be replaced by the boundary layer thickness.

There are several modelling approaches for turbulent flow. The most accurate is Direct Numerical Simulation (DNS), which simulates all eddies in the flow. Depending on the smallest scale eddy, defining the Kolmogorov scale, this requires very high mesh resolution and thus is very computationally expensive. Hence, it is mostly used for scientific applications. In engineering, this level of detail is usually not required [30]. Since for many applications only the average turbulent flow is of interest, Reynolds Averaged Navier Stokes equations (RANS) are commonly used in engineering. The time varying velocity in any given direction v_i is broken down into an average value and a fluctuating value (Equation 2.11). Only the average value is of direct interest for the solution. To take into account the velocity fluctuation, a tensorial apparent stress, the Reynolds Stress, is introduced (Equation 2.12) [30, 31].

$$v_i = \overline{v_i} + \tilde{v_i} \tag{2.11}$$

$$\tau_{ij} = -\rho\overline{\tilde{v_i}\tilde{v_j}} \tag{2.12}$$

There are several RANS models to take into account turbulence, introducing one, two or more, up to eleven transport equations. Since more equations mean longer computation times, one- and two-equation RANS models are most widely used in literature [30, 32]:

The most relevant single-equation models are Spalart & Allmaras and Baldwin-Barth. Both models add a single transport equation to describe turbulence, namely for the turbulent viscosity (S&A) and for the turbulent Reynolds number derived from the k-ϵ model (B-B).

The two-equation models can be categorised into k-ϵ and k-ω models, with the turbulent kinetic energy k, the dissipation rate of turbulent kinetic energy ϵ and the specific dissipation rate of turbulent kinetic energy ω. Their relation can be described with Equation 2.13, allowing to derive one model from the other. The coefficient C_μ usually takes the value 0.09 [32].

$$\epsilon = C_\mu k\omega \tag{2.13}$$

The standard k-ϵ (*SKE*) model has been derived for fully turbulent flow and thus shows better agreement with test data or DNS in the freestream regions. The Renormalisation Group k-ϵ and the Realisable k-ϵ models have been developed to make the model applicable to a wider range of problems.

The SKE model includes considerations for low Reynolds numbers, resulting in a better solution near the wall. As the results in the freestream differ significantly from reality, the Baseline and subsequently Shear Stress Transport (*SST*) models have been developed, combining k-ϵ and k-ω into a single model using a blending function. Analysing numerous papers has shown that k-ϵ is most widely used in the analysis of rocket engines, for example see [33, 34, 35]. As this model is more accurate in the freestream, it delivers better results and better agreement with test data for performance metrics depending on the bulk of the velocity and pressure fields, especially for larger engines. If near-wall properties are of interest or have a larger impact, like in smaller engines, k-ω is usually preferred.

Large Eddy Simulations (LES) can be placed in between DNS and RANS, resolving the large eddies as in a DNS and modelling smaller eddies as in a RANS simulation. Hybrids between RANS and LES exist, for example Detached Eddy Simulations (DES).

An overview of all turbulence models available in Ansys Fluent is given in Figure 2.3.

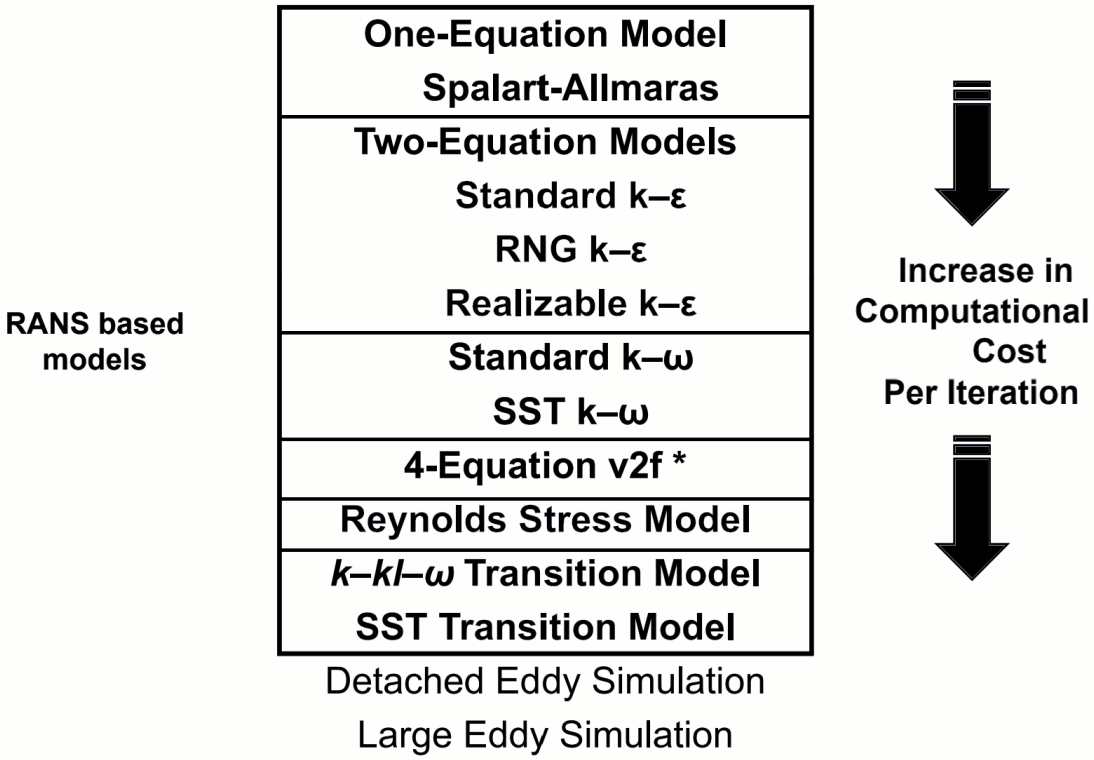

Figure 2.3: Turbulence Models Available in Ansys Fluent [31]

Wall Treatment

Figure 2.4 [32] shows the normalised velocity profile versus the distance from the wall. While far from the wall, the velocity follows a logarithmic curve, in the viscous sublayer near the wall the flow is virtually laminar and the velocity profile is linear. y^+ (Equation 2.14) denotes the normalised distance from the wall.

$$y^+ = \frac{\rho\, y\, u_\tau}{\mu} \tag{2.14}$$

$$u_\tau = \sqrt{\frac{\tau_{wall}}{\rho}} \tag{2.15}$$

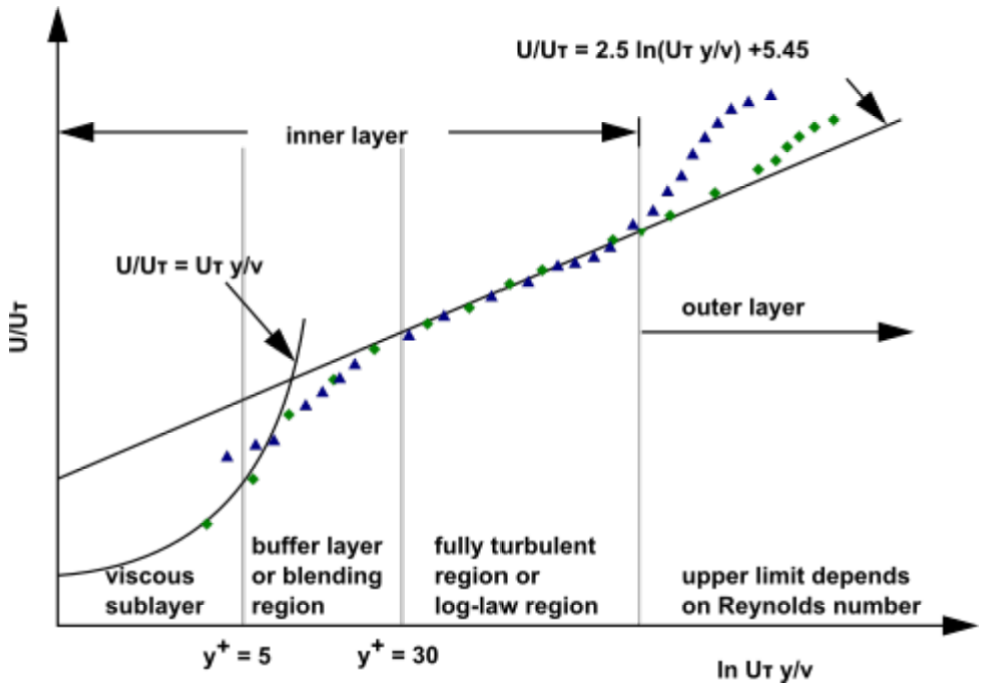

Figure 2.4: Subdivisions of the near-wall region [32]

If the first cell centroid is located within the viscous sublayer ($y^+ < 5$), the linear profile can be fully resolved. If the first cell is in the logarithmic region ($y^+ > 30$), the sublayer needs to be modelled with a wall function. Thus, the mesh resolution near the wall is critical in order to obtain an accurate result for properties near the wall. Depending on the desired outcome of the simulation, a high wall resolution may not be necessary. For determination of wall loads and especially heat transfer to the wall however, a $y^+ \approx 1$ is preferred [32].

The selected turbulence model also influences the near-wall mesh resolution. SKE cannot resolve the sublayer, hence requires a rather high y^+ value. k-ω models are designed to resolve the sublayer and thus should be used with low y^+ values. Since it is difficult to setup a mesh with a constant y^+ for complex geometries and high near-wall resolution can lead to unphysically high values for heat transfer or shear stress in the simulation, enhanced wall-treatment options have been developed to make the models more robust to a varying y^+. k-ω is inherently more robust.

Multiphase Flow

In rocket engine combustion, oftentimes multiple phases and phase transitions are involved. For example, the propellants might be liquid when inserted into the chamber and evaporate into a gaseous phase due to the heat of combustion. In the case of combustion of hydrocarbons, soot, i.e. solid carbon particles, might be present, which can lead to increased radiation [10] and clogging of the throat. At phase interfaces, for example the boundary of a comparatively cold liquid droplet surrounded by hot gas, there can be high gradients in properties like temperature, velocity, species concentration etc. Hence, depending on what shall be investigated with the simulation, modelling the different phases may be required for an accurate simulation.

For some applications, this is less relevant. If pressure and temperature are high enough, as often the case in high thrust applications, most propellants quickly become supercritical after injection. Hence

the differentiation between liquid and gas phase becomes impossible and even injected liquids can be modelled as a highly dense gas; for injected gases in high pressure propulsion systems, the pressure is always supercritical before injection, whereas temperature depends case by case [25]. This way of modelling is used for a variety of engines and propellant combinations, including liquid and gaseous hydrogen and oxygen as well as kerosene, delivering good agreement with experimental data [34, 36, 37, 38].

Hence it is also important to choose an applicable gas model. As the name suggest, the ideal gas law (Equation 2.16) is commonly used to describe the behaviour of gases, but it fails to accurately describe the behaviour of fluids that approach either the liquid or the supercritical state. To model those, the selected gas model must be a real gas model. The density calculated with the ideal gas law compared to a real gas law can deviate by a factor of 4 for non-ideal gases. Several real gas models exist, including the Redlich-Kwong, Soave-Redlich-Kwong, Peng-Robinson and Aungier-Redlich-Kwong models [39]. Most frequently, the Peng-Robinson equation of state is used to model the real gas behaviour (Equation 2.17) [25].

$$p = \frac{RT}{V_m} \tag{2.16}$$

$$p = \frac{RT}{V_m - b} - \frac{a}{V_m^2 + 2V_m b - b^2} \tag{2.17}$$

with the universal gas constant $R = 8.314 \frac{J}{mol\ K}$ and the molar volume V_m. a and b are material specific parameters.

Fluids become supercritical if they transition their critical point, i.e., both their temperature and pressure become higher than the critical temperature and pressure. For reference: For water, the critical temperature and pressure are approximately $T_c = 647K$ and $p_c = 22.1MPa$, respectively [40] and for kerosene, the critical temperature and pressure are approximately $T_c = 660K$ and $p_c = 2.4MPa$, respectively [41].

In smaller engines, chamber pressures are often below the critical point. Similarly, inlet pressures are usually lower, hence the propellants are subcritical and, if injected in liquid form, undergo a phase transition during combustion. This requires multiphase modelling. There are two ways of describing the movement of fluid: the Eulerian and the Lagrangian framework.The former observes a fixed volume and tracks properties of fluids entering and leaving that domain. The fluid is modelled as a continuum. The latter attaches to a discrete amount of fluid - this could be an individual molecule, a droplet or a volume containing an arbitrary amount of fluid, however with constant properties across the volume. This amount of fluid is tracked along its path, i.e., the observer moves with the fluid. The default method in simulation softwares like Ansys Fluent is Eulerian, since calculating flow parameters for an arbitrary number of fluid particles is computationally inefficient and thus rarely used for the whole domain of interest. Defining not one but several Eulerian phases in the simulation allows to model their interaction, including chemical reactions and mass transfer between phases or interface forces like surface tension. Several sub-models of Eulerian multiphase flow are available in Ansys Fluent, including the Volume of Fluid and the Fluid Mixture model [39] for immiscible and for miscible fluids, respectively. If one phase is small in volume or mass compared to the other(s), it can make sense to model it discretely, i.e., Lagrangian. This is especially interesting when looking at the propellant injection. For example, if a liquid propellant is injected into a combustion chamber filled with hot combustion gas, tracking the liquid droplets can make sense in order to accurately model the jet break-up and secondary breakup while modelling the majority of the fluid, the gas, in Eulerian form to maintain computational efficiency.

However, even for meshes with small cell count and 2D geometry, computation times can amount to several weeks on a high performance computer [42].

2.2.2. Combustion

Combustion is both a physical and a chemical process, consisting of mixing of a fuel and an oxidiser and subsequently one or several reactions, in which heat is released. In liquid rocket engines, fuel and oxidiser are usually injected separately into the combustion chamber. To make sure the combustion happens as quickly and efficiently as possible, the injectors are designed in a way that allows for thorough mixing of the propellants, for which turbulence is critical. Figure 2.5 depicts typical zones of combustion in a chamber with a converging-diverging nozzle. While the exact distribution depends on chamber geometry, injector design, propellants specification and operating conditions, generally any liquid rocket engine will have these zones. The processes in the chamber can be categorised into injection, atomisation, vaporisation, mixing & reaction, and expansion [10].

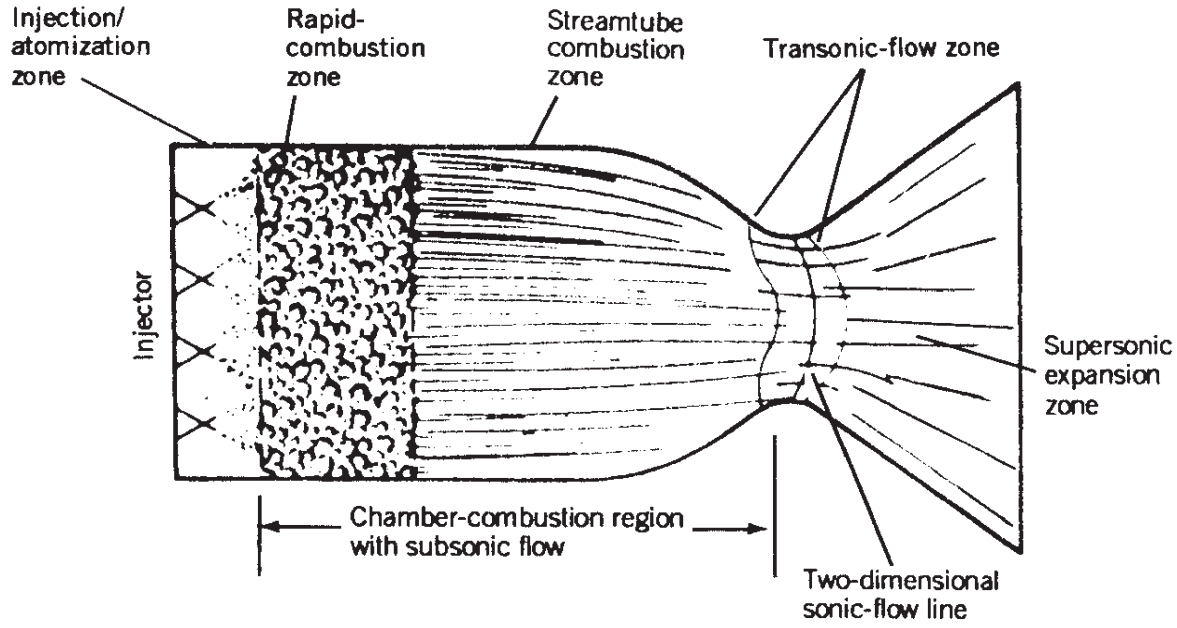

Figure 2.5: Division of combustion chamber into zones for analysis [10]

Combustion Modelling

Turbulent combustion is difficult to model since species concentrations, temperatures and reaction rates fluctuate with time with highly nonlinear dependencies, making the estimation of average reaction rates quite difficult. Average reaction rates have another issue: If a reaction requires a high activation energy or temperature to occur, it might only be initiated during temperatures peaks. But if the peaks, i.e., fluctuations are not modelled but only the cell average value is considered, reactions might occur significantly less or not at all. The averaged values simply cannot be extrapolated to accurately represent the highly non-linear dependencies between the flow properties. A different way of modelling is to use a Probability Density Function (PDF), which determines probabilities for flow properties like reaction rate, temperature etc. as a function of a dedicated variable prior to the actual simulation. During the simulation, the conservation equation for that variable is solved at all locations (and times) and further properties are derived using the values from the PDF. The PDF can either be calculated from

species transport equations, which consequently is more computationally expensive the more species are involved, or the PDF can be determined based on empirical data, for example from experiments [30].

There are two time scales relevant for combustion: the mixing of the propellants and distribution of heat, driven by turbulence, as all required reactants as well as sufficient energy need to be present for any reaction to happen; and the reaction rate, driven mostly by the activation energy, determining how quickly (and in which direction) the reaction occurs. Choosing the reaction model consequently also depends on which of the two time scales is expected to be the dominant one, i.e., the longer one [30].

The following reaction models are available in Ansys Fluent [39]:

- Species Transport
  - Finite-Rate Chemistry (reaction rate defines the time scale)
  - Turbulence-Chemistry Interaction through Eddy dissipation (turbulent mixing defines the time scale)
  - Combination of both
- Mixture fraction approach (Non-Premixed Combustion)
- Reaction progress variable approach (Premixed Combustion)
- Partially-Premixed Combustion
- Composition PDF Transport approach

In the Species Transport model, a conservation equation for each chemical species is included and each reaction is explicitly described by a stoichiometric reaction equation and Arrhenius rate parameters. Thus, depending on the number of compounds involved and depending on the accuracy of the reaction model, this can become very expensive. For example, the combustion of kerosene ($C_{12}H_{23}$) can be modelled with a one step reaction (Equation 2.18) only involving kerosene and oxygen as reactants and water and carbon dioxide as products, which would result in only four additional conservation equations.

$$C_{12}H_{23} + 17.75\ O_2 \rightarrow 12\ CO_2 + 11.5\ H_2O \tag{2.18}$$

Submodels of the Species Transport model define if the reaction rate is the time scale limiting the progress of combustion (Finite Rate Chemistry) or the turbulent exchange of species concentrations, temperature etc. (Turbulence Chemistry Interaction).

In reality, combustion processes consist of multiple intermediate reactions and can involve hundreds of species [25]. Calculating all conservation equations becomes very expensive and makes this model only useful if simple reaction mechanisms are considered.

To reduce the computational resources required to model such a complex combustion process, several simplified models are available where instead of one equation per species involved, there are fewer variables describing the progress of the process. The non-premixed combustion model is commonly used when modelling liquid rocket engines. It conserves the mass mixture fraction of the propellants and its variance, with a value of 1 describing the fuel, a value of 0 describing the oxidiser and a value of 0.5 describing an equal mixture (Figure 2.6). As the name suggests, this model works for systems which inject fuel and oxidiser separately. Before the simulation, a PDF is calculated describing the chemistry and the turbulence-chemistry interaction as a function of the two conservation variables. In

the premixed combustion model, both propellants are injected together and assumed to be perfectly mixed. The conserved variables are the progress of the combustion (0 meaning no combustion at all, 1 meaning complete combustion and intermediate values in the flame) or the position of the flame front, and in either case the variance of the variable [32]. Different from the Non-Premixed or Premixed models, the Composition PDF Transport model does not use a presumed PDF but calculates a PDF based on fluid density, velocity vector, composition and further flow properties. This joint probability density function is conserved, i.e., calculated throughout the simulation at all spatial and time steps. While still being a stochastic approach (opposed to the Species Transport model), it is much more accurate and expensive than the previous two models (Non-Premixed and Premixed). The PDF Transport is not compatible with spray breakup [32].

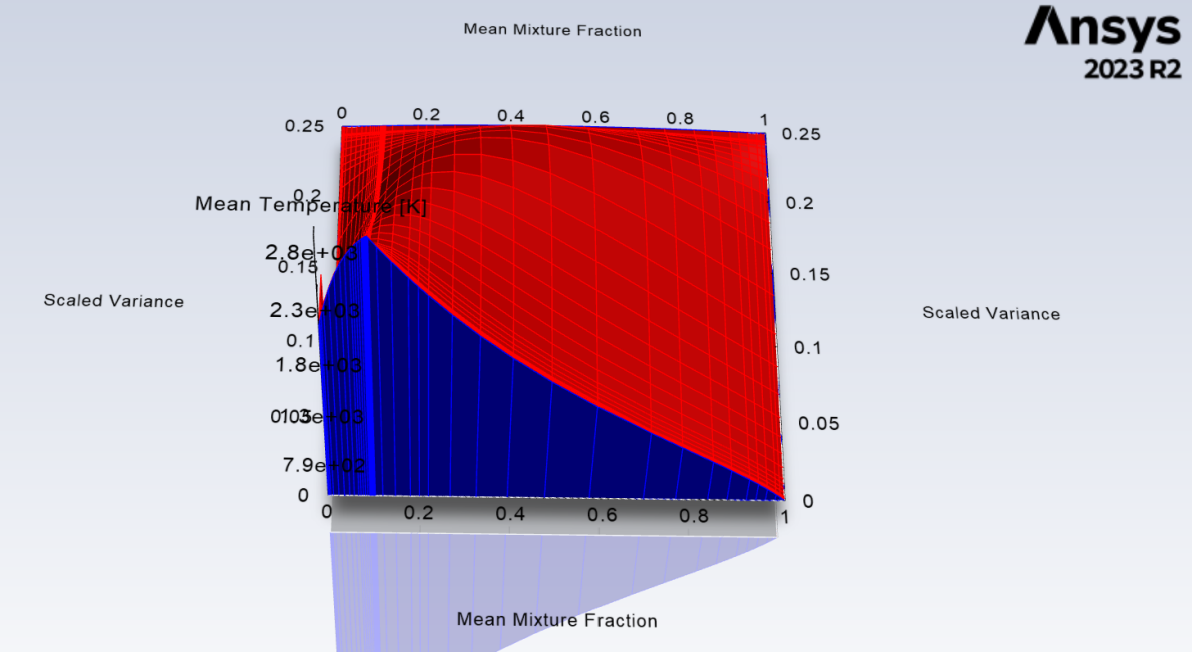

Figure 2.6: Example of temperature in a Non-Premixed-Combustion model, based on a PDF generated for hydrogen peroxide and kerosene at $t = 0s$. Temperature is only dependent on the mean mixture fraction and its variance.

In non-statistical models such as Species Transport, the creation and destruction of species through chemical reaction is determined by the forward and backward rates k of the given reaction, which are given by the Arrhenius-Equation (Equation 2.19), with pre-exponential factor or frequency factor A, temperature T, temperature exponent β, activation energy E_A and universal gas constant R [32]:

$$k = A\, T^{\beta}\, e^{-E_A/(RT)} \tag{2.19}$$

The temperature exponent is usually equal to 0. Additionally, pressure dependencies can be included.

The reaction rate k is also an indicator for the Ignition Delay Time (IDT), i.e., the time between contact of fuel and oxidiser and ignition. As is evident from Equation 2.19, raising the temperature speeds up the reaction and thus leads to a faster ignition. Increasing the pre-exponential factor or decreasing the activation energy has the same effect and can be achieved by the choice of the material, i.e., propellant composition and choice of catalyst. While adding a catalyst reduces the Ignition Delay Time (IDT), it can decrease performance [23].

The decrease in performance can also be explained with Equation 2.20 [7]. The exhaust velocity is proportional to $M^{-0.5}$, i.e., the higher the average molar mass of the exhaust gas, the lower the exhaust velocity, which is one of the downsides of using fuel additives such as aluminium particles . For example, the metal-based catalyst manganese dioxide with a molar mass of $M_{MnO_2} = 87g/mol$ has approximately twice the molar mass of carbon dioxide ($M_{CO_2} = 44g/mol$) or and five time the molar mass of water ($M_{H_2O} = 18g/mol$), the two primary combustion products. Hence, increasing the catalyst mass fraction leads to a decrease in exhaust velocity.

$$v_e = \sqrt{2\frac{\gamma}{\gamma - 1}\ \frac{R}{M}\ T_c \cdot \left(1 - \frac{p_e}{p_c}\right)^{\frac{\gamma}{\gamma - 1}}} \tag{2.20}$$

Combustion Instability

If the pressure in the combustion chamber during steady operation, i.e., not during start-up and shut-down, does not vary more than $\pm 5\%$ of the mean chamber pressure, it is considered stable or smooth [10]. In other words, combustion with higher fluctuations is considered unstable. These instabilities can in some cases reach values of ten times the steady-state chamber pressure at frequencies of over $15kHz$ [30], resulting in rapid destruction of the engine. Consequently, measures to ensure combustion as stable as possible must be taken. Combustion instability is not fully understood and topic of ongoing research. Generally, it is caused by interactions between fluctuations in the flow and the acoustic properties of the chamber [30]. Fluctuations include varying oxidiser-to-fuel-ratio, varying mass-flow, vibrations induced by the spacecraft etc. These lead to local differences in composition, temperature or pressure, thus different reaction rates and increased localised heat release, which provides the energy for further pressure fluctuation [30]. Instabilities can be roughly categorised by frequency [10, 30]:

- High Frequency: Coupled to the combustion process and acoustical chamber properties
- Medium Frequency: Caused by propulsion system vibrations, O/F fluctuations, resonances in the propellant feed
- Low Frequency: Caused by interactions with the propellant feed and/or the vehicle, especially feed pressure fluctuations.

Thus, to assess all types of instability, the engine cannot be assessed by itself but must be considered as part of a system. Since some level of varying feed and vibrations are always present, perfectly stable combustion is a purely theoretical case and a certain degree of instability has to be accepted. If the fluctuation that causes the instability and provides the initial energy for it is periodic, it is possible that the instability becomes periodic, i.e., the chamber pressure starts oscillating in phase with the causing fluctuation - this is in fact the most common form of instability. [30].

Instabilities can be further categorised by their mode, e.g., first, second, third mode etc., and by their direction, i.e., axial, radial or tangential [30]. While axial instabilities rather lead to varying performance, i.e., thrust, transverse instabilities appear to be the most destructive [30, 43].

Combustion instability is not fully understood and thus not fully repeatable, but there are different approaches to predicting it. To date, experimental measures appear to be the most reliable assessment method. [35] propose predicting instabilities by solving the Reynolds Stress transport equation by means of a CFD code, whereas according to [43], CFD is not really useful to assess instability and rather analytical methods based on energy dissipation should be used. [44] find that the Sauter-Mean-Diameter (SMD) and the Hewitt criterion can be good indicators for instability. All authors that investi-

gate stability agree that interactions between phases, including mixing, atomisation and vaporisation are central to understanding the phenomenon. For accurate results, a fully Eulerian approach seems insufficient - the injected phase is usually modelled in a Lagrangian framework.

Having relatively low-temperature premixed regions near the injector seems to contribute to instability [3, 30]. There are several ways to mitigate this:

- Increasing the droplet size, thus delaying the mixing
- Injecting a catalyst, lowering the activation energy and thus initiating reaction and higher temperature closer to the injector
- Injecting with higher pressure and/or higher O/F, reducing the IDT

Additionally, having a highly elastic wall seems to dampen instabilities throughout the chamber [30].

2.2.3. Wall Loads

Mechanical Loads

The mechanical loads acting on the combustion chamber wall are the pressure in wall-normal direction and the shear stress parallel to the wall. To determine the pressure at the wall accurately, a good wall resolution is necessary and combustion instabilities need to be analysed, as the momentary pressure increase in the form of instabilities can be orders of magnitude higher than the steady-state chamber pressure [30]. The shear stress directly depends on the velocity gradient at the wall (Equation 2.21).

$$\tau = \mu \frac{\partial v_x}{\partial r} \tag{2.21}$$

Thermal Loads

Heat transport in general happens through three mechanisms:

1. Convection
2. Radiation
3. Conduction

While all three mechanisms are present in rocket engines, convective heat transfer is usually the major component, with radiative heat transfer contributing between 5 to 40 % and conductive heat transfer, i.e., heat transfer through the wall in axial direction, being negligible [10, 30]. Near the throat, convection makes up up to 95% of the heat flux [30]. In low temperature ($T < 800K$) and low pressure engines, radiative heat transfer is often also negligible. In high temperature or pressure engines or if phase transitions happen within the engine, radiation becomes significant [10] and can contribute up to 90% of the heat in flame combustion [30].

There are several ways of modelling radiative heat [30]:

- In the *Heat Flow Method*, radiation is simplified to uniform radiation (perpendicular on each interface) and then discretised similar to FEM or FDM (so a hexahedron would have six radiative fluxes qx+, qx−, qy+ etc.). This is a strong simplification, leading to large errors.
- The *Zoning Method* works based on View Factors and Gebhardt Factors radiation exchange; it is only suitable for few surfaces/volumes with similar temperatures and absorption coefficients, as

otherwise it becomes too complex (if too many surfaces) or too inaccurate (if temperature and coefficients vary strongly)

- Other Methods exist, for example, the Monte Carlo ray-tracing, the Direct Transfer method, which is an improved version of the former, or the Discrete Ordinate method. The Monte Carlo method is quite accurate but very expensive, and the other two show inconsistencies compared to the real distribution.

Convective heat flux is strongly coupled to turbulence and combustion (in)stability in the chamber. Turbulent flow, leading to an exchange of energy, can easily double the heat flux near walls compared to a laminar flow [45]. Combustion instabilities, i.e., fluctuations in pressure, lead to even more significant increases in heat load (see Section 2.2.2). Consequently, this happens primarily close to the injection plane and walls close to the injection plane [45], where most of the instabilities originate.

2.2.4. Environmental Conditions

As discussed in Section 2.2.2, the performance and stability of the combustion process are highly sensitive to influences from the outside. The behaviour of the system the engine is attached to has an impact as well as the environment the overall system is exposed to. In a testing environment on ground, the atmospheric conditions can be predicted and even controlled well and are more or less constant. Tests can be postponed if necessary. As mass restrictions do not apply, a more more extensive set of measurement equipment to monitor mass flow rates, pressures etc. can be used. All this does not apply in space. The following two sections suggest which changes/boundary conditions to consider to replicate extreme conditions in-orbit.

Vehicle Induced Conditions

- Spacecraft vibrations could induce feed fluctuations, e.g., mass flow rate, pressure, O/F. In simulations, this could be modelled with a time-varying (e.g., sinusoidal) inlet boundary condition.
- Not only the steady-state operation is of interest. Especially during start-up and shut-down of the engine, inlet pressure and mass flow will have to gradually increase/decrease.

Atmospheric Conditions

- Depending on the location and orientation in space, the inlet propellant temperature may vary due to radiation to/from space incident on the tanks.
- Likewise, the engine (wall) temperature at startup depends on external radiation.
- Varying atmospheric pressure and density [46] would have an effect on the outlet boundary conditions, though changes in both seem small beyond 100km.
- The vacuum persisting in the chamber during idleness in space could result in breakup/outgassing from the engine wall, in turn effecting the combustion during operation.
- When operating in Low Earth Orbit (LEO), spacecraft are exposed to a low pressure atmosphere with a high concentration of atomic oxygen, which is highly reactive and can thus lead to engine deterioration [47].
- Especially hydrocarbons and metals are very sensitive to oxidation, whereas noble metals, silicones, oxides etc. are quite resistant and can provide good protection in the form of coatings [48].

- Such degenerative effects are negligible for short operation times, but changes over time, especially if the propulsion system is envisioned as an ACS for long missions in LEO, need to be predicted [47].

Table 2.6 shows the average ambient conditions in the atmosphere that rockets or spacecraft are exposed to. Table 2.7 and Table 2.8 show the change in properties during extremely low and high solar activity. It can be seen that, for example, the temperature in higher atmospheric regions rises by up to 600 K during strong solar activity. This needs to be seen in context of the simultaneously falling pressure, so the heat load is not comparable to a temperature rise of 600 K at sea level.

Table 2.6: Atmospheric conditions during mean solar activity varying with altitude [46]

Altitude $[km]$	**Temperature** $[K]$	**Density** $[kg/m^3]$	**Pressure** $[Pa]$	**Molar Mass** $[kg/kmol]$
0	300.2511	1.17E+00	1.01E+05	28.9502
100	184.016	5.08E-07	2.81E-02	27.7137
200	931.2806	2.91E-10	1.05E-04	21.4734
300	1,005.03	2.58E-11	1.20E-05	18.0015
400	1,010.97	3.89E-12	2.01E-06	16.3044
500	1,011.48	7.30E-13	4.07E-07	15.076
600	1,011.53	1.56E-13	1.01E-07	13.0389
700	1,011.54	3.91E-14	3.36E-08	9.7818
800	1,011.54	1.25E-14	1.58E-08	6.6572
900	1,011.54	5.46E-15	9.47E-09	4.846

Table 2.7: Deviation from mean atmospheric conditions during low solar activity [46]

Altitude $[km]$	**Temperature** $[K]$	**Density** $[kg/m^3]$	**Pressure** $[Pa]$	**Molar Mass** $[kg/kmol]$
0	0	0	0	0
100	-15.2941	6.9E-08	0.0008	0.2899
200	-246.3619	-1.16E-10	-0.000058	-0.2218
300	-306.1623	-1.858E-11	-9.53E-06	-1.0185
400	-311.8127	-3.322E-12	-1.787E-06	-1.4859
500	-312.3216	-6.697E-13	-3.738E-07	-4.5213
600	-312.3694	-1.457E-13	-9.01E-08	-7.524
700	-312.3743	-3.552E-14	-2.76E-08	-6.317
800	-312.3747	-1.059E-14	-1.184E-08	-3.8497
900	-312.3748	-4.28E-15	-6.66E-09	-2.399

Table 2.8: Deviation from mean atmospheric conditions during high solar activity [46]

Altitude $[km]$	**Temp.** $[K]$	**Density** $[kg/m^3]$	**Pressure** $[Pa]$	**Molar Mass** $[kg/kmol]$
0	0	-0.01	-1200	0
100	113.3178	-2.3E-07	-0.0018	-1.514
200	492.3663	5.37E-10	0.000381	-1.2898
300	594.0476	1.452E-10	0.000114	0.0824
400	608.2788	4.651E-11	3.819E-05	0.5774
500	610.2355	1.627E-11	1.379E-05	1.1207
600	610.5096	6.044E-12	5.209E-06	2.6932
700	610.5491	2.341E-12	2.076E-06	5.4905
800	610.5552	9.465E-13	8.682E-07	7.9875
900	610.5561	3.975E-13	3.875E-07	8.8555

2.3. Summary of Literature & Research Gap

2.3.1. Summary of Literature

For upper stage and on-orbit applications, there is a high demand for propulsion systems that combine high performance, storability and re-ignitability without being toxic. Hydrogen peroxide is a substance that is strongly researched in this regard as its decomposition, especially when catalysed, can provide moderate performance as a monopropellant or provide both oxidiser and activation energy for reaction with a fuel. Furthermore, it is non-toxic and storable. Two engine configurations are possible, either decomposing the H_2O_2 with a dedicated decomposition stage, or using a hypergolic fuel. Especially the combination of hydrogen peroxide and kerosene is widely used and much experimental work has been conducted on staged configurations.

Modelling combustion in a rocket engine needs to address the flow physics as well as the reaction chemistry. Turbulence, which is critical for mixing of the propellants, can be modelled in different ways, with the RANS models being most widely used since they provide good results without very high computational demands. As phase transitions happen within an engine, multiphase modelling is required, which can be divided into Eulerian (continuous) and Langrangian (discrete) frameworks. Both can be combined. Chemical reactions can be modelled by considering the species, their mixture and temperature in any cell at any time, or by calculating the probability of reactions and composition beforehand. Modelling flow properties like pressure, shear velocity, temperature and heat transfer, especially conduction, is crucial for the design of the thrust chamber to be able to select suitable materials and dimensions. The engine can furthermore be affected by changing atmospheric conditions, for example, the lack of a dense atmosphere in space preventing conductive cooling or radicals leading to chemical deterioration.

2.3.2. Research Gap

While several HTP-kerosene thrusters have been developed before, they usually used a staged configuration. To reduce mass and complexity, the setup investigated in the Greenlam project is not staged, i.e., there is no catalyst bed dedicated to the decomposition of the HTP before entering the combustion chamber. Instead, the oxidiser is inserted in its liquid, non-decomposed state. To still initiate combustion, a soluble catalyst is added to the fuel. Few papers were found that discuss this configuration, and their work was mostly experimental. While experimental work is important, it is less suitable for quick design iterations and parametric studies. Sensors cannot measure every property at each location in the engine. Hence, a combination of both experimental and numerical analysis is desirable. No literature describing the simulation of combustion of liquid hydrogen peroxide and liquid kerosene in an unstaged engine was found. Part of the reason may be that the exact reaction mechanism of coupled HTP decomposition and reaction is not understood yet, making its modelling difficult.

The models commonly used for existing thrusters are not inherently applicable to this case: Other hypergolic propellant combinations are often injected in a gaseous state, hence they do not undergo a phase transition and their modelling does not apply. Other liquid propellant combinations (kerolox) are usually used on larger thrusters with higher inlet pressures, which lead to supercritical inlet conditions, which is why their modelling is applicable neither.

Hence, this thesis shall explore how to model the combustion of liquid kerosene and liquid hydrogen peroxide in an unstaged small thrust rocket engine as applicable for the Greenlam engine, and consequently determine the engine's performance characteristics.

3

Research Plan & Methodology

Based on the research gap presented in the previous chapter, a research plan is developed in this chapter to attempt to contribute to filling that research gap and provide insights supporting the development of the Greenlam engine. Furthermore, the methodology adopted to implement that research plan and fulfil its requirements is presented.

3.1. Research Plan

3.1.1. Research Objective

As previously discussed, the Greenlam project is intended to develop an unstaged hypergolic thruster, using liquid hydrogen peroxide and kerosene, to provide a green propulsion solution for upper-stage or RCS applications. So far, work conducted on similar engines has been mostly experimental and existing numerical frameworks are not applicable to this engine. Hence, the objective of this thesis is to identify and validate models that can be used to simulate unstaged hypergolic biliquid hydrogen peroxide thrusters and, using these models, attempt to characterise the thruster's behaviour under defined operating conditions, i.e., during ground-testing, and subsequently during launch and/or in-orbit.

Since prototyping and ground-testing are necessary intermediate steps before flight, this thesis focuses on operating conditions as applicable to ground-testing.

3.1.2. Research Approach

To gain a good understanding of the engine under test and operational conditions, a numerical analysis incorporating physical and chemical phenomena in the engine is desirable. The following steps shall be followed to achieve that result:

- Identification of viable models for turbulence, multiphase flow and combustion
- Validation of models by comparison with simulations or experimental data from similar systems
- Running simulations and comparison of results to expected results and required performance parameters

- Variation of parameters like O/F, HTP concentration or minor geometric details to improve expected performance, e.g., thrust and specific impulse
- Assessment of combustion stability
- Change of boundary conditions to account for both ground test and realistic in-orbit conditions:
  - Standard gravity ($g_0 = 9.80665 m/s^2$) versus little or no gravity
  - Sea level atmospheric ambient pressure versus reduced ambient pressure
  - Stable versus fluctuating propellant feed properties

This research approach shall answer the following questions:

3.1.3. Research Questions

1. What are the characteristics of the flow and combustion in the engine?
   (a) How do temperature, pressure and velocity change throughout the chamber?
   (b) How do results differ for different propellant combinations?
   (c) Are there any combustion instabilities?
   (d) If so, where and to what extent? What causes these instabilities?
2. What loads on the wall can be expected?
   (a) What structural loads, i.e., pressure and shear forces, are present?
   (b) What thermal loads, i.e., convection and radiation, are present?
3. What combustion products can be expected?
   (a) How does the chemical composition change throughout the engine?
   (b) What is the composition of the exhaust?
   (c) Is nozzle erosion to be expected, e.g., by high oxygen concentrations?
   (d) Is nozzle clogging to be expected, e.g., by high soot concentrations?

3.1.4. Research Requirements

The following requirements were identified for the research to be considered successful: Combustion is the primary phenomenon under investigation and shall be modelled. Three spatial dimensions shall be considered to more accurately model the flow, considering that the injector design would likely not be truly axisymmetric. Furthermore, this would allow to analyse potential transverse flows to be able to look into transverse mode combustion instabilities. The simulation shall be transient to provide insight on the start-up behaviour and combustion instability. Since phase transitions from liquid to gaseous and potentially from gaseous to solid are to be expected, a multiphase model shall be used. Determining the effect of varying inlet parameters shall help to understand robustness against varying inlet parameters in reality and to find a set of parameters for optimal operation. Wall loads shall be determined to be able to define the exterior dimensions of the engine and to confirm the suitability of the selected materials and manufacturing process. The requirements are summarised in Table 3.1.

Table 3.1: Thesis Requirements

ID	Requirement
R1	**Simulations of the engine shall be performed, including:**
R1.1	Combustion of kerosene and HTP
R1.2	Three spatial dimensions
R1.3	Multiphase flow (continuous or discrete)
R1.4	Transient flow, ideally for the duration of one firing
R1.5	Different propellant combinations, i.e., HTP concentrations and O/F ratios
R2	**The model(s) used shall be validated with experimental or numerical data.**
R3	**From the flow simulations, expected loads on the chamber wall shall be determined.**
R3.1	Mechanical loads shall be determined.
R3.2	Thermal loads shall be determined.
R3.3	Combustion instability shall be taken into account for wall loads.

3.2. Methodology

3.2.1. Modelling Approach

As discussed in Section 2.2.1, there is no single best way to model a fluid flow. Depending on the case to be investigated and the results the analysis shall produce, different models have to be chosen. As discussed in Section 2.3.2, no papers could be found specifically on the simulation of bi-liquid hypergolic HTP-kerosene engines, there is no combined set of models validated for it. Most previous works focused on staged engines, which in terms of simulation have the advantage that the oxidiser entering the chamber is already decomposed, i.e., it is effectively hot gaseous water and oxygen instead of liquid hydrogen peroxide and there is no decomposition process that would need to be considered in the combustion chamber. Although hydrogen peroxide has been researched for years, the exact relationship between evaporation, decomposition and combustion is not fully understood, hence decoupling these processes simplifies the problem. The literature found on hypergolic hydrogen peroxide engines, i.e., without catalyst bed stage, is exclusively experimental.

To be able to simulate the flow in the Greenlam engine, adequate models for a number of physical and chemical phenomena need to be selected and their compatibility be tested. While no inlet pressure has been determined yet, it will likely be set in the range between 10 and 20 bar, typical for smaller engines and much below the critical points of the propellants. Hence, as discussed in subsection 2.2.1, multiphase modelling is necessary. While Lagrangian modelling is assumed to be more accurate, excessive computation times have been reported even for 2D cases, which cannot be realised for this thesis [42, 49]. For the investigation of instability, which is strongly coupled to droplet-gas interaction, especially jet breakup and evaporation, or to understand geometry altering phenomena like clogging (deposition of solid particles in injector or throat) and abrasion (removal of solid particles from the throat), setting up a discrete phase model is however considered a prerequisite. Since an engine design is considered where one of the major deviations from the typical HTP bipropellant engines is the omission of a catalyst bed, finding an accurate reaction model that includes the effect of a dissolved catalyst on the hydrogen peroxide decomposition is required.

Considerations relevant in any fluid simulation will be made, including turbulence and gas model as well as the definition of geometry and boundary conditions.

If the most appropriate model cannot be chosen simply by discussing the derivation and applicability of models, simulations with different setups will be run for comparison.

3.2.2. Model Validation

To validate the selected models, two approaches will be followed:

Results from papers describing similar engine setups will be attempted to be replicated and compared. These papers can be experimental or computational. Their geometry and boundary conditions will be replicated in the simulation software and be simulated with the previously determined set of models. Agreement between this simulation and the results from the corresponding paper would then be considered validation.

A different approach is to not directly replicate other works, but to compare the simulation results to both analytical calculations and to other rocket engines. While different engines would have different quantitative curves for pressure, temperature etc., normalisation thereof would allow for a qualitative comparison and thus provide validation.

3.2.3. Performance Assessment

To understand the engine behaviour, i.e., the physical and chemical processes in the chamber, the flow properties temperature, pressure and velocity will be analysed, since especially temperature directly impacts the occurrence of reactions, and temperature, pressure and velocity depend on the reactions. At the same time, these parameters are commonly investigated by other research and allow for comparison to other rocket engines.

The structural and thermal capabilities of the engine needed to be considered: a high engine performance is correlated to high flame temperature and chamber pressure, which adversely effects the demands to the properties of the newly developed material (UHTCMC) and increases structural mass. To that end, mechanical loads (wall shear stress, pressure) and thermal loads (wall temperature, heat transfer coefficient) will be analysed.

To optimise engine performance, the most important metric is considered to be the thrust output of the engine compared to the mass flow rate injected, or in other words, the specific impulse (see Equation 4.1). Since the thrust requirement of $F = 100N$ has been defined independently of the propellant choice, the specific impulse and the mass flow rate required to obtain that thrust are chosen as performance metrics.

To get an estimate for both the performance and the loads and how they vary, simulations shall be performed with different propellant combinations, i.e., HTP concentration and equivalence ratio.

3.3. Summary of Research Plan & Methodology

The primary objective of this thesis is to find a set of models suitable to simulate the Greenlam engine to characterise its behaviour, and thus also suggest a model framework generally applicable for simulations of similar engines, especially unstaged hypergolic bipropellant engines using hydrogen peroxide. To find these models, applicable models will be chosen through reasoning before simulation or by running different models and comparing results. Validation shall be performed by replication of other papers and by comparison to other engines as well as analytical estimates. Once the set of models is finalised, boundary conditions will be varied to investigate the effect of different inlet-conditions like concentration and O/F ratio. Figure 3.1 summarises this methodology.

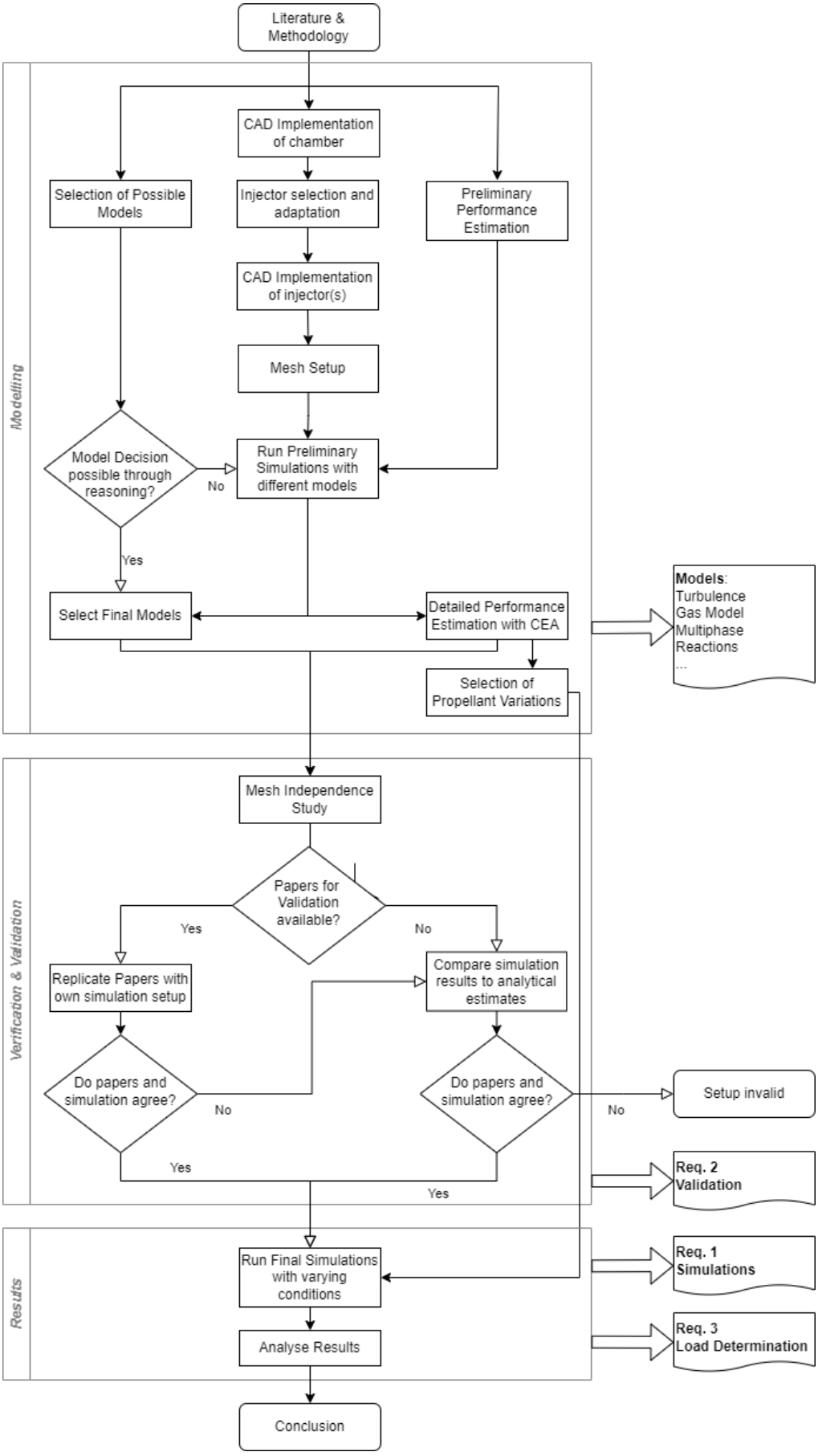

Figure 3.1: High-Level Methodology

4

Modelling & Validation

This chapter describes the selection of models for the simulations and the reasoning behind the model selection as well as preliminary simulations. Verification through a mesh independence study and validation by comparison to other papers and analytics is demonstrated. Setups and validation attempts that were tried but did not produce good results are also shown and analysed with respect to why they did not work.

4.1. Chamber & Injector

Figure 4.1 shows the geometry of the combustion chamber designed by SolvGE. Only the interior dimensions are fixed, the wall thickness will be determined by further studies within the group. Maximum interior dimensions are $126mm$ axially and $17.5mm$ radially.

4.1.1. Material

The material of the chamber walls, excluding the injector plate, is an Ultra High Temperature Ceramic Matrix Composite (UHTCMC) containing carbon fibres. The material is currently under development at the faculty. Preliminary material properties (Table 4.1) were provided by the research group and taken into account in the simulation to model the heat transfer to the walls.

Table 4.1: Preliminary UHTCMC material properties

Parameter	Value
Density	$3477kg/m^3$
Specific Heat	$661.87J/kgK$
Wall Thickness	$0.005m$
Thermal Conductivity	$30W/mK$
Max. Allowable Temperature	$2773K$

4.1.2. Injector

The injector design for the engine has not been finalised so far. However, as discussed in Section 2.2.2, the propellant injection, atomisation and mixing have a strong influence on combustion stability and

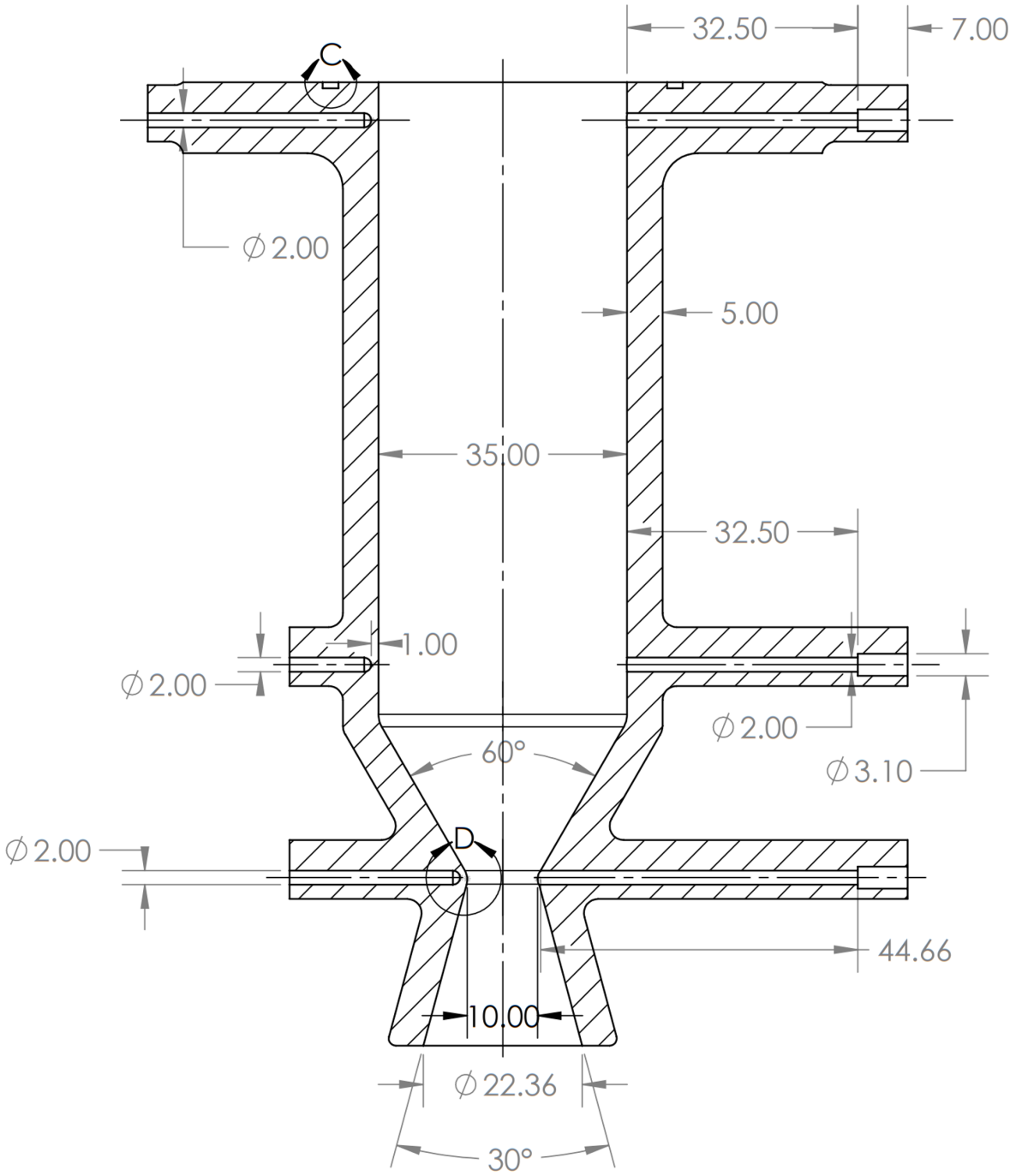

Figure 4.1: Technical drawing of the Greenlam combustion chamber provided by SolvGE

on the flow overall, which is why the injector design has a significant impact on the simulation. Since it was not within the scope of this thesis to design an injector, simplified versions of different kinds of existing injectors were adapted to the present engine and tested in the simulations to assess the impact of the injector on the flow. A coax injector was chosen due to its geometric simplicity, a pintle and an impinging-jet injector were chosen due to their stability enhancing properties, frequent use in small thrust engines and availability of test results with hydrogen peroxide. Depending on the results, one of these injectors or adapted version might be used for the thruster.

Coaxial Injector

To start with a geometrically simple design, a coaxial injector was chosen. As no injector for the specific propellant combination could be found, injectors for kerolox were investigated, given the similar densities of the propellants. DLR developed such an injector under the SMall Innovative Launcher for Europe (SMILE) project [50]. Their design was simplified and scaled down to be used as initial design for the Greenlam engine (Table 4.2, Figure 4.2).

Table 4.2: Coaxial Injector Geometry adapted from DLR SMILE [50]

Parameter	Value
Number of Orifices/Annuli	18
Annulus Diameter (Fuel)	$4.2\ mm$
Baffle Diameter	$2.875\ mm$
Orifice Diameter (Oxidiser)	$2.375\ mm$

The injector features 18 orifice-annulus pairs, with each orifice functioning as an oxidiser inlet and each annulus as a fuel inlet.

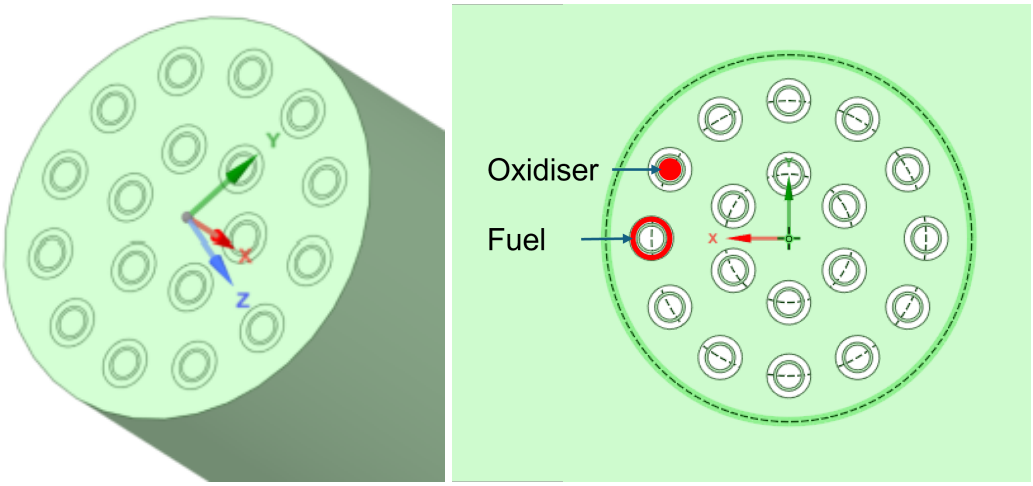

Figure 4.2: CAD Implementation of simplified and down-scaled Coaxial Injector according to specifications given by DLR [50]

Impinging Injector

A research group at KAIST [51, 52] made use of an impinging jet injector. They used HTP and a catalytic hydrocarbon blend as propellants. The axes of the individual injection tubes are not parallel but angled with respect to each other. This causes the propellant jets to intersect or impinge on each other, significantly enhancing atomisation, distribution and mixing [7]. In this case, the configuration is referred to as an unlike pentad injector. Four oxidiser injectors are placed around one central fuel injector and angled 30 $^\circ$ towards it. The geometry was not scaled but directly implemented in CAD (Table 4.3, Figure 4.3).

Table 4.3: Impingement Injector Geometry from KAIST [51]

Parameter	Value
Number of Orifices	1 (Fuel) + 4 (Oxidiser)
Fuel Inlet Diameter	$1.20\ mm$
Oxidiser Inlet Diameter	$1.25\ mm$
Impingement Angle	$30\ ^\circ$

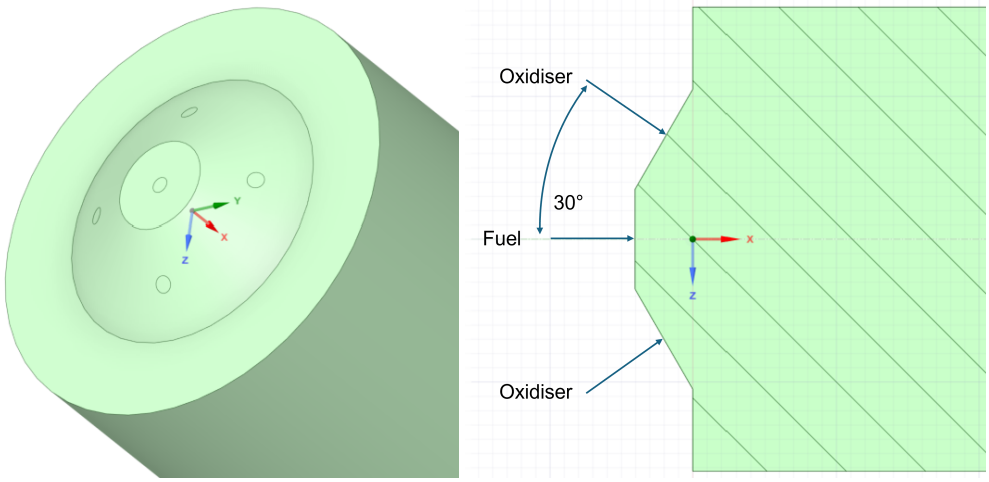

Figure 4.3: CAD Implementation of Impinging Injector according to specifications given by KAIST [51]

Pintle Injector

Researchers from Purdue University [53] used a pintle injector. Pintle injectors inherently provide combustion stability, are highly throttleable (up to a factor of 20), achieve good propellant mixing regardless of the propellants' relative injection velocities and high combustion efficiencies. Downsides are a comparatively long required chamber length [7, 54]. Like regular coaxial injectors, they consist of a coaxial inner tube and an annulus. Behind the outlet of the tube, there is a pintle, forcing the flow to divert radially and thus intersect the annular stream. Different from standard coaxial injectors, they only feature a single injector element. The pintle was implemented in CAD to be used for validation simulations (Table 4.4, Figure 4.4).

Table 4.4: Pintle Injector Geometry from Purdue University [53]

Parameter	**Value**
Pintle	
Pintle diameter	$9.525\ mm$
Pintle length	$11.43\ mm$
Primary hole diameter	$0.57912\ mm$
Secondary hole diameter	$0.381\ mm$
Number of hole pairs	16
Fuel exit area	$6.038698\ mm^2$
Fuel injection velocity	$14.35608\ m/s$
Parameter	**Value**
Annulus	
Injector face hole diameter	$10.5918\ mm$
Gap distance	$0.5588\ mm$
Oxidiser exit area	$17.29029\ mm^2$
Oxidiser injection velocity	$8.65632\ m/s$

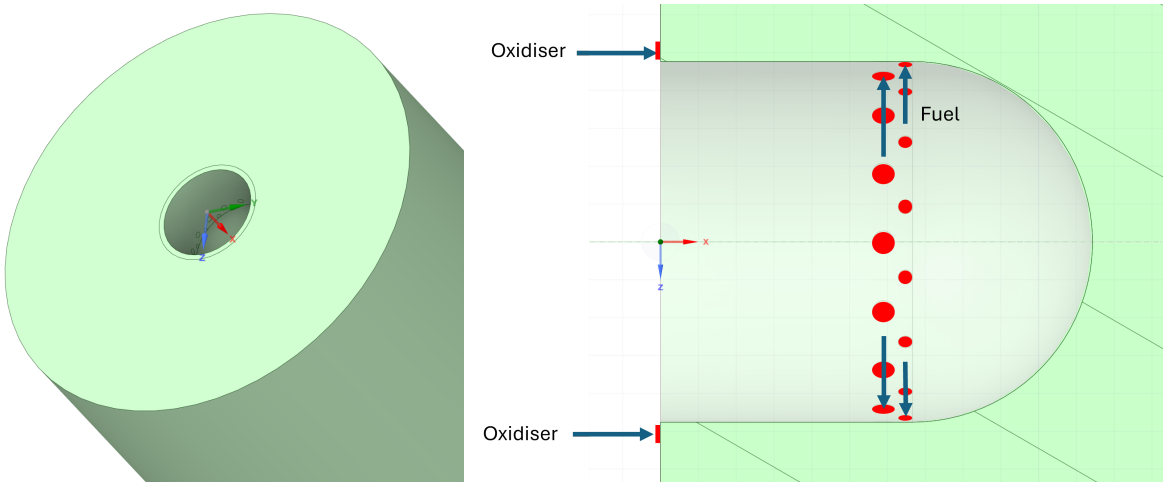

Figure 4.4: CAD Implementation of Pintle Injector according to specifications given by Purdue University [53]

4.2. Model Selection & Simulation Setup

Simulations were performed with Ansys Fluent 2023 R2 and run on DelftBlue, the TU Delft's super computer cluster operated by the Delft High Performance Computing Centre (HDPC) [55].

4.2.1. Preliminary Simulations

Several different simulation setups were tried to become familiar with the combustion behaviour and evaluate the models, while using the same propellant parameters to allow for comparison.

Using Equation 4.1 [7], the required mass flow rate could be derived from the thrust requirement and the specific impulse which depends on the propellant combination.

$$I_{sp} = \frac{F}{\dot{m}\ g_0} \tag{4.1}$$

With a thrust goal of $F = 100N$, HTP-concentration of $\alpha = 0.98$, a vacuum specific impulse of $I_{sp,vac} = 319s$ [56] and a stoichiometric oxidiser-fuel-ratio (O/F), this resulted in the following mass flow rates (for the calculation of the mass flow rates, see section A.1):

$$\dot{m}_{fuel} = 5.01\ g/s$$
$$\dot{m}_{oxidiser} = 32.34\ g/s$$

The above values were used for all preliminary simulations.

4.2.2. Turbulence

Since there was high interest in determining the loads on the chamber wall, required for subsequent dimensioning of the same, the k-ω SST model was chosen. It combines the accurate modelling capability of k-ω for flow near walls with the good free stream modelling of k-ϵ. Furthermore, while the aim was to resolve the viscous sublayer ($y^+ < 5$), this model is inherently robust to varying y^+ values.

4.2.3. Multiphase Model

As discussed in Section 2.2.1, multiphase models can roughly be categorised in Lagrangian and Eulerian approaches, with the former being especially useful for small numbers of droplets (or solid particles)

and modelling droplet-gas interaction, and the latter being computationally cheaper and more suited for bulk fluids. Using a Lagrangian framework was preferred to accurately model the droplet-gas interaction as well as the droplet-droplet interaction, i.e., collision, breakup, atomisation, evaporation and mixing. Regardless, both approaches were tried.

Eulerian Model

As kerosene and water/hydrogen-peroxide are not miscible, the Volume of Fluid Model was used rather than the Mixture Model. The gas was set as the primary phase, each propellant as a secondary phase. Using Lee's evaporation-condensation model, propellants can transition to the primary phase to allow for gas-phase reactions to happen. While the simulations were stable, they did not show ignition. Further investigation showed that even after several seconds, not all propellants were present in the gas phase. It was found that the issue was in the definition of the evaporation model. Lee's model takes as input the saturation temperature, i.e., the boiling point, of each species. If the temperature in the domain is higher than that temperature, vaporisation through boiling is initiated. Below that temperature, no vaporisation (through evaporation) happens. This goes against what was expected. For example, water at atmospheric pressure has a boiling point of $100\ °C$ or $373.15\ K$. Below that temperature, there would be no boiling, but there would still be evaporation of water into the surrounding medium until that medium, for example, air, is saturated with water. This process is governed by the saturation pressure of water, which is temperature dependent, meaning, at higher air temperatures the water saturation pressure is higher and more water can evaporate. To incorporate this into Lee's model, the saturation temperature which in Fluent by default is constant for many species, was redefined as a function of pressure. Different models exist to describe saturation pressure as a function of temperature. The Antoine equation is a rather simple function with reasonable agreement with test data and parameters could be found for both H_2O_2 and H_2O.

$$\log_{10}\left(\frac{p_{sat,H_2O_2}}{Pa}\right) = -\frac{2534.72\ K}{T} + 10.9779\ [57] \tag{4.2}$$

$$\log_{10}\left(\frac{p_{sat,H_2O}}{Pa}\right) = -\frac{1730.63\ K}{T - 39.724} + 10.1962 \tag{4.3}$$

A number of temperature-pressure tuples was calculated and inserted as points for a piecewise-linear function in Fluent to test the model with H_2O_2 and H_2O only. Again, no vaporisation was seen. Plotting the saturation temperature for water determined by Ansys using Lee's model showed a value of $373\ K$ throughout the whole domain, i.e., the saturation temperature for $1\ bar$, whereas at a vapour-phase water concentration of 0, the water partial pressure is also 0 and thus a much lower saturation temperature was expected. This led to the realisation that Lee's model indeed does not consider the species' partial pressure to calculate saturation, but the static pressure of the whole mixture.

This vaporisation model may be useful for applications where the ambient temperature is higher than the saturation temperature and the dominant vaporisation process is boiling rather than evaporation. In a non-hypergolic rocket engine, this is achieved with a dedicated ignition system that adds energy leading to a rise in temperature, which vaporises propellants and initiates ignition. Since the engines investigated in this report rely on a small amount of hydrogen peroxide to evaporate and decompose to initiate ignition, the Lee model is not suitable. No other vaporisation models are available in Fluent with the VOF setup.

The Eulerian multiphase flow model did not lead to ignition in any of the simulations, presumably due to the lack of propellant evaporation and was not further considered.

Lagrangian Model

Consequently, only the combined Eulerian-Lagrangian model was used in further simulations. Chamber and atmospheric gases were modelled as a continuum, the liquid propellants were injected as discrete particles which, by evaporation, transition into the continuous phase, where they could react.

Interaction between discrete and continuous phase was activated for the droplets to be influenced by the gas and to allow for evaporation. Unsteady and high-resolution particle tracking were enabled for improved numerical stability and accuracy, respectively.

Two different propellant injections were setup (one for the fuel, one for the oxidiser) using the surface injection to be able to use the previously defined inlet surfaces and have droplets injected over the whole surface. Mass was injected using the face-normal direction.

Multi-component droplets were chosen to be able to incorporate blends of species, e.g., the mixture of hydrogen-peroxide and water injected as one single solution. For each liquid species, the corresponding species in the gaseous mixture was selected for evaporation.

4.2.4. Reactions

As described in Chapter 2, the reaction mechanism of the combined decomposition and combustion is not fully understood. While several decomposition mechanisms have been proposed, no definitive mechanism could be found. In any case, the rate determining step would be the first reaction. Thus, it seemed sufficient to model only the overall decomposition reaction from H_2O_2 to the final products, oxygen and water, as well as the combustion of kerosene to the final products carbon dioxide and water. While the catalyst would be part of intermediate reactions (for example, see Figure 2.1), a catalyst by definition is not consumed in the reaction and hence would not be included in the net reaction equation [58].

Due to the limited number of species (six: five species participating in reactions plus nitrogen present in the atmosphere), calculating a conservation equation for each species seemed feasible. Hence, the Species Transport model was chosen, which additionally allowed to include the effect of the catalyst on the Arrhenius rate, and compared to PDF based methods does not rely on statistics. Finite-Rate chemistry was selected, assuming that combustion and especially ignition are primarily dependent on the catalyst and its effect on the Arrhenius rate. Since reaction rates in the liquid phase are by two orders of magnitude smaller, it was assumed that reactions only occured homogeneously in the gas phase. Consequently, for decomposition to happen, the hydrogen peroxide injected as liquid first had to undergo a phase transition. This model has also been used previously in literature [34].

Since the specific choice and concentration of the catalyst have not been finalised and modelling the catalyst as a separate species and potentially as a solid phase would add further complexity, the catalyst was not modelled. Instead, its effect on the reaction rate parameters was represented by changing the reaction rate parameters directly in the reaction between kerosene and hydrogen peroxide. As explained in Section 2.2.2, this likely led to an increased exhaust velocity.

Since hydrogen peroxide can still decompose thermally, i.e., without contact with the catalyst, and the released oxygen can subsequently combust with kerosene, the total reaction mechanism included three reactions (Equation 2.5, Equation 2.7, Equation 2.18).

One issue during preliminary simulations was that steady state was reached after about $5-7ms$. Drop tests conducted by the research group with this propellant combination have shown ignition delay times of about $50ms$. While some deviation could be expected, for example due to higher temperature or better atomisation, an order of magnitude seemed excessive. This deviation was most likely due to the exact Arrhenius parameters of the reactions being unknown (see Section 2.1.3).

Different Arrhenius rate parameters were tried. Since no data could be found for catalyst induced combustion of kerosene and HTP, values from other HTP reactions were used as an estimate (see Table 2.3). Activation energies for the thermal decomposition and the combined catalytic decomposition and combustion were taken from the only experiment found that used manganese oxide as a catalyst [12]. The pre-exponential factor is the lowest value found for gas-phase decomposition [15]. For the kerosene-oxygen reaction, parameters are already predefined in Fluent. The final values can be seen in Table 4.5.

Table 4.5: Reaction Mechanism & Parameters with thermal decomposition of hydrogen peroxide (a), catalyst induced combustion of hydrogen peroxide and kerosene (b), and combustion of oxygen and kerosene (c)

	Reaction			A [s^-1]	E_A [kJ/mol]
(a)	H_2O_2	$\rightarrow$	$H_2O + 0.5\ O_2$	$1e13$	75.0
(b)	$C_{12}H_{23} + 35.5\ H_2O_2$	$\rightarrow$	$12\ CO_2 + 47\ H_2O$	$1e13$	58.0
(c)	$C_{12}H_{23} + 17.75\ O_2$	$\rightarrow$	$12\ CO_2 + 11.5\ H_2O$	$2.587e9$	125.6

4.2.5. Gas Model

As discussed in section 2.2.1, real gas models become relevant as soon as very low or very high temperatures and pressures are reached, i.e., the gas approaches its liquid or supercritical phase. Looking at the critical point for kerosene (section 2.2.1), the critical point could be exceeded in the engine, which is why a real gas model had to be considered. Figure 4.5 shows the same reference simulation run once with the ideal gas model and once with the Peng-Robinson real gas model. Peng-Robinson was chosen over other real gas models as it was found to be most widely used in the studied literature. Results especially for temperature, velocity and density showed significant differences between ideal and real gas, highlighting a more prominent over-expansion of the flow. Hence, using the ideal gas model did not seem appropriate for this study and the Peng-Robinson model was used for further simulations.

4.2.6. Propellant Variation

An observation was made regarding the temperature contours: The combustion temperature in the centre was in the expected range around $2950K$. Towards the wall, there was hardly any decrease in temperature. While the material is still in development and its thermal properties have not yet been tested, its expected allowable temperature is around $2500°C$ or $2773K$. So to have a sufficient margin of safety, the temperature needed to be lowered.

To decrease wall temperature, two adaptations could be made: Increasing the O/F ratio would lead to an oxygen rich combustion, ensuring complete combustion of the kerosene. In this specific case, the oxidiser itself produces thrust by decomposing even if it does not participate in a combustion reaction. Since the decomposition of H_2O_2 leads to products with a temperature of about $1225K$ for a concentration of 98%, this would significantly lower the average temperature. Decreasing the H_2O_2 concentration would lead to more water in the chamber, taking up energy to evaporate, thus lowering the overall temperature.

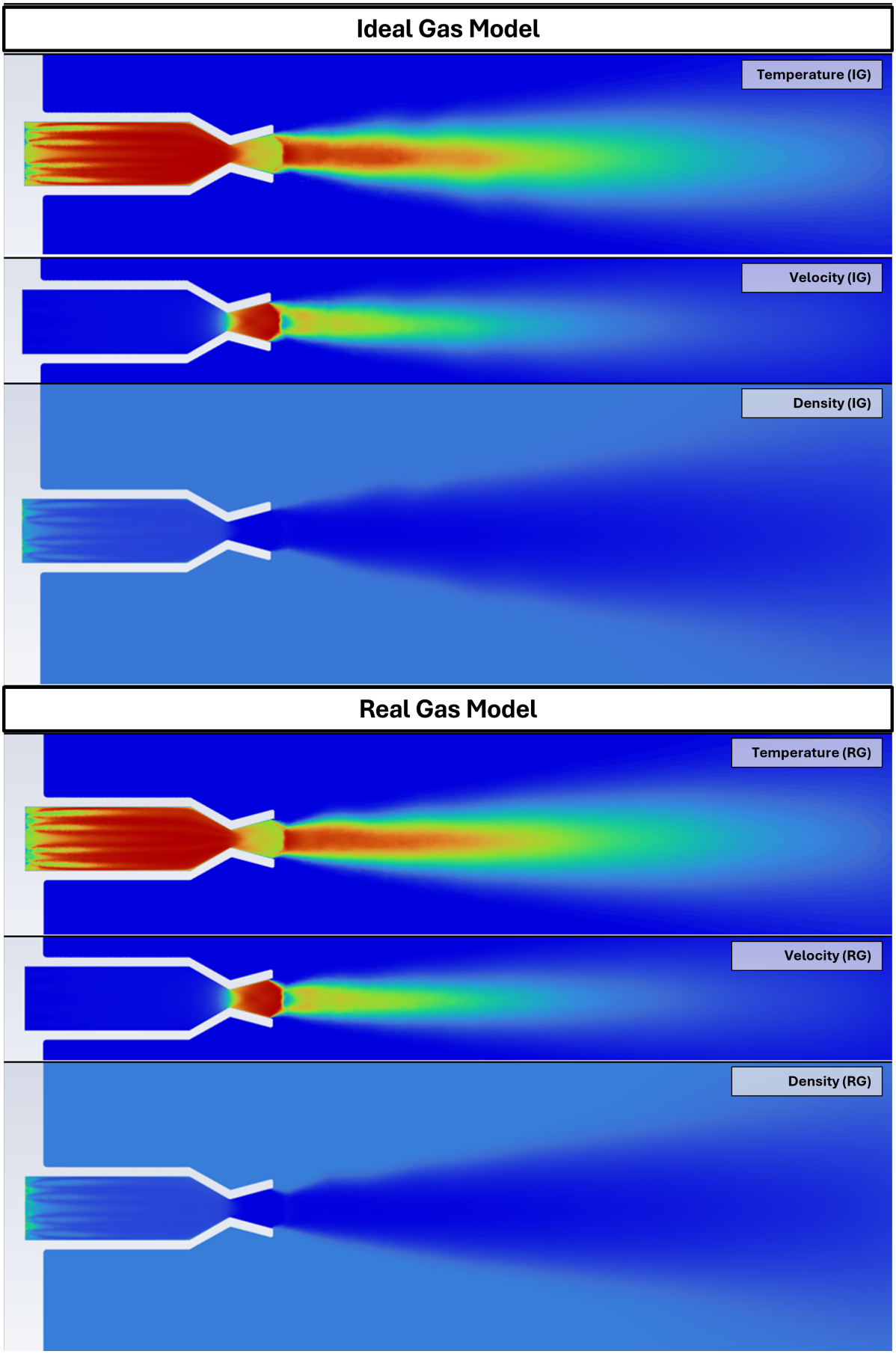

Figure 4.5: Comparison of Ideal Gas and Real Gas (Peng-Robinson) models

Based on these considerations and observations of the preliminary simulations (Section 4.2.1), a study was performed using the publicly available NASA code Chemical Equilibrium with Applications (CEA) [59]. Chamber pressure p_c was varied from $5bar$ to $10bar$ with an interval of $0.5bar$. HTP concentrations α of 90%, 95% and 98% were considered. Equivalence ratio Φ was varied from 0.90 to 1.10 with an interval of 0.05. The equivalence ratio describes how the propellant mixture deviates from the stoichiometric mixture ratio, e.g., $\Phi = 1.0$ indicates stoichiometric combustion and $\Phi = 0.5$ indicates highly oxidiser-rich combustion with only half the oxidiser present that would be required to oxidise all fuel.

For reference, Table 4.6 shows the values for $p_c = 7.5bar$, as this is the closest to the previously obtained value of approximately $7.4bar$. The chamber temperature range across chamber pressures for any given combination of Φ and α is less than 2%.

Table 4.6: CEA output for $p_c = 7.5\ bar$

	Φ	O/F	$T_c\ [K]$	$I_{sp,vac}\ [s]$	$I_{sp,sl}\ [s]$	$\dot{m}\ [10^-3\ kg]$
98%	0.90	8.21	2749	273.1	243.4	37.32
	0.95	7.78	2770	275.5	245.1	37.00
	1.00	7.39	2787	277.4	246.5	36.75
	1.05	7.04	2798	278.6	247.8	36.58
	1.10	6.72	2804	279.2	249.0	36.50
95%	0.90	8.47	2699	270.2	241.2	37.72
	0.95	8.02	2723	272.7	243.0	37.38
	1.00	7.62	2740	274.7	244.4	37.11
	1.05	7.26	2752	275.9	245.8	36.95
	1.10	6.93	2758	276.3	246.9	36.89
90%	0.90	8.94	2609	264.8	237.1	38.50
	0.95	8.47	2636	267.6	239.1	38.10
	1.00	8.04	2656	269.8	240.6	37.79
	1.05	7.66	2669	270.7	242.1	37.66
	1.10	7.31	2674	270.8	242.7	37.65

Total mass flow $\dot{m}$ is not output by CEA but was calculated from the vacuum specific impulse and the vacuum thrust requirement $F_{vac} = 100N$ according to Equation 4.1, all other results were obtained from CEA. For the CEA in- and output files, see section A.2.

The values found serve as an estimate but cannot provide ultimate accuracy. The code assumes chemical equilibrium whereas the simulation used finite rate chemistry leading to slower reactions. Furthermore, not all propellant properties in CEA are defined for the inlet temperature of around $300K$, so lower values had to be inserted for the analysis to run. Hence, inlet enthalpy in reality would be higher. Regarding the chamber temperature, even the highest temperature in Table 4.6 was only $31K$ above the limit temperature. Assuming that the temperature would decrease towards the wall due to less reactions happening and heat transfer to the outside cooling the wall, the temperature should be sufficiently low.

The data showed that both temperature and specific impulse increase with increasing chamber pressure, increasing concentration and increasing equivalence ratio, i.e., decreasing O/F. Opposing the previous assumption, the highest performance is not achieved with an equivalence ratio of 1 (see Figure 4.6). The reason for that could be that while theoretically, stoichiometric combustion might be most efficient for complete combustion, the water content in the chamber also increases with increasing O/F. While water does not contribute thrust, it takes up energy for vaporisation and heating. Running further CEA analyses showed that regardless of chamber pressure and concentration, the highest I_{sp}

is achieved with an equivalence ratio of about 1.10 to 1.15. This of course further increases the combustion temperature, negatively effecting the wall. In terms of emissions, an increased value of Φ also leads to more unburnt fuel released into the atmosphere.

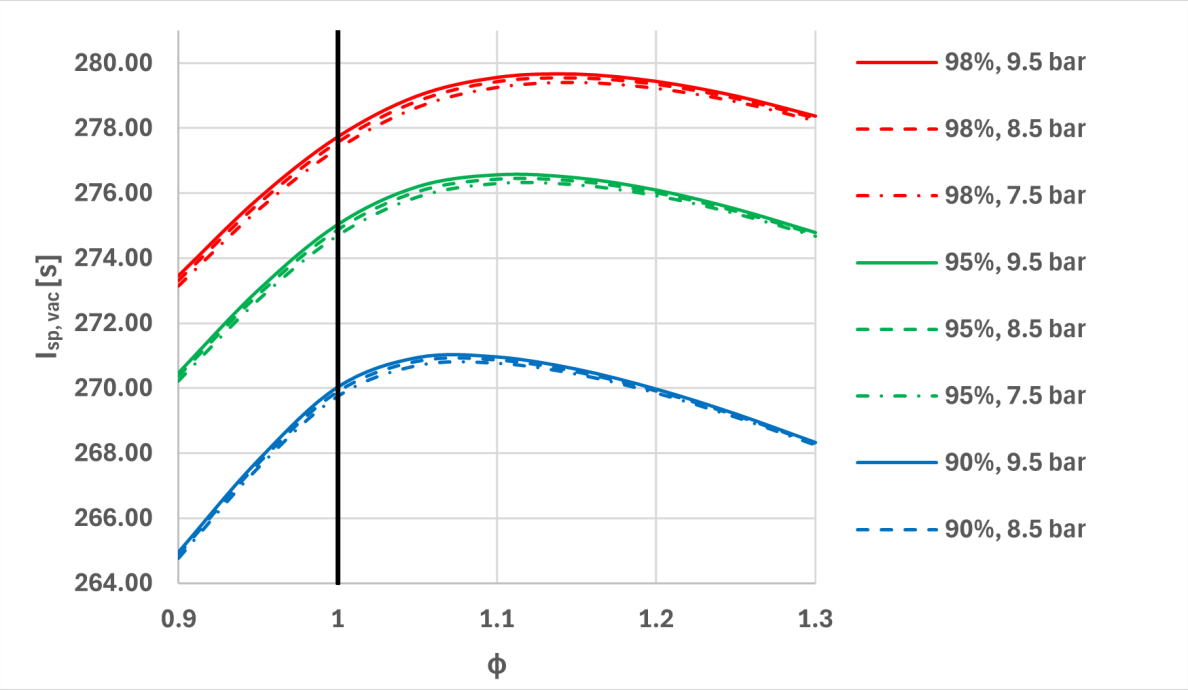

Figure 4.6: $I_{sp,vac}$ versus Φ for different concentrations and chamber pressures, obtained from CEA

Although the fuel-rich mixtures, i.e., mixtures with $\Phi > 1$, showed elevated temperatures compared to lower equivalence ratios, their temperatures appeared to be tolerable by the engine. This was only an assumption, as the real wall temperature could not be inferred directly from the chamber temperature. In the following, both the highest performing concentration, $\alpha = 0.98$ as well as the slightly lower concentration of $\alpha = 0.95$ with a lower expected temperature were analysed. To see the difference between stoichiometric and higher performance mixture ratios, equivalence ratios of 1.00 (stoichiometric ratio) and 1.10 to 1.15 (highest I_{sp} ratio) were considered. Finally, all previously considered injectors, the coaxial injector, the impinging injector and the pintle injector, were to be compared by simulating them with the mentioned propellant combinations (Table 4.7).

Table 4.7: Overview of the simulations to be performed; $I_{sp,vac}$ is given for a chamber pressure of $7.5bar$

Injector Type	α	Φ	O/F	$I_{sp,vac}[s]$	$\dot{m}$ $[10^{-3}\ kg]$	**Identifier**
Coaxial	98%	1.00	7.39	277.4	36.75	c98st
	98%	1.15	6.42	279.4	36.50	c98hp
	95%	1.00	7.62	274.7	37.12	c95st
	95%	1.10	6.93	276.3	36.89	c95hp
Impinging	98%	1.00	7.39	277.4	36.75	i98st
	98%	1.15	6.42	279.4	36.48	i98hp
	95%	1.00	7.62	274.7	37.12	i95st
	95%	1.10	6.93	276.3	36.89	i95hp
Pintle	98%	1.00	7.39	277.4	36.75	p98st
	98%	1.15	6.42	279.4	36.48	p98hp
	95%	1.00	7.62	274.7	37.12	p95st
	95%	1.10	6.93	276.3	36.89	p95hp

4.2.7. Boundary Conditions

Walls

The momentum wall boundary condition was set as a standard roughness stationary wall with no-slip condition.

As the wall temperature is coupled with the flow properties, it is generally not known a-priori and changes over time. From a steady-state analytical analysis, an estimation could be made, but this would overestimate the wall temperature during start-up, thus artificially adding energy to the chamber rather than dissipating it before the flow reaches a steady state. Assuming an adiabatic wall on the other hand would remove the dissipation of heat through convection, radiation and, to a small extent, conduction, hence leading to an overestimation of the engine at all phases from startup through to shut-down. Other ways of modelling the thermal boundary are available, setting, for example, heat transfer coefficients rather than a temperature. Since convection was expected to be the dominant heat transfer mechanism (see Section 2.2.3), the heat transfer coefficient could have been approximated by using the convective heat transfer coefficient, but that property depends on the flow properties and for this case has not been analytically pre-determined.

For that reason, simulations were only run with with adiabatic walls and with several different temporally constant wall temperature boundary conditions (Figure 4.7): A constant wall temperature of $300K$ (that being a slightly elevated ambient temperature), a constant wall temperature of $1,800K$ (that being the maximum expected wall temperature), and a 10th order polynomial temperature profile (as function of x) based on a steady state analysis performed at the research group. However, this steady-state profile was assumed to be reached only after approximately 10 seconds, which is the maximum foreseen firing duration, and hence also overestimates the wall temperature. Comparing the results of the temperature boundary simulations and the adiabatic wall simulation showed that deviations in temperature, pressure and velocity were within 2% between the simulations. Hence, for simplicity and in line with most simulations found in literature, the walls were assumed to be adiabatic.

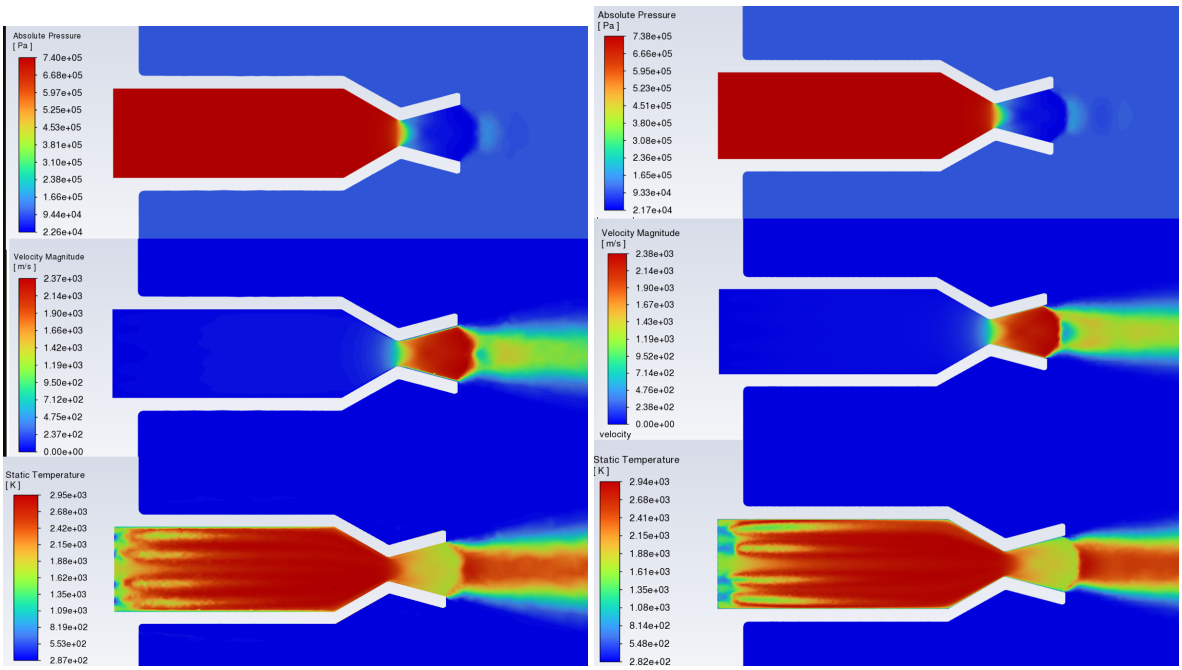

Figure 4.7: Pressure, velocity and temperature contours; Left: $T_{wall} = f(x)$; Right: $T_{wall} = const.$

The injector plate material was assumed to be aluminium. The material of the remaining walls was defined as UHTCMC as described in Section 4.1.1

Inlets

The inlet temperature for both propellants was set to $T_{ox} = T_{fuel} = 300K$. They were injected as droplets from the applicable surfaces. Inlet pressure was twice the target chamber pressure, i.e., $p_{ox} = p_{fuel} = 15bar$.

Since no continuous phase mass flow was injected from the inlets but only discrete phase parcels, the inlets were defined as mass flow inlets with 0 mass flow but the gauge pressure mentioned above.

Outlet

Since initial engine tests will be run on ground, operating conditions were set to standard sea-level conditions, i.e., $T_{op} = 288.15K$, $p_{op} = 101325Pa$ and $g_0 = 9.81\frac{m}{s^2}$. Gravity acts orthogonally to the flow direction. Reverse flow was enabled. For simplicity, the atmosphere was considered to consist of 79% nitrogen and 21% oxygen.

Since the atmosphere has an impact on the flow during start up, in the subsonic parts of the nozzle and the exhaust, it needed to be considered in the simulation as well. Scaling the farfield, i.e., the simulation boundaries, to approximately 20 times the maximum dimension of the geometry of interest is often recommended as a rule of thumb. Using the chamber dimensions and this guideline, a farfield with length and radius of $2520mm$ and $350mm$, respectively, was chosen. It was found that approximately 15 times the chamber length appears sufficient to not see any change in flow parameters anymore.

In Fluent, the borders of the domain were defined as Pressure Outlet with 0 gauge pressure, i.e., total pressure equal to atmospheric pressure.

To ensure there is no pressure wave reflection at the boundaries, the Acoustic Wave Model was enabled and the boundary condition set to *Non-Reflecting*. This led to divergence and was consequently disabled again. Regardless, the dimensions of the farfield should be large enough to not have an artificial pressure wave reflection in the domain.

4.3. Mesh Independence

In this section, the dependence of the results on the mesh resolution is investigated, thus verifying the mesh.

4.3.1. Preliminary Mesh

Preliminary simulations were performed in a domain with a diameter of $0.7m$ and a length of $1.64m$, split into $6,814,667$ elements with $1,258,995$ nodes and a minimum edge length of approximately $0.15mm$ (Figure 4.8, Figure 4.9, Figure 4.10). In a previous simulation, a larger domain was used and temperature and velocity contours were analysed. Where no change below a percent could be noted, the domain was cut to arrive at the current domain. Furthermore, the geometry was split to be able to apply different mesh sizes to different parts of the domain.

An unstructured mesh based on tetrahedrons was used throughout all simulations, as the more complex injector geometry could not be represented with hexahedrons with good quality, and switching from an unstructured mesh around the injector to a structured mesh further down stream led to unphysical values at the interface between structured and unstructured mesh.

Sizing was applied especially to the chamber and its faces to improve resolution in this area. Refinement was applied to the chamber walls.

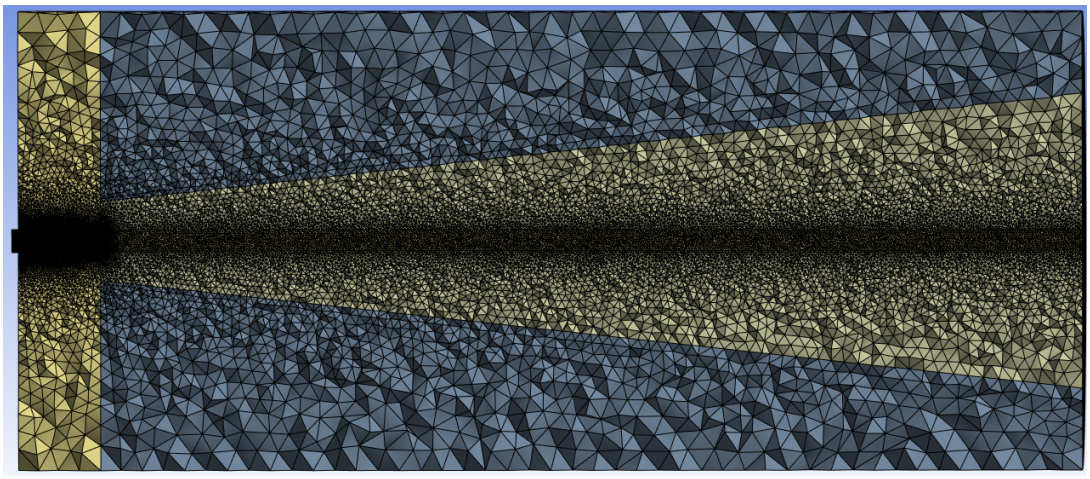

Figure 4.8: Cross section of mesh for preliminary simulations: Whole domain

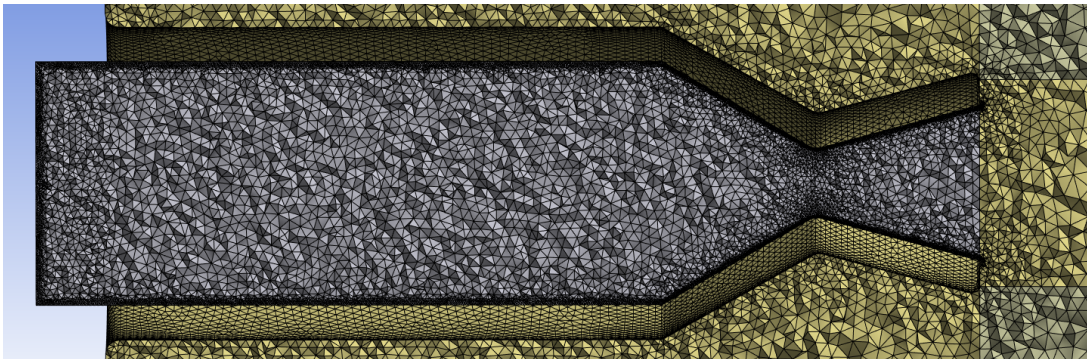

Figure 4.9: Cross section of mesh for preliminary simulations: Combustion chamber

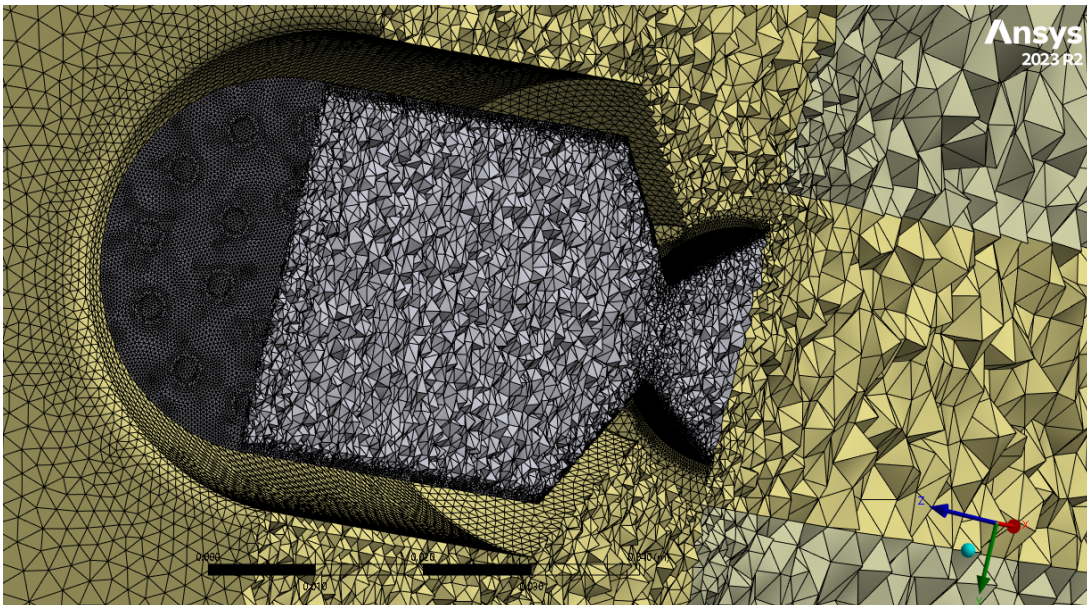

Figure 4.10: Cross section of mesh for preliminary simulations: Isometric view of the injector

4.3.2. Mesh Refinement

The setup (see section 4.2) and preliminary mesh described above were used for reference (*m1.0x*). All sizing parameters were decreased, i.e., refined, to 80%, resulting in a 50% higher element count (*m1.5x*) and increased, i.e., coarsened, to 120%, resulting in a 30% lower element count (*m0.7x*) compared to the reference mesh (Table 4.8).

Except for the sizing, all three meshes were setup the same way, using an unstructured method with tetrahedral elements and mesh refinement at the walls as outlined in Section 4.3.1. Since there were still differences in results between the reference mesh and the refined mesh, another mesh with half the element size (*m2.3x*) was setup. To be able to generate the mesh on the local machine, the wall refinement had to be lowered slightly. To still achieve good boundary layer resolution, an inflation layer was used. Subsequently, the mesh was processed with ICEM to remove any low-quality elements, resulting in a minimum orthogonal quality of 0.2, a maximum aspect ratio of 20, minimum skewness of 0.2 and minimum overall quality of 0.2. Two further refined meshes were generated to analyse the effect of introducing an inflation layer and its sensitivity (*m3.7x* and *m5.5x*).

Table 4.8: Mesh Independence Setup: Sizing (top) and Statistics (bottom); all dimensions in mm

	m5.5x	**m3.7x**	**m2.3x**	**m1.5x**	**m1.0x**	**m0.7x**
Injector Face	0.36	0.45	0.50	0.80	1.00	1.20
Central Farfield Body	1.06	1.32	2.00	3.20	4.00	4.80
Chamber Body	0.40	0.50	0.60	1.20	1.50	1.80
Throat Face	0.13	0.16	0.15	0.24	0.30	0.36
Nozzle Face	0.16	0.2	0.2	0.56	0.70	0.84
Chamber Face	0.28	0.35	0.50	0.80	1.00	1.20
Nodes (x10^6)	8.37	5.62	4.62	1.93	1.26	0.91
Elements (x10^6)	37.23	25.31	15.59	10.45	6.81	4.95
Nodes Rel.	6.65	4.47	3.67	1.53	1.00	0.73
Elements Rel.	5.46	3.71	2.29	1.53	1.00	0.73

To allow for comparison, all simulations were run for 20 time steps à 50 iterations and a final time step for 500 iterations. All time steps were set to $\Delta t = 1\ ms$. 40 CPUs with a total of 160GB were used per simulation. Figure 4.11 shows the increase in runtime compared to the mesh size for the different meshes.

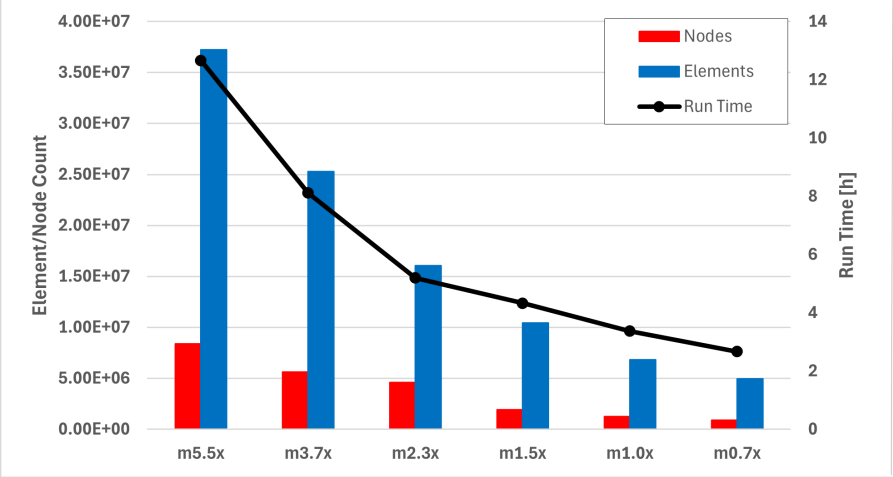

Figure 4.11: Node and Element Count and Runtime for different meshes

Table 4.9 shows that the increased mesh resolution led to increased performance, i.e., higher thrust, maximum temperature and pressure for the meshes with Refinement but to decreased performance for the meshes with Inflation Layers. With increasing resolution, the thrust further approached the expected value of $60.04\ N$, while the temperature deviated more from the value obtained with CEA, which could be attributed to the combustion model (see Section 4.4.3).

Table 4.9: Mesh Independence Results

	m5.5x	**m3.7x**	**m2.3x**	**m1.5x**	**m1.0x**	**m0.7x**
Run Time [h:m:s]	12:39:53	8:7:51	5:12:35	4:19:13	3:22:24	2:41:14
Residual (Cont.)	6.51e-01	7.50e-01	9.65e-01	8.40e-01	1.12e+00	1.55e+00
Residual (x-vel.)	8.51e-06	8.58e-06	6.88e-06	5.29e-06	7.49e-06	1.03e-05
Residual (Energy)	1.59e-04	1.86-04	1.76e-04	1.12e-04	1.51e-04	1.87e-04
F $[N]$	50.60	57.82	59.38	58.27	57.39	55.81
T_{max} $[K]$	3255.08	3181.41	3214.12	3107.22	3090.599	3071.705
p_{max} $[bar]$	6.47	7.18	7.34	7.52	7.55	7.55
v_{max} $[ms^{-1}]$	2067	2296	2345	2368	2395	2410

Further investigation showed that while the reference mesh reached steady-state within the 20 time-steps, the meshes with the boundary layer inflation required up to 30 time-steps. This explains the apparent decrease in thrust despite earlier mesh refinements leading to an increase in thrust. Thus, the two finest meshes were run for further time-steps to allow the simulations to reach steady-state, resulting in a final steady-state thrust of approximately $63N$ (see Chapter 5). The increase in element count by 47% between the coarse and fine mesh led to a change of maximum values of less than 1% (Table 4.10).

Table 4.10: Difference in maximum values for coarse mesh (m3.7x) and fine mesh (m5.5x)

	Coarse (m3.7x)	**Fine (m5.5x)**	**Deviation**
$v[m/s]$	2378.16	2400.38	0.93%
$p[10^5 Pa]$	7.64	7.67	0.30%
$T[K]$	3274.79	3274.83	0.00%
$F[N]$	62.86	63.22	0.57%

Plots for the different meshes for wall shear stress, wall absolute static pressure and wall temperature (Figure 4.12, Figure 4.13 and Figure 4.14) were evaluated to not only consider maximum values but changes throughout the chamber. Properties were evaluated at the walls to ensure the values were taken from the same location, as using a location in the mesh interior would lead to interpolation of values. The maximum values of wall shear stress, wall pressure and wall temperature deviated less than a percent from each other. Higher deviation was visible only in the wall temperature after flow separation. This was considered acceptable, since the wall temperature at the nozzle exit was low and not relevant for dimensioning.

A further increase in mesh resolution was considered unnecessary because of the low change in results. Due to time constraints, the final simulations (Chapter 5) were run in parallel to the final mesh study simulations, which is why the finer mesh was selected for those simulations in case a significant change would have been observed.

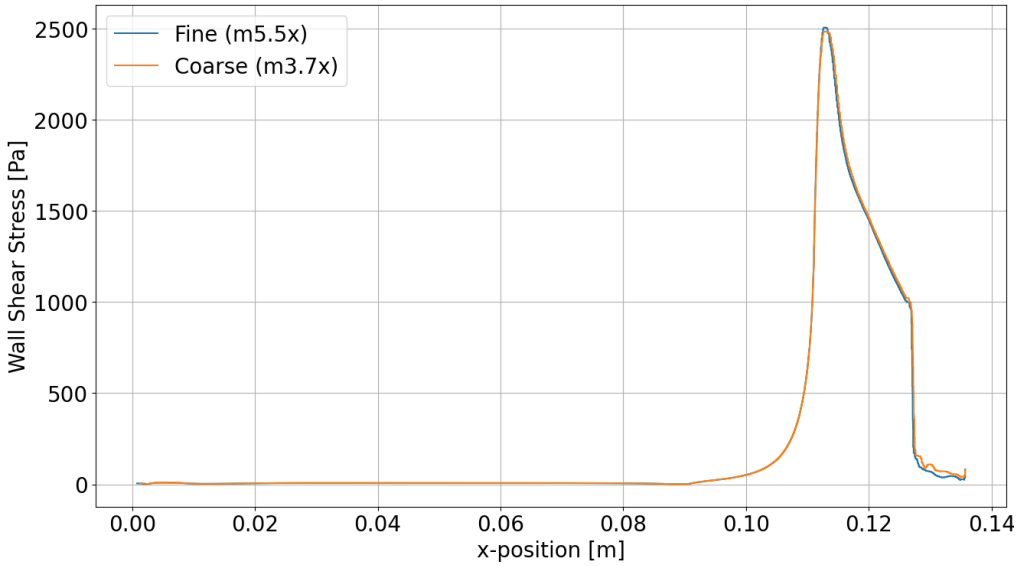

Figure 4.12: Wall Shear Stress plots along the x-axis for fine (*m5.5x*)and coarse ($m3.7x$) mesh

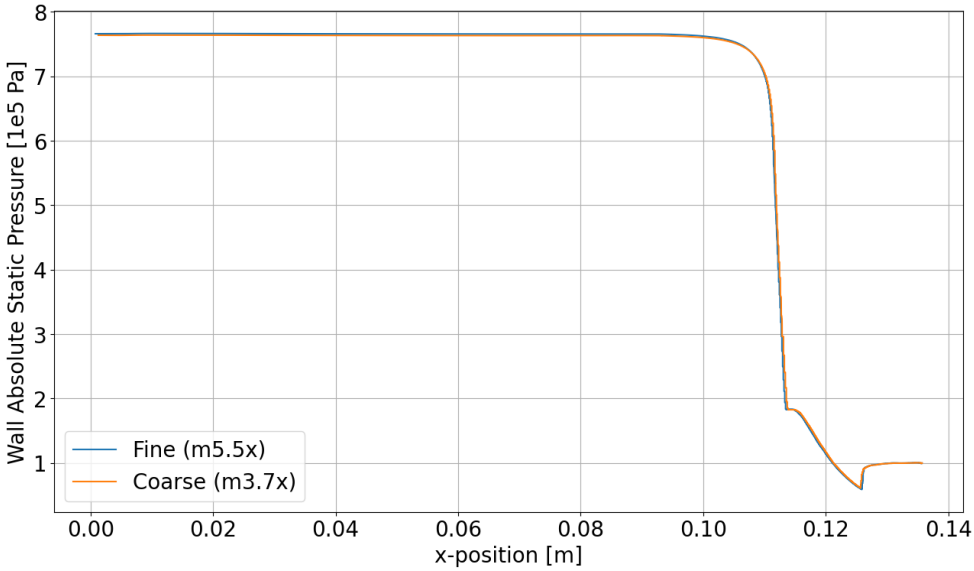

Figure 4.13: Static Absolute Pressure plots at the Wall along the x-axis for fine (*m5.5x*)and coarse ($m3.7x$) mesh

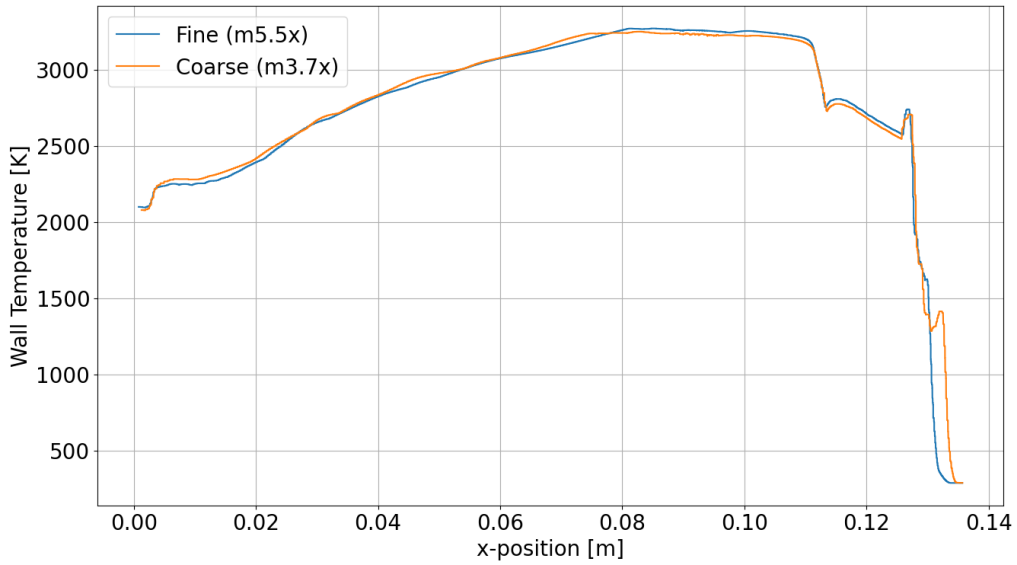

Figure 4.14: Wall Temperature plots along the x-axis for fine (*m5.5x*)and coarse ($m3.7x$) mesh

The final mesh is shown in Figure 4.15, Figure 4.16 and Figure 4.17.

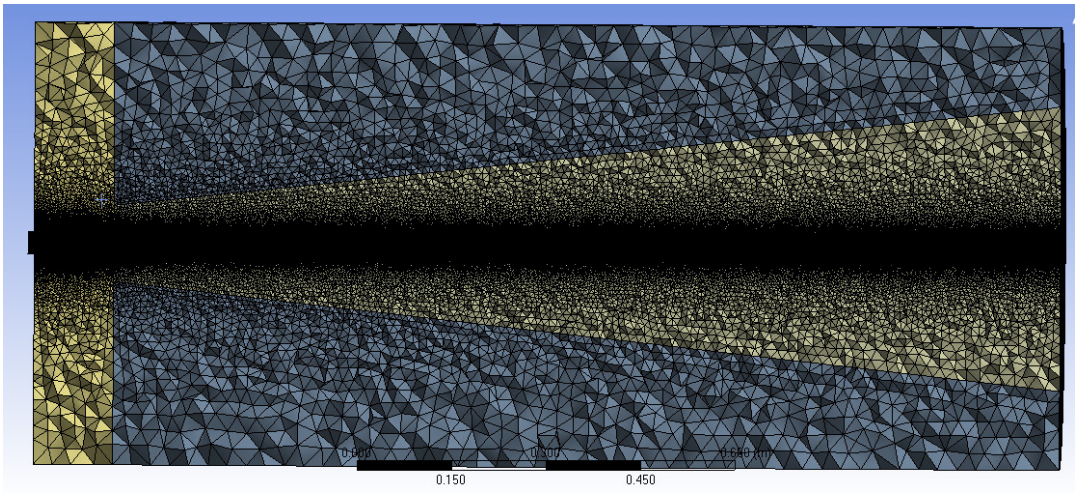

Figure 4.15: Cross section of final mesh: Whole domain

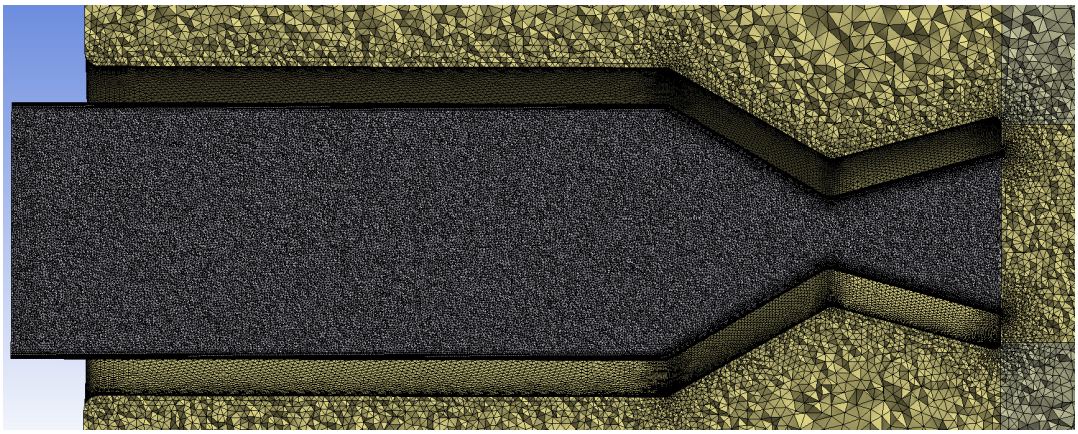

Figure 4.16: Cross section of final mesh: Chamber

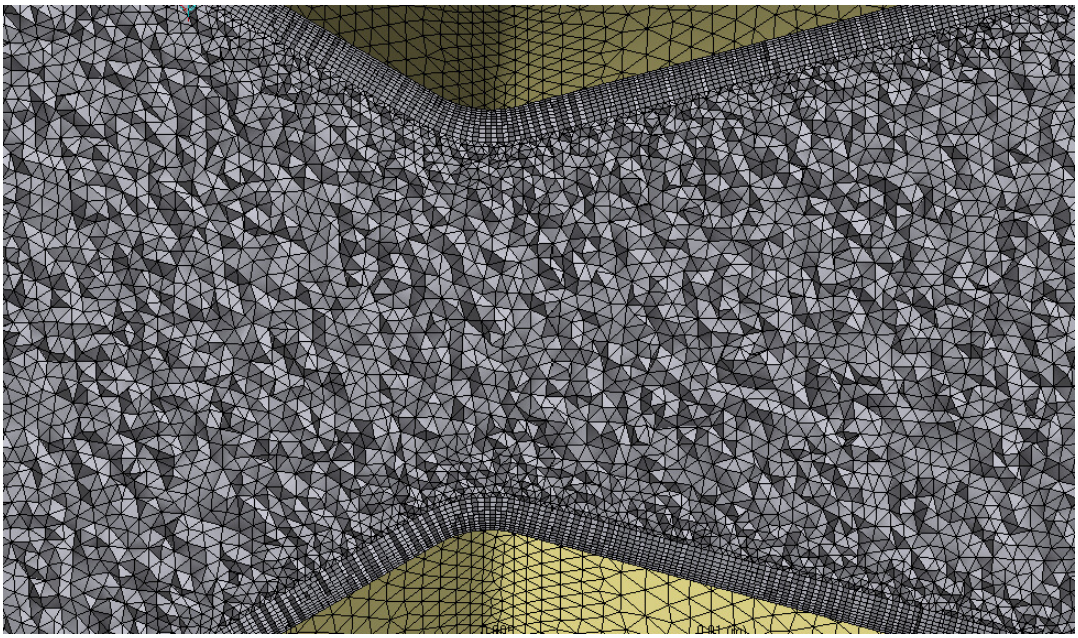

Figure 4.17: Cross section of final mesh: Throat; $D_t = 10mm$, 10 inflation layers with a minimum thickness of $0.05mm$; element size in the centre is approx. $0.4mm$

Figure 4.18 depicts the improvement in results between the original mesh and the final mesh on the example of the temperature contour.

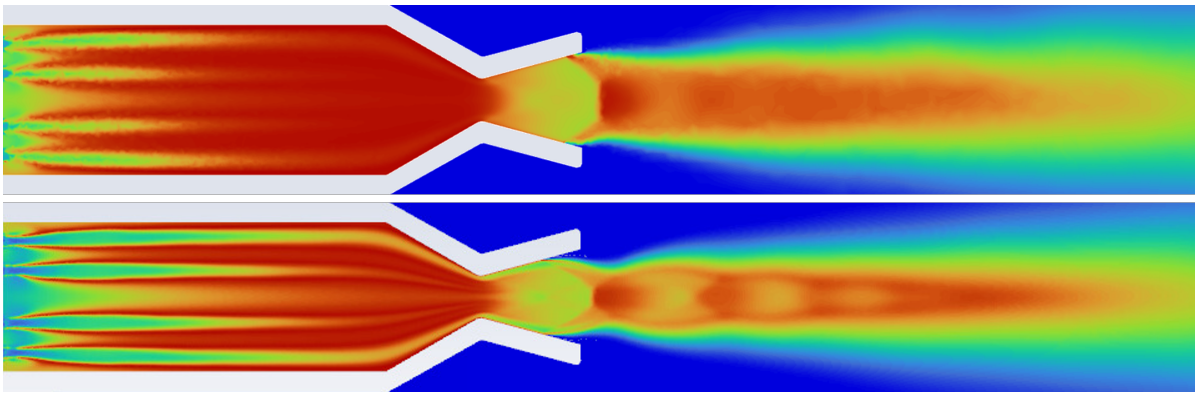

Figure 4.18: Temperature contour for the original mesh (top, 1.26M nodes) and the final mesh (bottom, 8.37M nodes)

4.3.3. Effect of Time Step Size

In addition to mesh independence, i.e., independence from spatial resolution, time-step independence, i.e., independence from temporal resolution, was considered. Figure 4.19 shows the thrust curve for different meshes and different time steps. While the thrust curve for the default mesh (*m1.0x*) is monotonously rising, the refined mesh (*m2.3x*) already shows a decrease in thrust shortly after startup, which becomes more prominent with the finest mesh (*m5.5x*). With increasing mesh resolution, the thrust needs more time to build up and the final value is higher.

With the finest mesh, two simulations were run for 58 time steps but different time step sizes, i.e., the default simulation with $\Delta t = 1.0ms$ and $58ms$ and the simulation with the reduced time step of $\Delta t = 0.5ms$ and $29ms$. Both simulations reached approximately the same final thrust value and the same graph contour was visible, but the reduced time-step led to two times faster build-up of thrust. This could be due the relaxation factors applied, which limit the change in any variable between two iterations to a fraction of the calculated value. For example, the pressure relaxation factor was set to 0.3 as per recommendation by Ansys to improve solution stability. If between iterations the change in pressure was calculated to be $100Pa$, the value would only be changed by $30Pa$, i.e., 0.3 of the estimated value. While the end-result would be the same, more iterations would be required to achieve it. Hence, if a reduced time-step was used but the number of iterations per time-step remained constant, a faster build-up of the combustion could be expected. This difference in results could be mitigated by allowing more iterations per time-step. Hence, for the simulations run here, time-step independence was not given. Since the final thrust values and the qualitative contours matched while the exact transient behaviour could not be quantified regardless due to lack of availability of Arrhenius parameters, the agreement was considered sufficient.

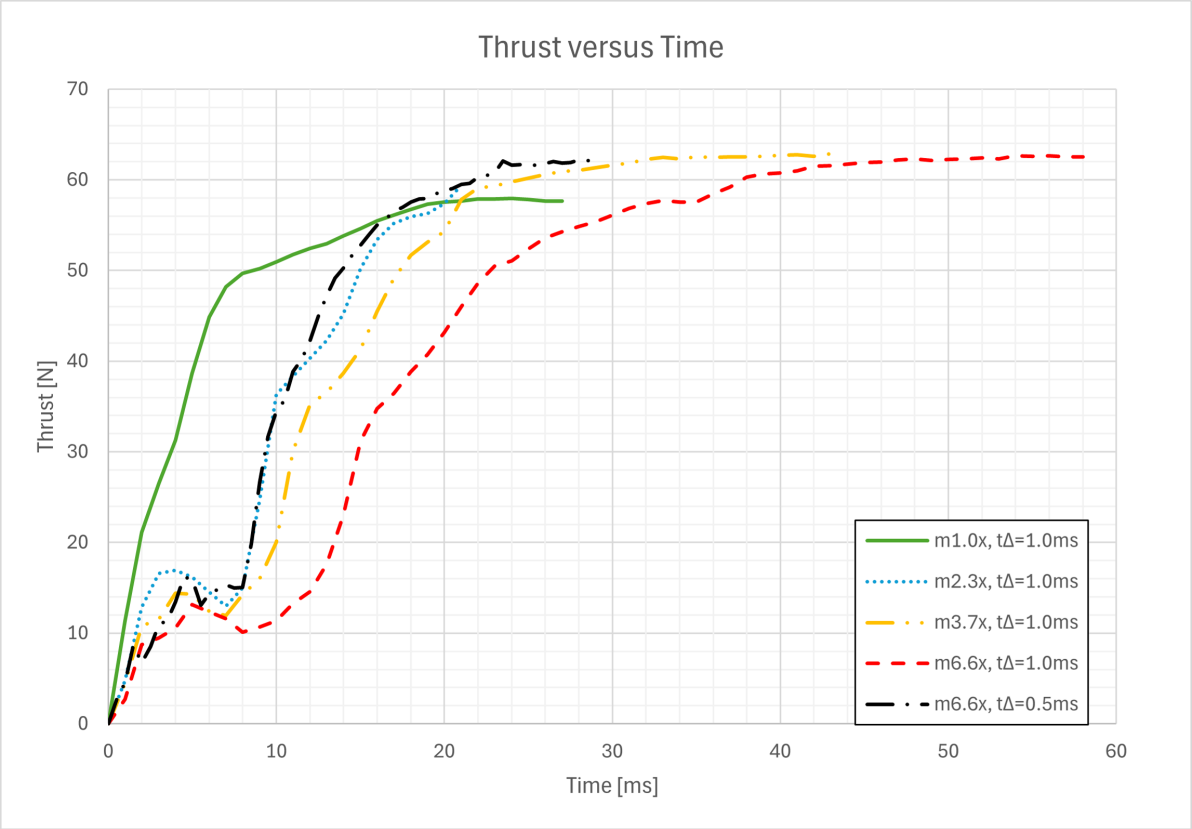

Figure 4.19: Thrust versus Time for different meshes and time-step sizes

4.4. Validation

4.4.1. Validation Cases

The primary approach to validate the simulation setup was numerically replicating experimental works on similar engines by other researchers. Two papers were found with sufficiently similar engines and detailed descriptions of the experimental setup.

In the first paper, HTP is used with Stock 2 (hydrocarbon blend and catalyst), with a chamber geometry very similar in shape and dimensions. The engine employs an impinging-jet injector and aims for a thrust of 500 N. In the following, this will be referred to as *case 1* or *impinging engine* .

In the second paper, HTP is used with Block 0 (methanol and catalyst). The chamber has a similar volume but different proportions. A pintle injector is used and the design thrust is 663 N. In the following, this will be referred to as *case 2* or *pintle engine*.

The setup with a coaxial injector previously described in Section 4.2.1 will be referred to as *case 0* for the sake of comparison.

Case 1 - Impinging Jet Injector

The first validation case was based on experimental work performed at the Korea Advanced Institute of Science and Technology (KAIST) [51, 52].

Their engine uses 90% hydrogen peroxide with Stock 2, a hydrocarbon fuel consisting of tetraethylene glycol dimethylether, tetrahydrofuran and toluene with sodium borohydride as catalyst to induce hyper-

golicity with the HTP. The exact composition was not provided. The fuel material properties differ from the properties of kerosene, but for simplicity, kerosene was used in the validation simulation. Since the stoichiometric ratio of kerosene/HTP differs significantly from the O/F given in the paper, the simulation was run both with the original O/F and with the O/F resulting from stoichiometric combustion of kerosene and HTP.

Chamber dimensions are $32.5mm$ diameter and $80.2mm$ length. The injector is an unlike pentad impinging injector. Although the chamber geometry is similar to that of the Greenlam engine (section 4.1), the nominal thrust is $500N$, i.e., five times higher. The inlet pressures are approximately $32bar$ and $38bar$ for oxidiser and fuel, respectively. Since the DPM setup in Fluent requires an inlet velocity rather than inlet pressure, an estimate for the inlet velocity was obtained using Equation 4.4 [7].

$$\dot{m} = \rho \, A \, v \tag{4.4}$$

The setup is shown in Figure 4.20, Figure 4.21 and Table 4.11. The injector is shown in more detail in section 4.1. For further details, see section A.3.

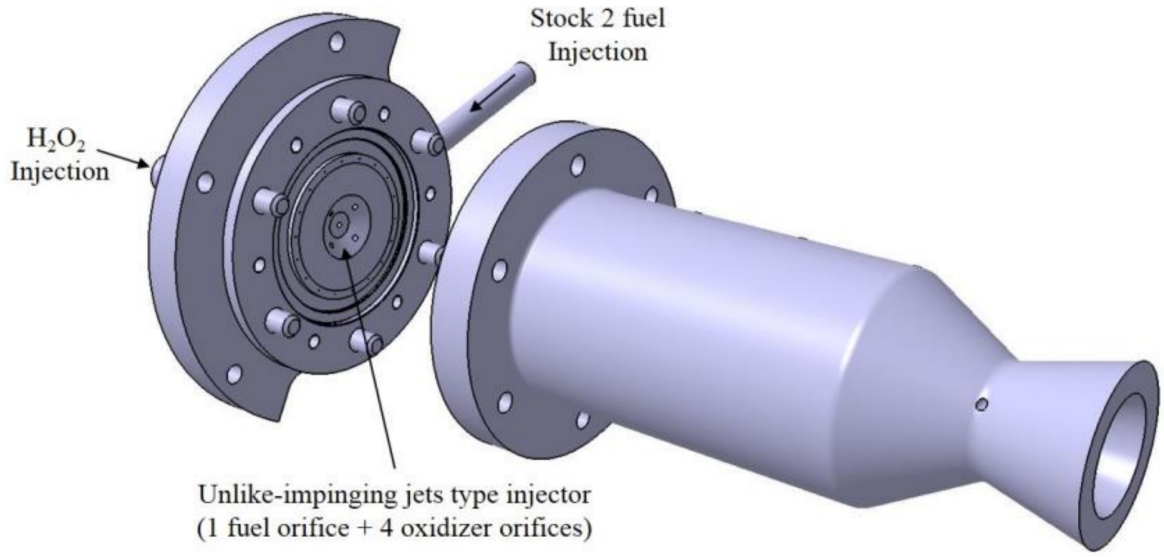

Figure 4.20: Chamber geometry of the impinging engine [52]

Table 4.11: Injection properties for validation case 1 [51]

Fuel	Injector pressure	38	bar
	Mass flow rate	24	g/s
	Injection velocity (derived)	26.2	m/s
	Inlet diameter	1.20	mm
	Inlet temperature (assumed)	300	K
Oxidiser	Injector pressure	32	bar
	Mass flow rate	131.4	g/s
	Injection velocity (derived)	19.1	m/s
	Inlet diameter	1.25	mm
	Inlet temperature (assumed)	300	K

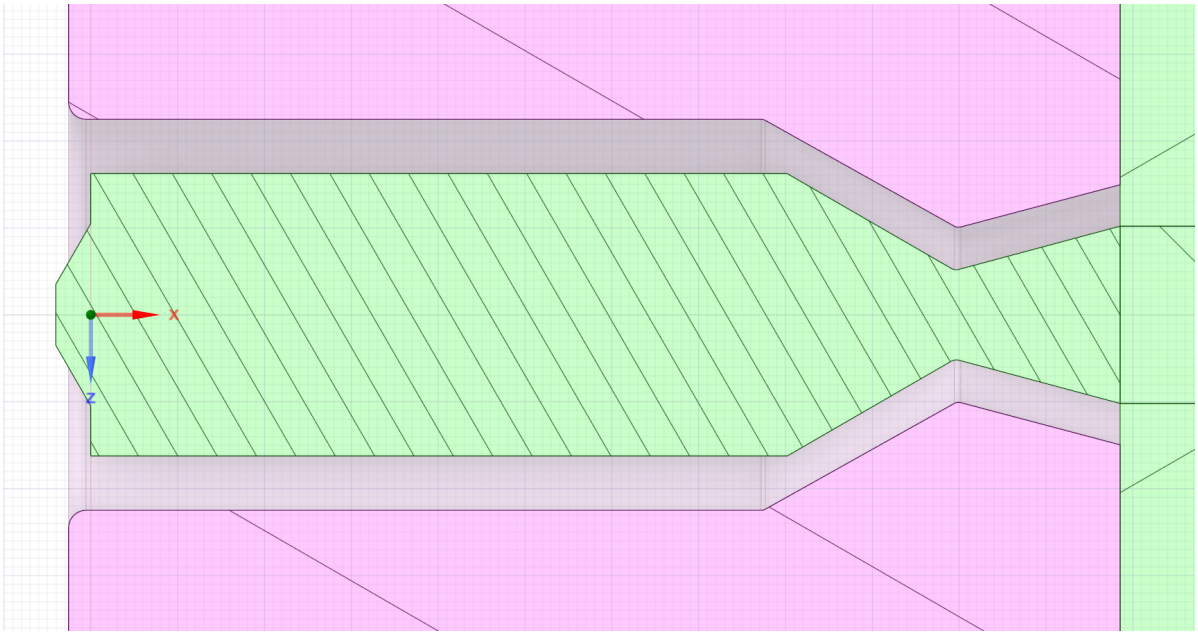

Figure 4.21: Impinging engine implemented in CAD

Case 2 - Pintle Injector

The second validation case was based on experimental work jointly performed by IN Space LLC and Purdue University [53]. They use the methanol-manganese oxide blend Block 0 as fuel and 90% HTP as oxidiser. The exact composition of the Block 0 is not given in the paper and varies between sources. According to [60] it consists of 78% Methanol and 22% Manganese(II) acetate tetrahydrate. The pintle injector features 32 injection holes at the lower part of the pintle for fuel injection, leading to radial outflow, and an annulus located at the base of the pintle for oxidiser injection, leading to axial flow.

The experimental setup for the pintle engine [53] is shown in Figure 4.22, Figure 4.23 and Table 4.12. The injector is described in more detail in section 4.1. More detailed parameters are provided in section A.3.

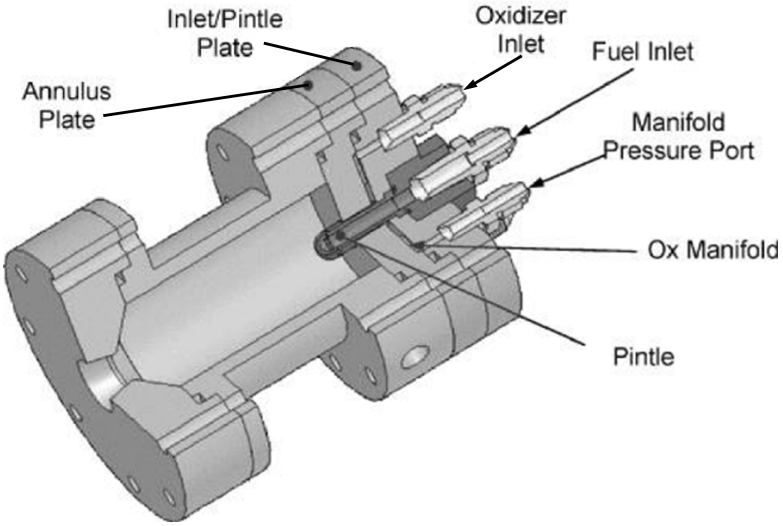

Figure 4.22: Chamber geometry of the pintle engine [53]

Table 4.12: Injection properties and engine geometry for validation case 2 [53]

Design Parameters		
Oxidiser	90% H2O2, 10% H2O	
Fuel	CH_3OH, Mn_3O_4	
General		
Vacuum thrust	662.7848	N
Vacuum specific impulse	231	s
Chamber pressure	27.57904	bar
Mass flow rates		
Oxidiser	0.213642	kg/s
Oxidiser injection velocity	8.65632	m/s
Fuel	0.078018	kg/s
Fuel injection velocity	14.35608	m/s
O/F	2.74	$-$
Chamber		
Chamber diameter	44.3484	mm
Chamber length	76.2381	mm

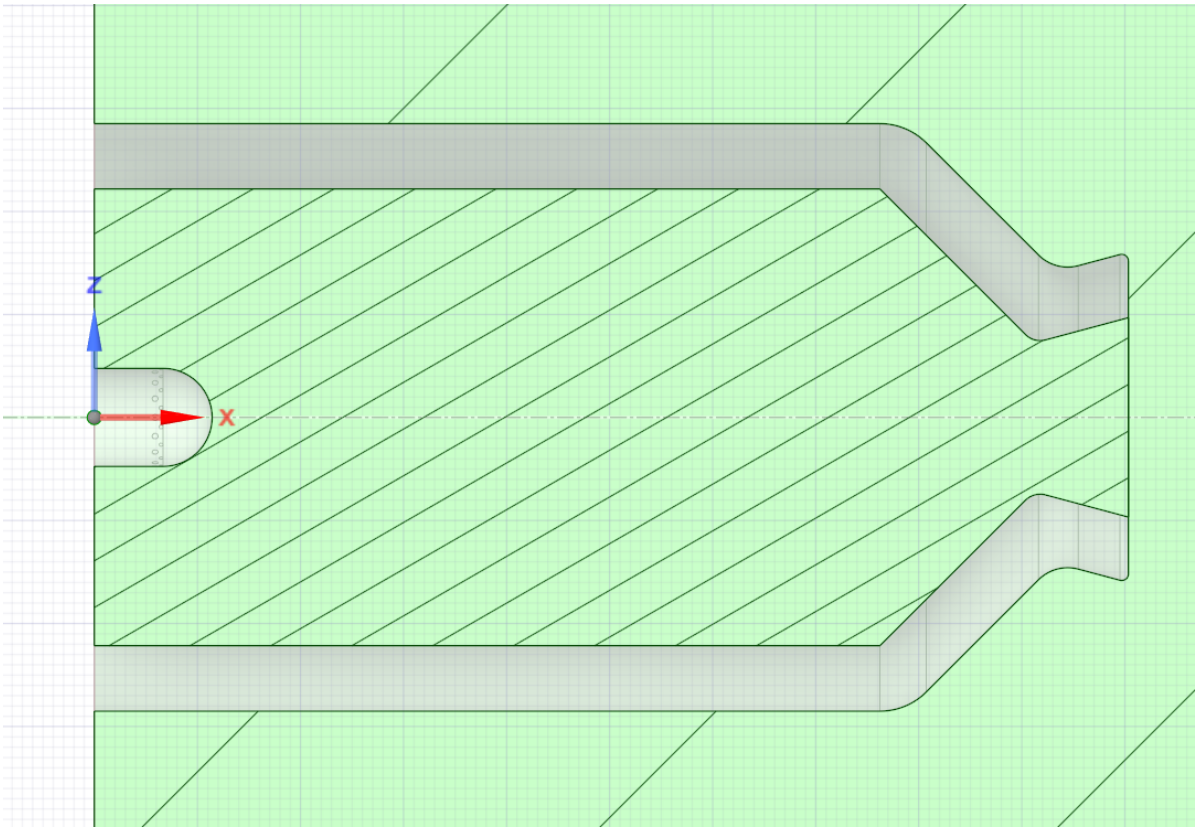

Figure 4.23: Pintle engine implemented in CAD

4.4.2. Intermediate Results & Model Adaptations

Reproducing the results of the experimental papers with an impinging-jet injector and a pintle injector by using the setup described in section 4.2, only changing geometry, boundary conditions and propellant parameters, was not successful. Since the Greenlam engine configuration somewhat differs from the two papers above, changes were made to the original simulation setup (*case 0*) to take into account the differences, most notably the different injector types, i.e., pintle or impinging-jet instead of coaxial

injectors, the different injection parameters, e.g., mass flow rate and velocity, and the different fuels with different material parameters, e.g., density, vapor pressure and reaction rates.

Injector Configuration & Injection Parameters

The major difference between the injectors in the validation cases and in the *case 0* simulations was how they distribute propellant. The coaxial injectors were distributed evenly over the injector plate, with each individual injector inserting both fuel and oxidiser. Thus, when entering the chamber, the propellants were already quite distributed over the chamber radius and the mixing itself happened due to the difference in inertia of the propellant streams. In contrast, both validation injectors had only one central injector element (although several orifices) and relied primarily on the fuel and oxidiser jets impinging on each other to initiate breakup and atomisation (see Figure 4.24).

Figure 4.24: Cold-flow test of impinging jet injector showing atomisation [51]

The original setup did not include droplet collision. Realising that the validation cases relied on this collision, stochastic droplet collision and breakup models were enabled. Since collision in Fluent can only happen between the same species or mixture, all propellants were defined within the same mixture, defining the exact compositions only in the Component tab, e.g., setting the mass fraction of H_2O_2 and H_2O to 0 for the fuel injection.

The Stochastic Collision model is mostly applicable for low Weber numbers ($We < 100$). It can be strongly time-step and mesh dependent, as it is determining the probability of collision of any two particles that are in the same mesh cell at the same time [32].

Several breakup models are available. The default model for low Weber numbers is the TAB (Taylor Analogy Breakup) model. More appropriate for high Weber numbers ($We > 100$) is the Wave model, where breakup is mostly related to the relative velocity between a droplet and its surrounding medium [39].

The Weber number (Equation 4.5) relates a droplet's inertia to its surface tension.

$$We = \frac{\rho v^2 D}{\sigma} \tag{4.5}$$

With approximate densities of $\rho_{ox} = 1400kg/m^3$ and$\rho_{fuel} = 810kg/m^3$ and surface tension coefficients of $\sigma_{ox} = 0.026N/m$ and $\sigma_{fuel} = 0.078N/m$ for oxidiser and fuel, respectively, the injection velocities v and droplet diameters D equal to orifice diameters given in Table 4.11, the Weber number is orders of magnitude higher than 100, i.e., the inertia dominates the surface tension and the Wave model is applicable. This regime is outside of the optimal range for the Stochastic Collision model, but no other droplet collisions are available in Ansys Fluent. On the other hand, if droplets are injected with with a size of $10^{-6}m$ to $10^{-5}m$ ($We < 100$), assuming primary breakup happened before injection, both the TAB and Stochastic Collision model are applicable. Droplet injection diameters are discussed below.

To improve the modelling of the droplets' interaction with the wall, all DPM wall boundary conditions were set to *wall-jet*. While the default condition *reflect* reflects particles as if the impact was purely elastic, this boundary condition determines the post-impact velocity and direction based on impingement angle and Weber number. This can result not only in reflection but also make the particle stick to the wall [32]. Figure 4.25 shows the velocity profiles for *case 1* with two different injection velocities, i.e., the injection velocity provided in the source and half that value.

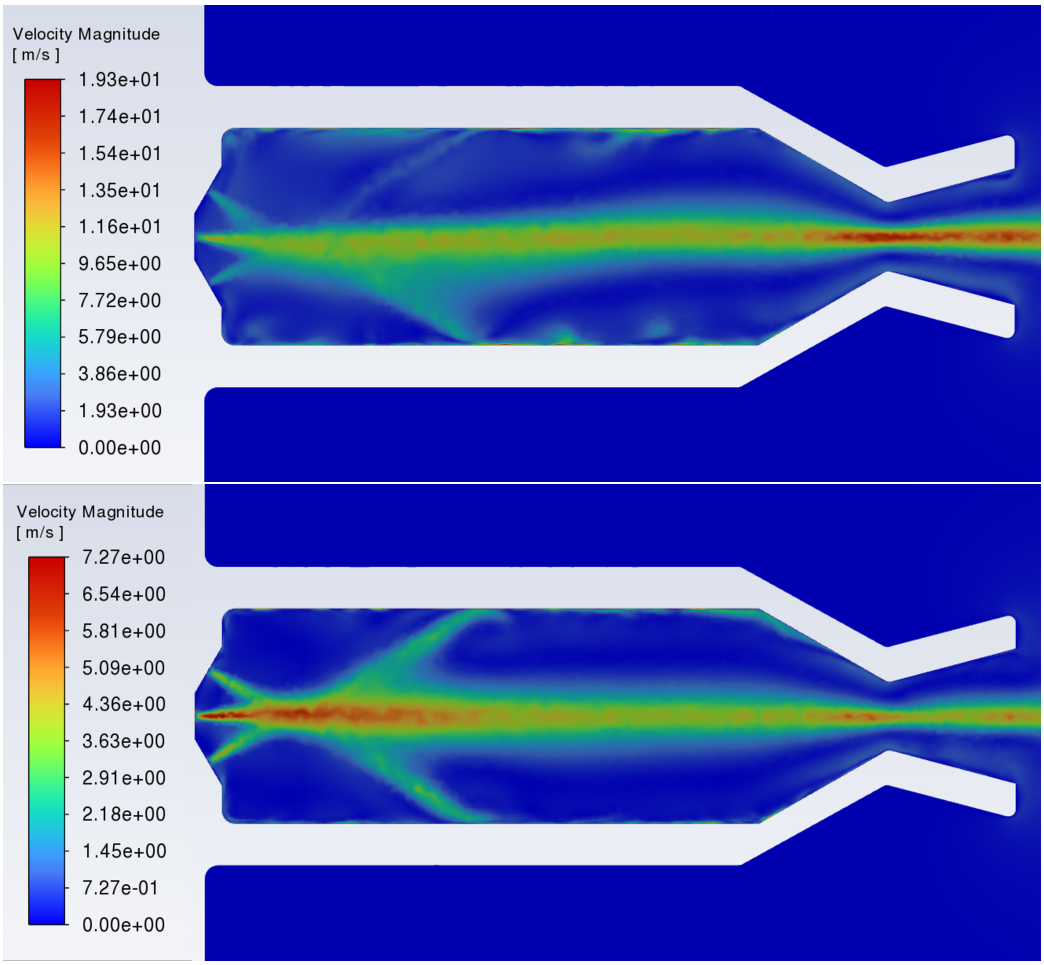

Figure 4.25: Velocity profiles for Case 1 with original (top) and lowered velocity (bottom)

While some collision and mixing can be seen, most of the particles continued on their path defined by the injector without interacting with the other jets. This could be due to the temporal and/or spatial resolution of the simulation, as discussed above. Higher collision rates can be seen with lower injection velocities, but these lower velocities contradict the information given in the paper and the collision rates are still insufficient. The axial asymmetry in the graphs might be due to gravity acting in negative z-direction.

The injection velocities in *case 2* were lower, which could explain why there was much more of a spray formation visible (Figure 4.26). Still, an unexpected strong radial fuel jet persisted.

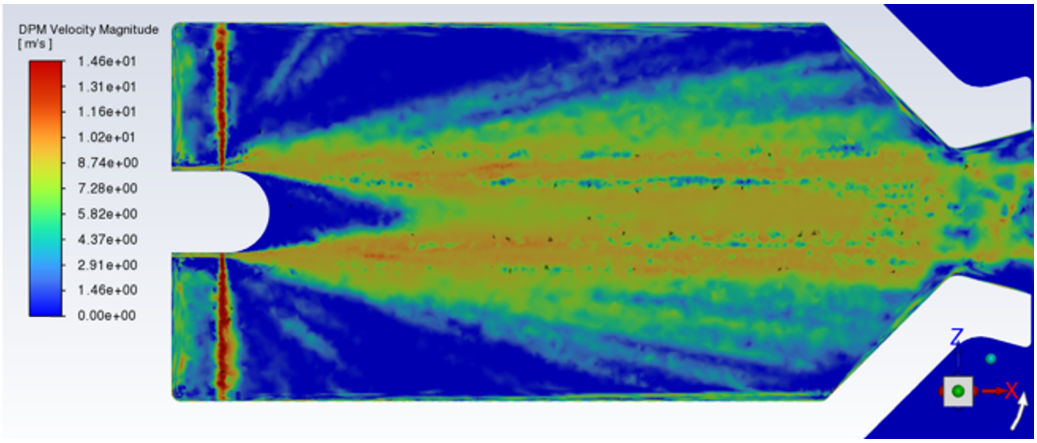

Figure 4.26: Velocity profile for Case 2

Both cases showed elevated temperatures, but no ignition. Neither of the cases were stable, they diverged a few time-steps after the time of the screenshots due to accumulation of particles at the wall and the static pressure exceeding the limits at that location.

As described above, the DPM setup in Ansys fluent requires mass flow rate and inlet velocity as input. Hence, addressing the different injection conditions was very straightforward and could be done by changing the numerical values in the DPM injection tab in Ansys Fluent.

Another relevant parameter is the droplet size of the injected fluid. By default, droplets are injected with a uniform diameter. If the injection is supposed to represent a liquid jet, the droplet size can be set equal to the orifice diameter of the jet [39]. Since break-up of jets, i.e., primary breakup, is often difficult to model, the initial droplet size can be set as if the primary breakup had already happened. Commonly, a Rosin-Rammler distribution is used for this [61], a probability distribution that takes as input the minimum, mean and maximum diameter of the droplets, by default on the order of microns to hundreds of microns. However, these values need to be verified experimentally for accurate results.

Simulations were run with different droplet diameters:

- uniform: default diameter of $0.0001m$
- uniform: diameter equal to the orifice diameter of each propellant
- distributed: default minimum, mean and maximum diameters of $10^{-6}m$, $10^{-5}m$ and $10^{-4}m$ with a spread parameter of 3.5 (Rosin-Rammler)

It was found that increasing the droplet diameter up to the orifice diameter (but not beyond) significantly increased the stability of the solution. The reason for that could simply be that, for any given

mass flow rate, less particles needed to be tracked. Mixing of the propellants was not enhanced by choosing smaller diameters. As discussed above, changing the droplet diameter has an impact on the applicability of the collision and breakup models.

Consequently, changing the injection diameter was also considered for the original setup with a coax injector to see if it had an impact on either convergence or results. Figure 4.27 shows two contours with the same setup using the TAB breakup model, the only difference being the initial diameter of the injected droplets. Calculating the We number for both cases shows that for the right setup with higher droplet diameters ($We > 100$) the Wave model is more applicable. Running the same simulation with the Wave model resulted in different DPM mass source values but the same order of magnitude and a qualitatively identical contour. It was concluded that injecting particles with a diameter equal to the orifice diameter does not deliver reasonable results for the coax injector.

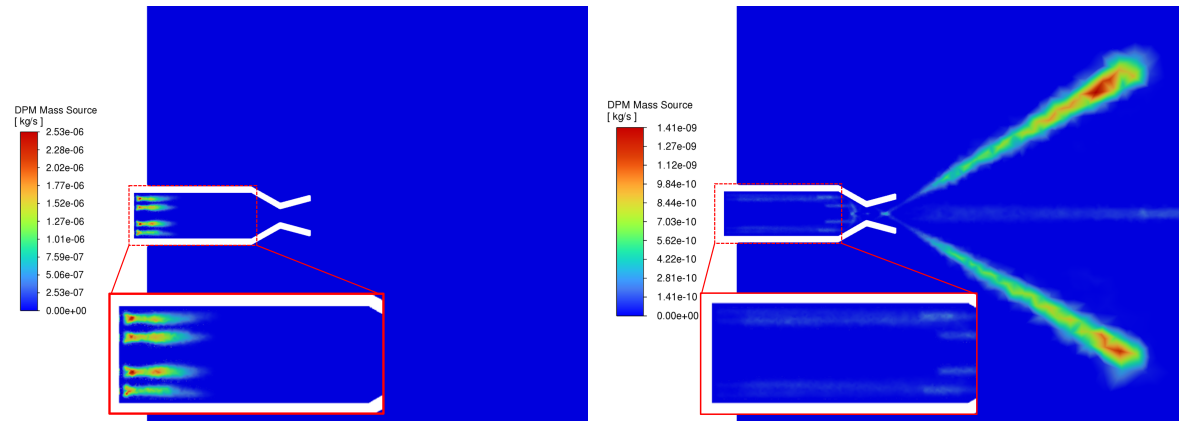

Figure 4.27: DPM Mass Source in original setup with Rosin-Rammler distribution and mean droplet size of $d_{fuel} = d_{ox} = 0.01mm$ (left) and uniform injection with $d_{fuel} = 1.20mm$ and $d_{ox} = 1.25mm$ (right)

While no definitive conclusions can be drawn from this for the two validation cases since they have a different mixing mechanism based on impingement, this finding supports the assumption that the high droplet diameter chosen for those simulations was one of the reasons they did not deliver the expected results, i.e., no sufficient droplet impingement and subsequent spray. As discussed, setting lower and distributed droplet diameters led to divergence for the validation cases.

Material parameters

For both *case 1* and *case 2*, the qualitative fuel composition was known, but the exact percentages were not given. Like kerosene, methanol which is the main compound of Block 0 (*case 2*) is predefined in the Ansys Fluent database, but the compounds of Stock 2 (*case 1*), namely tetraethylene glycol dimethylether, tetrahydrofuran and toluene, are not defined. The same goes for the catalysts in both cases. Finding sufficient material data for any of these materials was not possible, thus, strong simplifications had to be made. Block 0 was modelled as pure methanol but with a lower mass flow rate to account for the approximately 21% that are not in fact methanol. Stock 2 was modelled as kerosene, with a change in O/F to account for the different stoichiometry. These are strong simplifications that may have rendered the simulations unphysical.

Furthermore, Arrhenius parameters were only available for the combustion of oxygen with either kerosene or methanol. Specifically the ignition delay strongly depends on the reaction rate parameters, i.e., the activation energy and the pre-exponential factor of the reactions. As outlined in Section 2.1.3, an in-

crease in activation energy of 30% can lead to a decrease in reaction rate by a factor of three orders of magnitude. For any reaction involving hydrogen peroxide, estimates had to be made based on hydrogen peroxide decomposition with other catalysts, but real Arrhenius rate parameters for the specific reactions need to be found experimentally through, for example, drop tests.

Spatial and Temporal Resolution

The *case 0* simulations produced reasonable results with time steps of $1ms$, with even time-steps as high as $10ms$ delivering similar results. This was in line with [42, 62], stating that time scales smaller than milliseconds usually do not have an impact on rocket engine performance, whereas researchers at the faculty raised the concern that transient combustion simulations usually need to be run at time steps around 10^{-5} or 10^{-6} s to resolve turbulent and chemical processes. However, lowering the time-step below a millisecond did not improve stability, it merely delayed the divergence to a later time-step.

For *case 0*, a coarse, unstructured mesh (minimum edge length $\Delta x \approx 0.15mm$) without performing a mesh-independence study was used initially to be able to quickly test and run models on a personal computer and delivered acceptable results. An equivalent mesh was setup for the validation cases.

Observing pressure singularities near the walls, especially near the injectors and at edges like the intersection of injector plate and chamber or the intersection of chamber and divergent, it was tried to mitigate the pressure spikes by chamfering edges and by improving near-wall mesh resolution through use of inflation layers. It was also tried to double the overall mesh-resolution in the chamber. Neither approach helped in achieving a solution. It is possible that the model setup in general was viable, but time step and grid size insufficient, i.e., too large, to accurately capture the physics of droplet break-up, propellant mixing etc. Given that lower droplet diameters were necessary to achieve good results for the coax injector but led to divergence for both validation cases indicates that higher resolution and hence more resources are necessary for these cases to obtain results. Previous papers have reported that simulations for a two-dimensional case took weeks to run on a high performance computer [42, 49]. Consequently, running a similar setup with sufficient spatial and temporal resolution but in three dimensions might not be possible with the available resources.

Intermediate Conclusions

It appears that due to no droplet collision model being available for higher Weber numbers, engines with injectors that rely on jet impingement for propellant mixing cannot be simulated with the Discrete Phase Model, assuming the droplet diameter is equal to the jet diameter. If instead of a jet, the propellant condition is assumed to be post-primary-breakup and the injected droplets are much smaller, the Stochastic Collision model becomes applicable, but due to the high number of discrete particles to be tracked, the simulation is no longer possible to run with the available resources.

As discussed in Section 3.2.1, other researchers modelling transient Lagrangian combustion made use of more computational resources (number of CPUs and memory) [42, 49] and ran a single simulation for several weeks for it to converge, which in the scope of this research was not possible. A possible conclusion could be that more resources are necessary to solve the combination of models selected.

Given the little research done so far on this kind of engine, there is an overall lack of both numerical and experimental data available that could be used for validation. In the few available papers, not all information regarding geometry and materials was available, so assumptions had to be made. Hence, instead of lack of computational resources the simulations could have been unsuccessful due to lack of detailed information on propellant and boundary conditions.

Since the attempt to numerically reproduce experimental results by KAIST [51, 52] and Purdue University [53] was not successful, the validation needed to be simplified and was subsequently conducted with a rather qualitative comparison of results of this research to results of previous research on rocket engines and to the data generated with CEA (Section 4.4.3).

Since validation against impinging-jet and pintle injectors was not successful, the approach of simulating the Greenlam engine with these injectors was omitted and further simulations were conducted exclusively with the coaxial injector.

4.4.3. Qualitative Validation

Insight about the validity of the simulations with a coax injector could be gained by comparing specific performance indicators like thrust or exit velocity to values given by CEA, and by comparing trends in the engine to trends in other rocket engines, e.g., chamber temperature plotted over axial distance or the formation of Mach diamonds behind the exit.

Performance Indicators

Designing a thruster for operation in higher altitudes or in space means designing it for an ambient pressure significantly lower than $1atm$, or $101325Pa$. Assuming an orbit of $500km$ altitude, the exit pressure for ideal expansion would be less than $1\ \mu Pa$ (Table 2.6), or to simplify, approximately $0\ Pa$. If now the same engine with the same mass flow rates were tested on ground, the ambient pressure would be much higher, meaning the flow would be overexpanded and pushed inwards, i.e., towards the axis, by the atmosphere, potentially leading to flow separation before the exit. Considering Equation 2.1, extended for non-ideal expansion (Equation 4.6) [7], the relationship between specific impulse and exit velocity (Equation 4.7) [7], and the difference in specific impulse between sea-level and vacuum (Table 4.6), leads to an expression to estimate the thrust that can be expected for an engine designed for space but tested on ground (Equation 4.8).

$$F = \dot{m}\ v_e + (p_e - p_a)\ A_e \tag{4.6}$$

$$I_{sp} = \frac{v_e}{g_0} \tag{4.7}$$

$$\frac{F_{sl}}{F_{vac}} = \frac{I_{sp,sl}}{I_{sp,vac}} + \frac{(p_{e,sl} - p_a)\ A_e}{\dot{m}\ g_0\ I_{sp,vac}} \tag{4.8}$$

Assuming a concentration of 98% HTP, stoichiometric combustion and a chamber pressure of $7.5\ bar$ resulted in the performance given in Table 4.13, according to CEA.

Table 4.13: CEA input for Qualitative Validation

$I_{sp,vac}$	$277.36\ s$
$I_{sp,sl}$	$246.46\ s$
O/F	7.3882
T_c	$2786.66\ K$
p_e	$27934\ Pa$
Ma_e	2.642
v_e	$2417.3\ m/s$

The Python script produced in this research (section A.1) calculated $O/F = 7.3750$. The slight deviation from the CEA value might be due to CEA assuming a different formula for kerosene. Since both the

script and Fluent use the same formula, the latter value was used to derive the mass flow rates:

$$\dot{m}_{fuel} = 4.3898\ g/s$$

$$\dot{m}_{ox} = 32.3752\ g/s$$

With Equation 4.8, Table 4.13 and an exit area of $A_e = 392.675\ mm^2$, the expected sea level thrust was $F_{sl} = 60.04\ N$.

The simulation results and comparison to the expected results are given in Table 4.14. The thrust value was obtained by defining a report parameter in Fluent that summed up the axial forces on all walls and inlets. The output in Fluent was negative, as the x-direction was defined positive in the direction of the flow, whereas thrust acts in opposite direction. To circumvent having to define the inlets as walls, the thrust could alternatively be defined as the integral of static pressure across the inlet surfaces (positive value) minus the sum of axial forces on the walls (negative value), resulting in the same total value.

Table 4.14: Simulation results for qualitative validation

Parameter		Expected	Simulation	Deviation [%]
F	$[N]$	60.04	57.66	-3.96
T_c	$[K]$	2786.66	3076.20	10.39
p_e	$[bar]$	0.28	$0.26\ -\ 0.35$	$-7.14\ -\ 25.00$
p_c	$[bar]$	7.50	7.61	1.47
Ma_e	$[-]$	2.64	2.76	4.55
v_e	$[ms^{-1}]$	2417	2384	-1.37

There are several aspects that might explain the higher temperature compared to the CEA results. While CEA assumes chemical equlibrium, the combustion model in the simulation only considered the forward reaction and only full combustion, meaning no intermediate reaction products like carbon monoxide were created and dissociation was not considered. Furthermore, the walls in the simulation were assumed to be adiabatic, dismissing the heat lost to the walls. Lastly, the inlet temperatures varied: The material properties of H_2O_2 are only defined for the specific temperature of $272.74K$. The maximum deviation allowed is $10K$, so $282.74K$ was chosen as inlet temperature for CEA. Hence, the inlet enthalpy in the CEA analysis was lower compared to the simulation.

Trends

Contours of pressure, temperature etc. are not the same across all engines found in literature. However, the plots found generally agree between a few papers.

Combustion Zones

Comparing the temperature contour to the combustion zones described by Sutton [10] showed good agreement (Figure 4.28). Just behind the injector, there is a low temperature zone (light blue) where breakup, atomisation and mixing happens, closely followed by the rapid combustion zone with different colours, indicating that parts of the gas are already combusting and parts are still quite cold. From approximately the middle of the chamber to the throat, barely any change in temperature is noticeable, but streamlines can be seen clearly. Behind the throat, the flow expands, resulting in a decrease in temperature.

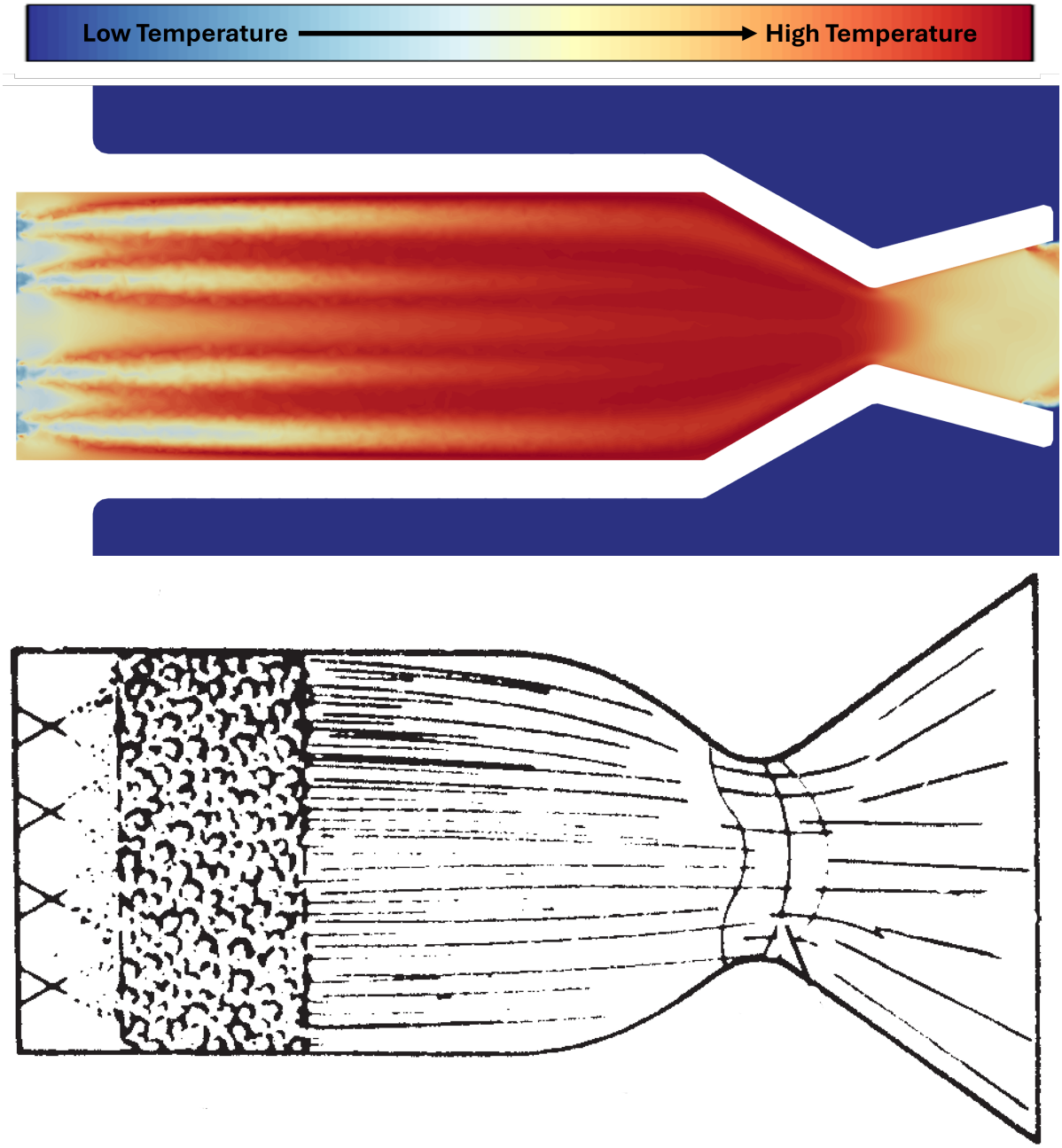

Figure 4.28: Temperature contour from thesis (top) compared to combustion zones in a generic rocket engine [10] (bottom)

Pressure

Figure 4.29 shows the pressure curve on the symmetry axis across the nozzle for simulations of different engines, normalised by the chamber length and the chamber pressure of each engine. In all cases, chamber pressure is approximately constant throughout the chamber and rapidly drops through the nozzle. The shift of curves to the left or right is due to the ratio of convergent to divergent section in the different nozzles.

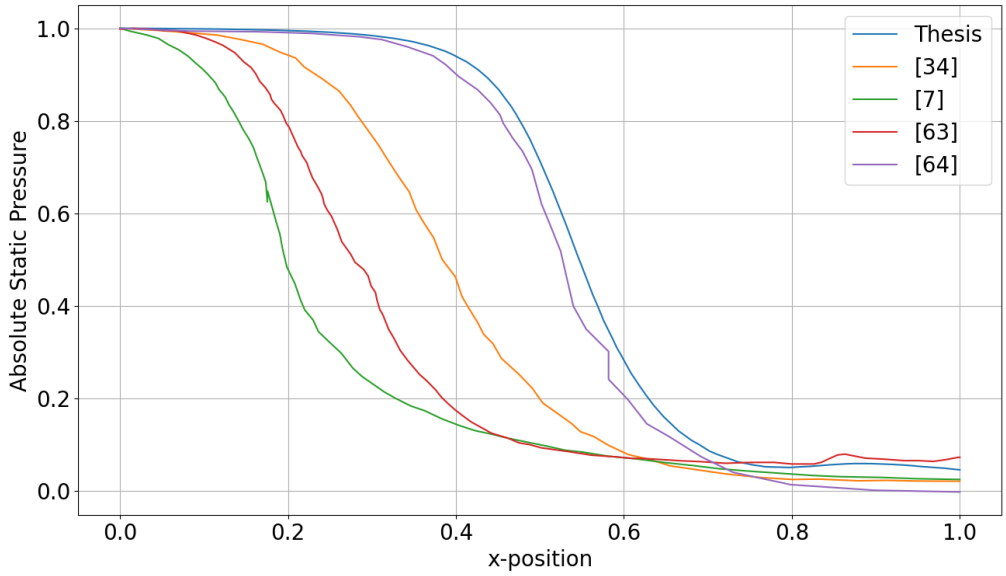

Figure 4.29: Absolute Static Pressure on central axis of the nozzle; thesis compared to different engines [7, 34, 63, 64]

Temperature

Figure 4.30 shows static temperature in the centre of the engine plotted over axial distance compared to a liquid-oxygen-kerosene engine [65] and a staged-configuration $100\ N$ HTP-kerosene engine [33]. Especially the contours of Greenlam and the other HTP-kerosene engine show strong agreement.

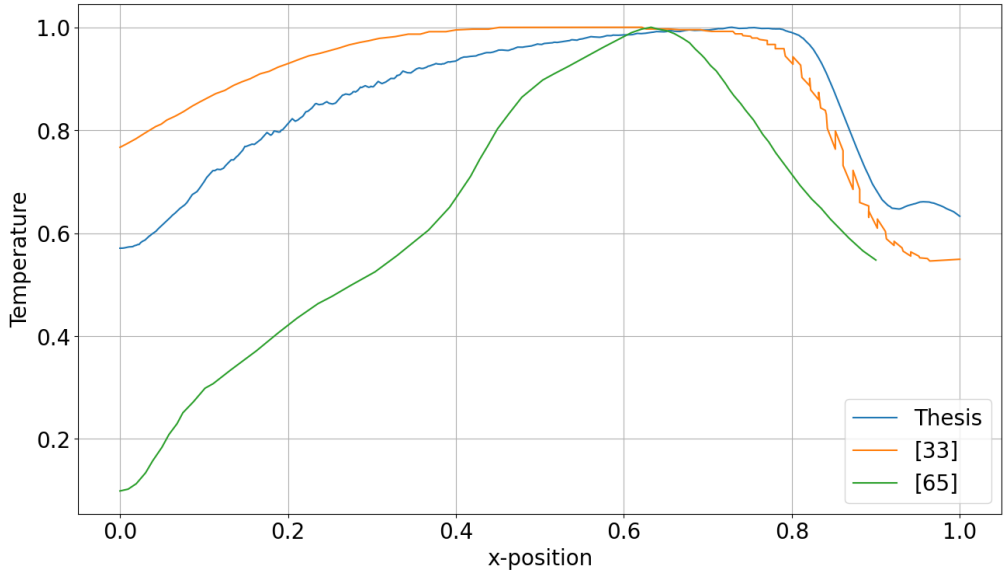

Figure 4.30: Temperature on central axis; thesis compared to different engines [33, 65]

Heat Transfer

Two different heat transfer coefficients are available in Fluent that can be calculated despite the adia-

batic thermal boundary condition, and while the nature of their curves is very similar, the values differ significantly. One coefficient is calculated based on y^+, one based on the wall function. Comparing the heat transfer to the wall to a generic qualitative plot given by [7] shows a similar trend with a slow increase after the injector, stronger increase in the convergent and peak at the throat ($x \approx 0.11\ m$), followed again by a quick decline (Figure 4.31). The heat transfer is predominantly governed by pressure and chamber diameter. The pressure at the throat and in the chamber is approximately identical, but the throat has a much smaller diameter, hence a higher heat flux. The exit diameter lies in between throat and chamber diameter, hence the intermediate heat flux. While not explicitly mentioned, the generic plot might assume a nozzle with an exit diameter larger than the chamber diameter (which is typical especially for upper stage nozzles), explaining the drop in the heat transfer coefficient towards the end below the value near the injector. Bartz developed a formula to determine the convective heat transfer coefficient in a rocket engine (Equation 4.9) [7, 66]. Taking simulation results as input for the formula, the heat transfer coefficient according to Bartz was calculated and compared to the two heat transfer coefficients taken from Fluent. The three coefficients calculated with Bartz, taken from the simulation based on y^+ and taken from the simulation based on the wall-function, were normalised with the same values to allow not only for qualitative but also quantitative comparison (Figure 4.31). Throughout the chamber, the y^+-based coefficient shows better agreement with Bartz' formula than the wall-function based coefficient. The y^+ based coefficient has a maximum deviation from the formula at the throat with a factor of 2. For the remaining simulations, the y^+-based coefficient was considered, the wall-function based one was disregarded.

$$h = \frac{0.026}{D_t^{0.2}} \frac{\mu^{0.2} c_p}{Pr^{0.6}} \left(\frac{p_c}{c^*}\right)^{0.8} \left(\frac{D_t}{r_c}\right)^{0.1} \left(\frac{D_t}{D_c}\right)^{1.8} \cdot \varphi \tag{4.9}$$

$$c^* = \frac{p_c A_t}{\dot{m}} \tag{4.10}$$

$$\varphi = \frac{\left[1 + Ma^2\,(\gamma - 1)\,/2\right]^{-0.12}}{\left[0.5 + 0.5\ (T_w/T_0)\,(1 + Ma^2\,(\gamma - 1)\,/2)\right]^{-0.68}} \tag{4.11}$$

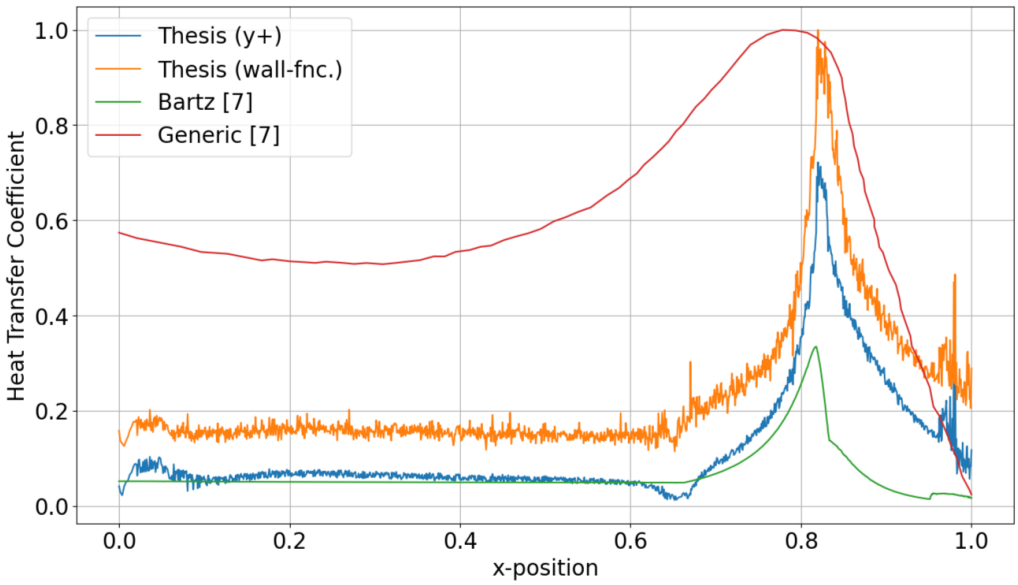

Figure 4.31: Wall Heat Transfer coefficient; thesis compared to generic and analytical results [7]

Velocity

With the assumption of an ideal gas and isentropic flow, the axial velocity v can be described as a function of temperature T with the specific gas constant R and the ratio of specific heats γ and the chamber temperature, i.e., the maximum temperature, T_c (Equation 4.12) [7].

$$v(T) = \sqrt{\frac{2\gamma}{\gamma - 1} \cdot \frac{R\,T_c}{M} \cdot \left(1 - \frac{T}{T_c}\right)} \tag{4.12}$$

γ is not directly available from the simulation data, but can be derived from c_p, R and M(Equation 4.13). c_p, R/M and T can be read from the simulation data.

$$\gamma = \frac{c_p}{c_v} = \frac{c_p}{c_p - R/M} \tag{4.13}$$

In general, velocity profiles across the nozzles of rocket engines show a similar but inverted trend compared to the static pressure, as reactions become less important and the high pressure and low velocity before the nozzle is converted to low pressure and velocity after the nozzle. Both the analytical estimate and external numerical results agree with the curve obtained (Figure 4.32).

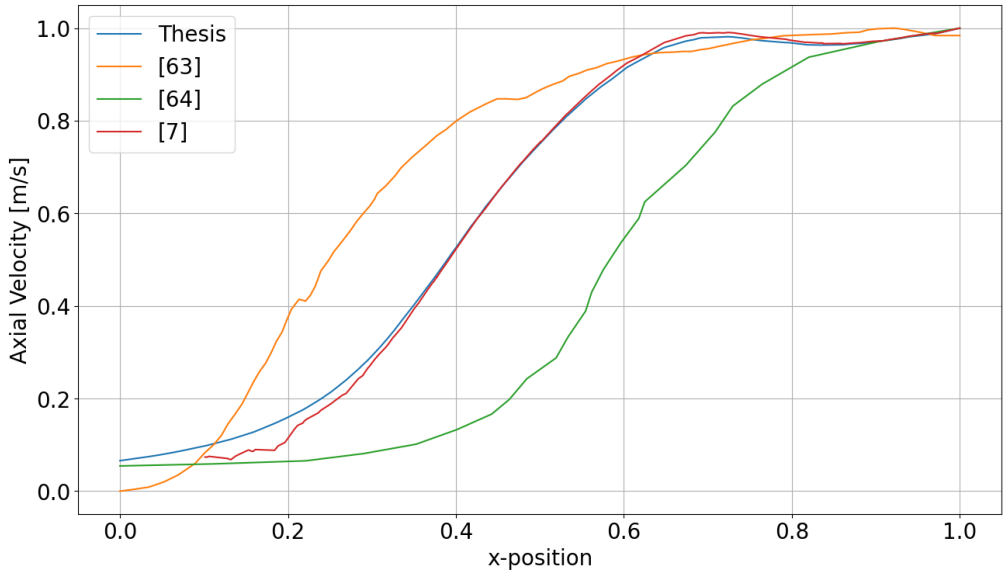

Figure 4.32: Velocity contours on the central axis of the nozzle; thesis compared to different engines [63, 64] and analytical result [7]

4.5. Summary of Modelling & Validation

The chamber geometry and its material, excluding the injector, were given by the research group. Three different injectors, a coaxial, an impinging jet and a pintle injector, were considered for the simulations and implemented in CAD.

In the final setup, simulations were performed three-dimensional and transient. Turbulence was modelled using k-ω SST to be able to accurately model both free-stream and near-wall flows and to as-

sume y^+-insensitivity. Decomposition and combustion reactions were implemented with the Finite Rate Species Transport model, since a reaction mechanism with a limited number of species was chosen and the effect of a catalyst could be considered by setting corresponding Arrhenius rate parameters. In terms of time scale of the reaction, the reaction rates were assumed to be more important than the turbulent mixing. Reactions were assumed to occur exclusively in the gas phase. Propellants were injected as separate Discrete Phase droplets with TAB breakup enabled, gases were modelled as continuum with the Peng-Robinson equation of state. The Discrete Phase Model was chosen because it is generally better suited to model the interaction between liquid droplets and the surrounding gas. Furthermore, the Eulerian model could not represent evaporation which was considered critical to initiate combustion in a hypergolic engine.

Using insights from preliminary simulations and the software CEA, it was found that a pressure of about $7.5bar$ is required for the given chamber to produce a thrust of $F = 100N$. Different concentrations and equivalence ratios were considered. Fuel-rich mixtures showed higher specific impulse and higher chamber temperature. Since the chamber temperatures were only slightly higher than the allowable wall temperature and a decrease of the chamber temperature towards the wall was expected, colder, oxidiser-rich mixtures were not considered in the following due to their inferior performance.

Validation was initially attempted by replicating experimental work from KAIST and Purdue University with the defined simulation setup. Neither work could be replicated, presumably due to the droplet collision model not being compatible with the rather coarse temporal and spatial resolution that had to be chosen due to availability of resources or due to incomplete information given in the papers or an incompatibility of the droplet collision model. Generally, little research has been published on non-staged HTP bipropellant engines and no other papers suitable for replication could be found. Hence, a rather qualitative validation approach was followed, comparing the temperature, velocity, pressure and heat transfer curves obtained from the simulation to curves or analytical results published for other engines. Furthermore, single values like chamber temperature, thrust, exit pressure etc. were compared to the values expected after conducting analysis with CEA. Comparison with both data from other papers and with CEA showed good agreement. The reaction mechanism and especially the reaction rate parameters remain to be validated by experiment.

To achieve mesh independence, the original mesh with 1.26 million nodes was refined several times. The finest mesh had 8.37 million nodes. Differences in maximum values for several parameters between the finest and second finest mesh were less than 1%. The transient behaviour was still different between the two meshes, i.e., the finest mesh required more time-steps to achieve steady-state. However, since the curves were only shifted but the steady-state values were approximately identical and the quantitative transient behaviour could not be verified due to a lack of Arrhenius parameters anyways, the mesh was considered sufficient.

5

Results & Discussion

This chapter shows the results obtained in the simulations, analysing the parameters which describe the engine performance, the flow characteristics and the loads on the chamber structure, as outlined in Section 3.2.3.

As described in Section 4.2.6, four different propellant combinations were tried. The highest concentration usually considered for HTP is 98%, resulting in the highest performance. A slightly lower concentration of 95% was considered as well to lower the loads on the thrust chamber. As it was found that the highest performing mixture is not the stoichiometric ratio but a slightly fuel-rich composition (Figure 4.6), both the stoichiometric and the highest performing O/F were simulated for both concentrations (Table 5.1):

Table 5.1: Overview of the simulations performed

α	Φ	O/F	$I_{sp,vac}[s]$	$\dot{m}$ $[10^{-3}$ $kg]$	**Identifier**
98%	1.00	7.39	277.4	36.75	c98st
98%	1.15	6.42	279.4	36.50	c98hp
95%	1.00	7.62	274.7	37.12	c95st
95%	1.10	6.93	276.3	36.89	c95hp

To analyse the transient change in temperature, pressure and velocity, snap shots of the corresponding contours were taken at each time step and are shown for the *c98st* case. All the analysis presented here is only valid for the selected Arrhenius parameters. Hence, with a different catalyst, the transient behaviour would likely look similar in magnitude and trend but be shifted in time.

5.1. Engine Performance

As the I_{sp} (obtained with CEA) varied between the mixtures but the thrust requirement of $F = 100N$ held regardless, the mass flow was varied between the mixtures to realise the same thrust for all four setups. As expected, the steady-state thrust was approximately identical, but small differences were still present (Table 5.2): Among the stoichiometric setups, the higher concentration produced higher thrust, and both resulted in higher thrust than the fuel-rich setups. As explained in Section 4.4.3, a

Table 5.2: Thrust for different propellants and deviation from the default case ($\alpha = 98\%$, $\Phi = 1.00$)

Case	Thrust [N]	Thrust rel.
$\alpha = 98\%$, $\Phi = 1.00$	63.22	$-$
$\alpha = 98\%$, $\Phi = 1.15$	61.88	-2.11%
$\alpha = 95\%$, $\Phi = 1.00$	63.00	-0.34%
$\alpha = 95\%$, $\Phi = 1.10$	62.09	-1.78%

vacuum thrust of $100.00N$ is equivalent to a sea-level thrust of $60.04N$ (obtained with Equation 4.8), mostly due to the overexpansion caused by atmospheric pressure. All values exceeded the analytical estimate. Reasons for this might have been the slightly higher chamber pressure, leading to higher I_{sp} (Figure 4.6), and the different reaction models.

In terms of transient behaviour, no significant difference could be identified. After rising initially, the thrust decreased between about $5ms$ and $8ms$ before rising again (Figure 5.1). Analysis of the velocity contours showed that after about $5ms$, the flow began to separate from the nozzle wall, which was likely the cause for the drop in thrust. Steady state, measured by constant thrust, was reached after approximately $50ms$.

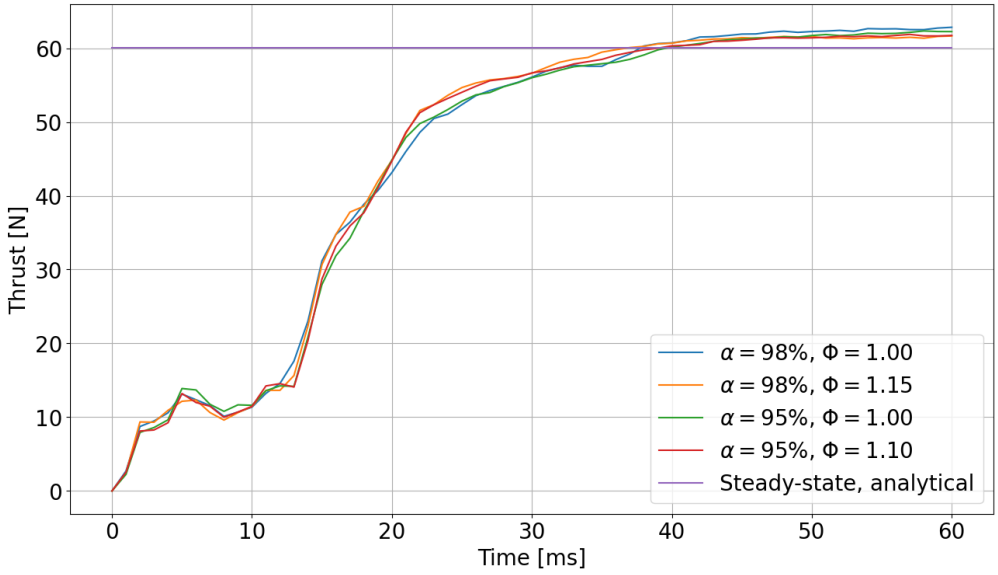

Figure 5.1: Thrust over time for different propellants compared to the analytical value obtained based on CEA data

Figure 5.2 shows the mass flow rates for the different cases that are needed to fulfil the thrust requirement of $F_{vac} = 100N$. As described before, the theoretical specific impulse as per CEA (*orange*) increases with increasing concentration and increasing equivalence ratio (up to the optimum equivalence ratio). Based on the thrust values obtained in the simulations, the actual sea-level specific impulse was calculated for all cases. Assuming that the ratio of vacuum thrust to sea-level thrust stays constant ($\frac{F_{vac}}{F_{sl}} = \frac{100N}{60.04N}$), the mass flow rates to obtain $100N$ thrust in vacuum were calculated (*blue*). While higher concentrations still resulted in higher I_{sp} and thus lower mass flow rate, the fuel-rich mixtures now performed worse. If only mass optimisation were considered, disregarding the resulting loads, the highest performing mixture would be chosen: According to CEA, this would be the highest concentra-

tion with the highest equivalence ratio ($\alpha = 98\%$ and $\Phi = 1.15$). According to the simulations, this would be the highest concentration but the stoichiometric equivalence ratio ($\alpha = 98\%$ and $\Phi = 1.00$). The difference between highest and lowest mass flow rate in either case is approximately 2%, the significance of which would need to be evaluated in combination with considerations resulting from the thermo-mechanical analysis of the chamber structure and their implications for sizing and thus chamber mass.

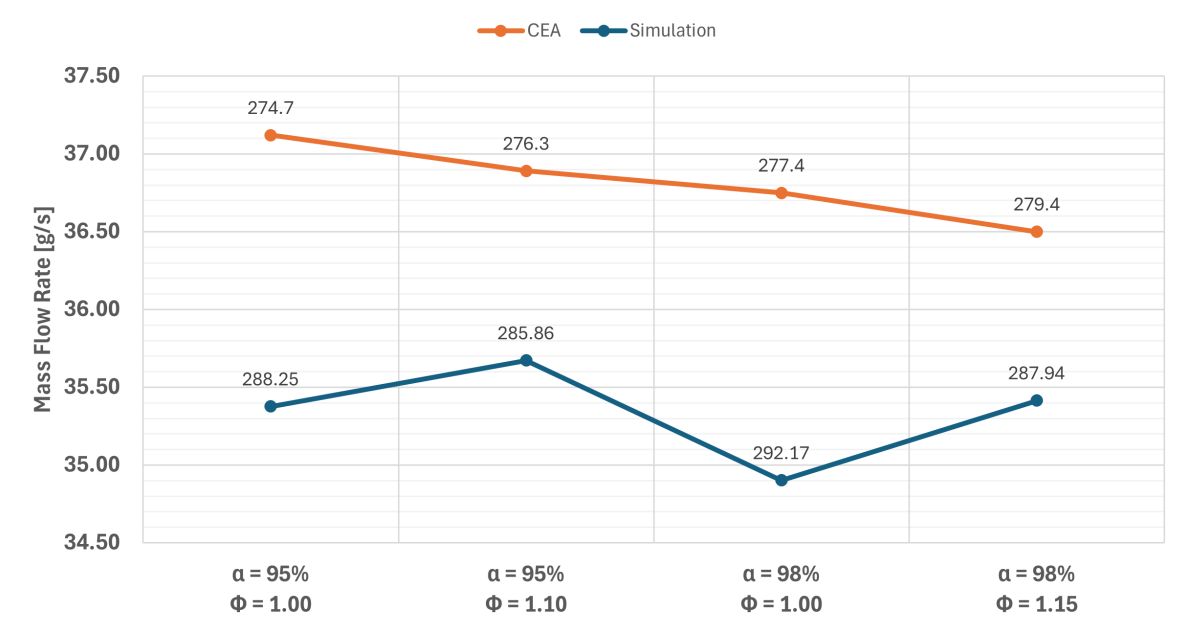

Figure 5.2: Mass Flow Rate to obtain a Vacuum Thrust of $F = 100N$ for Varying Propellants, according to CEA and derived from simulations; I_{sp} $[s]$ is given for each fuel combination

5.2. Flow Characteristics

Temperature, pressure and velocity were analysed to understand the overall behaviour of the engine and the processes behind it, rather than to infer implications for the chamber structure. Both the development over time and the differences caused by selecting different propellants were considered.

5.2.1. Static Temperature

Transient Temperature

Reactions occured within the first time-step ($t = 1ms$), visible in the contour (Figure 5.3) as four zones of higher temperature, showing the four oxidiser injections lying in the cross section. Analysing the reaction rates showed that directly after the injector, the thermal decomposition reaction remained the dominant reaction throughout all time-steps, being approximately three orders of magnitude more frequent than the combustion reactions, as evaluated by plotting reaction rates [$kgmol/m^3s$]. While the thermal decomposition has a much higher activation energy, it can already be initiated in the pure oxidiser stream without the presence of fuel being required.

The high temperature and thus the decomposition zones expanded over the next time steps, with ignition occuring at around $7ms$. Following ignition, the high temperature zones spread towards the nozzle and towards the injector. The temperature near the wall increased faster than in the centre of the engine. At $t = 40ms$, the flow inside the chamber was almost fully developed. Close to the injector,

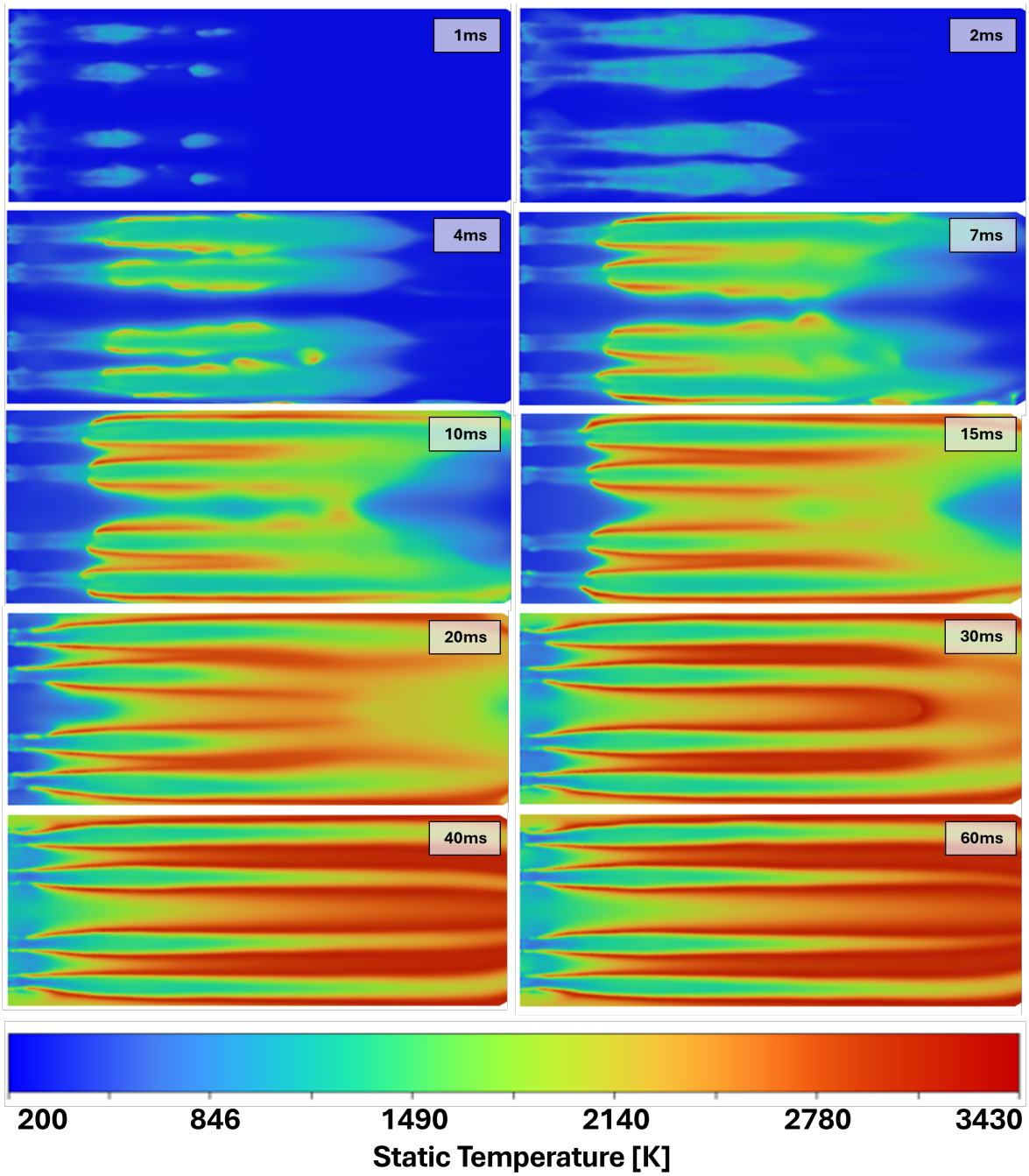

Figure 5.3: Static Chamber Temperature over Time (Injector to Nozzle Entrance)

the temperature remained comparatively low ($T \approx 1250K$). At $t = 60ms$, a slight reduction in width of the two inner oxidiser streams was visible, indicating more combustion. The four coaxial injection elements that lay in the cross-sectional plane could be seen clearly. Following the injectors to the right, relatively cold streams of rather pure oxidiser (green) were visible. On the border between annuli and orifices, i.e., where the propellants mixed, red lines began to form, indicating combustion and hence a higher temperature. Towards the convergent section, the low temperature zones reduced, indicating progressing combustion, however not complete combustion. Between $t = 40ms$ and $t = 60ms$, barely any change in temperature was visible in the chamber.

The temperature in the nozzle first significantly rose at around $t = 10ms$ (Figure 5.4) and increased at the wall before it did in the centre. As the flow developed further and exited the chamber ($t = 20ms$), separation could be seen in the nozzle divergent, and subsequently shock diamonds formed ($t = 30ms$). This was expected, as the injection was setup in a way that operating the engine in vacuum would lead

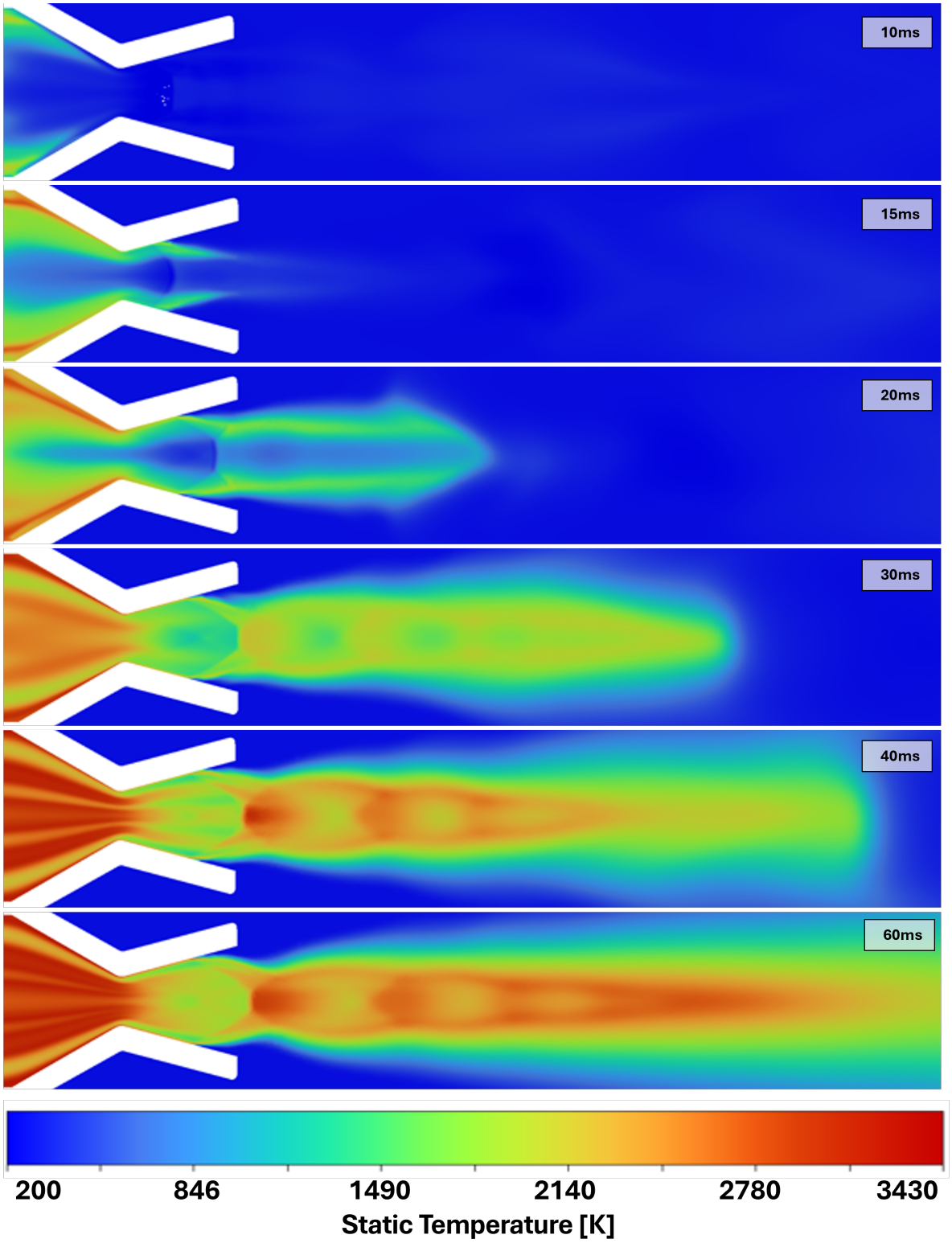

Figure 5.4: Static Nozzle and Plume Temperature over Time

to optimal expansion. Since at sea-level the atmospheric pressure is much higher, the flow was pushed inwards, i.e., away from the nozzle wall (over-expansion). This led to a subsequent compression of the flow and hence an increase in temperature and pressure, and the flow expanded again. This pattern of shock (compression) and expansion repeated several times. While the chamber temperature remained stable after $40ms$, the plume continued to develop until $t = 60ms$.

Figure 5.5 shows the temperature at different locations throughout the engine. Following the streamlines from the oxidiser injectors, it can be seen that low-temperature zones remained behind the oxidiser injector throughout the engine and high temperature zones appeared at the interface between oxidiser and fuel. This is most clear at $x = 0.02m$, showing the cold oxidiser in green and combustion in red. The green colour is equivalent to a temperature of approximately $1350K$ - the temperature obtained from decomposition of 98%-HTP according to CEA is $1394K$. Since 12 of the 18 injectors were placed close to the wall, this led to high reaction rates and consequential generation of heat near the walls.

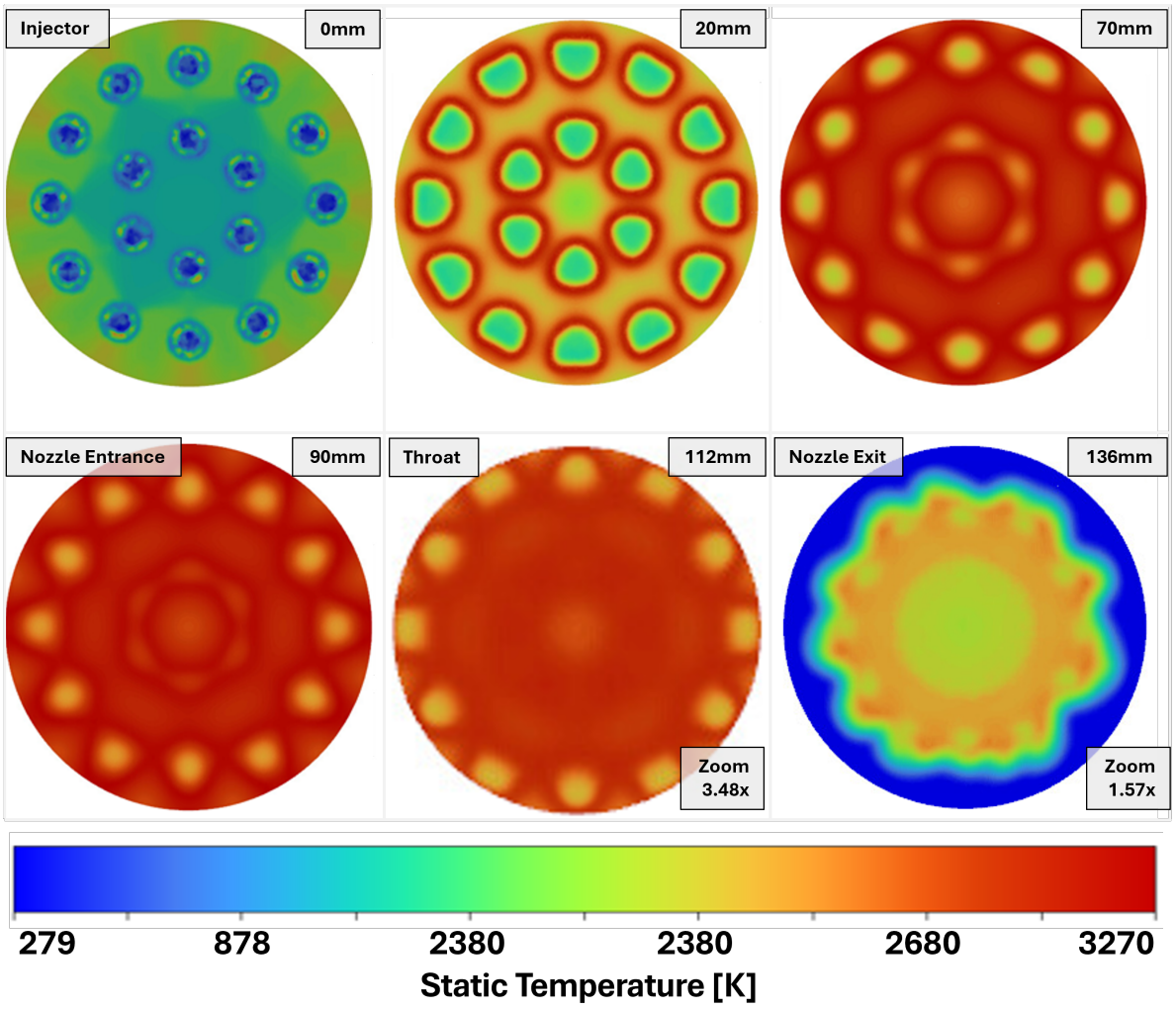

Figure 5.5: Change in temperature throughout the chamber (steady-state, $\alpha = 98\%$, $\Phi = 1.00$); throat and nozzle exit are enlarged

Temperature for different Propellants

Figure 5.6 shows the temperature on the chamber central axis plotted over axial distance for the four different propellant combinations. As also visible in the contours (Figure 5.3), the temperature is rel-

atively low near the injectors where no combustion is happening. With increasing axial distance, the combustion progressed and temperature rose. The highest temperature was reached just before the throat ($x = 0.11m$). After the throat, the pressure and hence the temperature dropped quickly. The sudden increase and subsequent decrease in temperature at $x \approx 0.13m$ were caused by the separation and formation of shock diamonds, clearly visible in Figure 5.4 at $t = 60ms$. The unevenness of the temperature curves was likely caused by the combination of mesh resolution and a high temperature gradient: the values were taken from the symmetry axis, but the unstructured mesh did not necessarily align with it. Hence, to produce a value for this specific location, neighbouring cell values were interpolated.

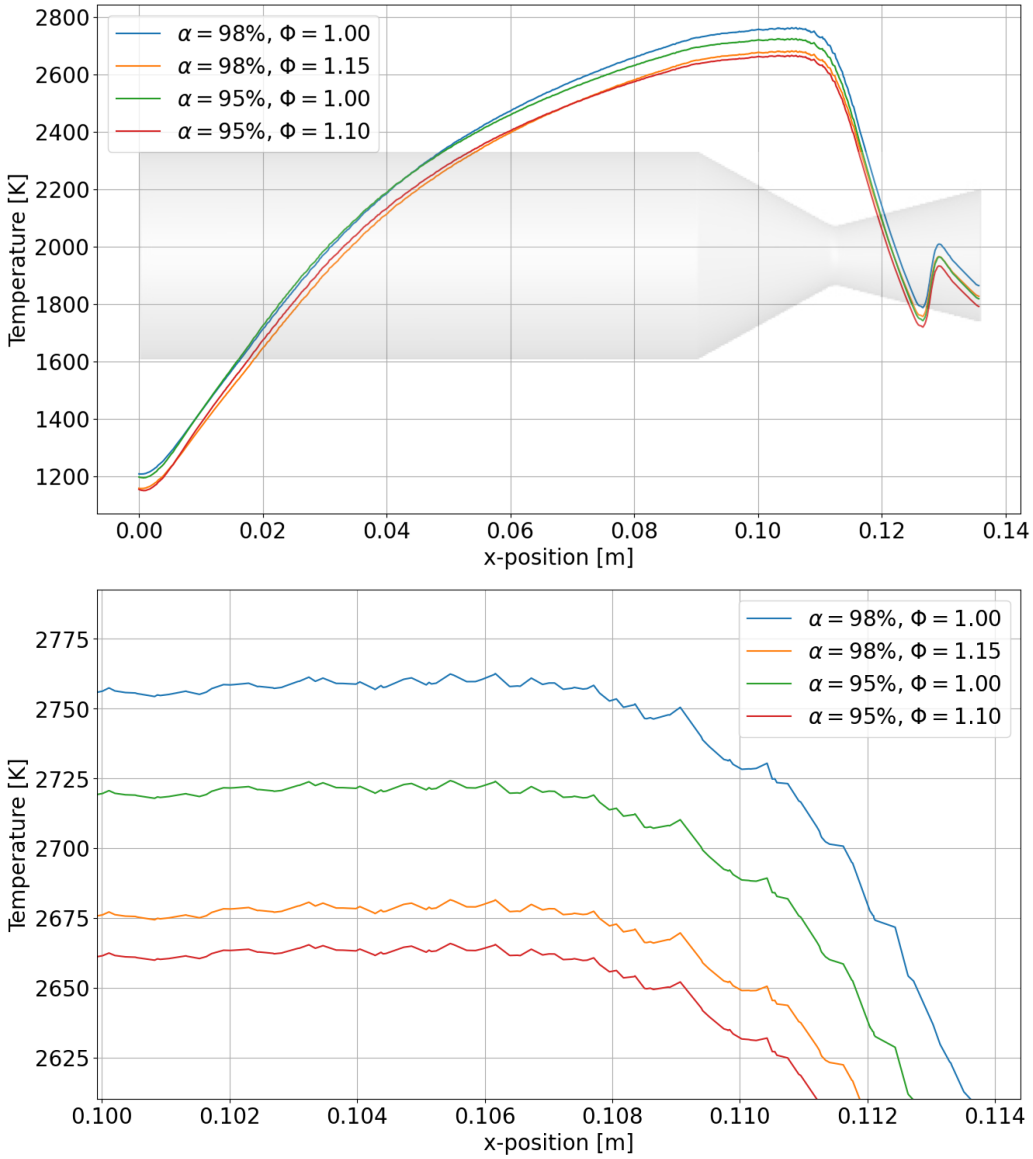

Figure 5.6: Static Temperature along the chamber symmetry axis for different propellants; whole chamber (top) and throat (bottom)

The radial position of these cells may have varied slightly. Since there was a high radial temperature gradient in the throat (see Figure 5.4), this could have caused the unsteadiness of the graph.

The values for the stoichiometric propellants deviated less than 1% from the values predicted with CEA. For the higher performing fuel-rich mixtures, the deviations were within 5% (Table 5.3).

Table 5.3: Temperature prediction from CEA compared to Maximum Static Temperature on the symmetry axis from simulations for different cases

	CEA	**Simulation**
$\alpha = 98\%$, $\Phi = 1.00$	$2787K$	$2763K$
$\alpha = 98\%$, $\Phi = 1.15$	$2806K$	$2682K$
$\alpha = 95\%$, $\Phi = 1.00$	$2740K$	$2724K$
$\alpha = 95\%$, $\Phi = 1.10$	$2758K$	$2666K$

As expected, the higher concentration mixtures reached higher combustion temperatures than the lower concentrations. Contrary to the predictions made with CEA, the fuel-rich mixtures led to a lower combustion temperature compared to the stoichiometric mixtures of the same concentration. A possible cause for this may have been the degree to which the kerosene was combusted (see section 5.3).

5.2.2. Absolute Pressure

Transient Pressure

Pressure was approximately constant throughout the chamber and dropped quickly across the throat for all time steps (Figure 5.7). Pressure rose quickly and with continuing increase in pressure, shock diamonds started to form around $t = 10ms$ and became visible more clearly at $t = 20ms$. This pattern expanded in axial direction. At $t = 30ms$ chamber pressure reached more than 90% of the steady state pressure. From $t = 40ms$ onwards, the chamber pressured was approximately constant and only the plume showed slight development.

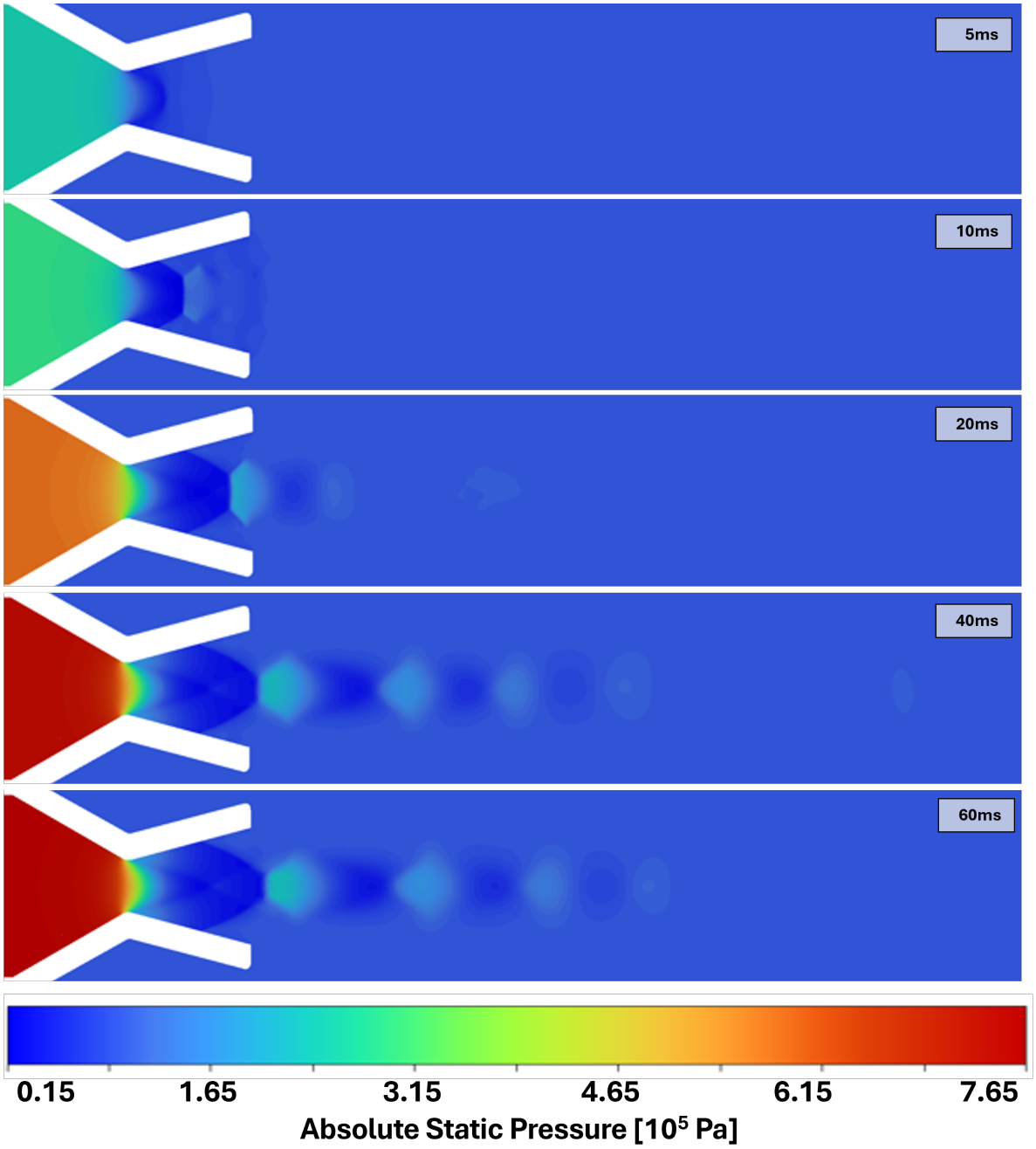

Figure 5.7: Absolute Static Pressure Contour over Time (Nozzle)

Pressure for different Propellants

The pressure was expected to be the same across all four cases, since the CEA chamber pressure value was set to $7.50\ bar$ for all cases. The peak pressure ranged from $7.54\ bar$ ($\alpha = 98\%$, $\Phi = 1.15$) to $7.66\ bar$ ($\alpha = 98\%$, $\Phi = 1.00$), a difference of 1.24% and a maximum deviation from the set pressure of 2.18% (Figure 5.8). The difference could be attributed to the difference in combustion completeness, as explained in section 5.3. Across the throat ($x = 0.11m$), the pressure dropped. Subsequently, there was a small increase in pressure due to the Mach diamond pattern, as explained above.

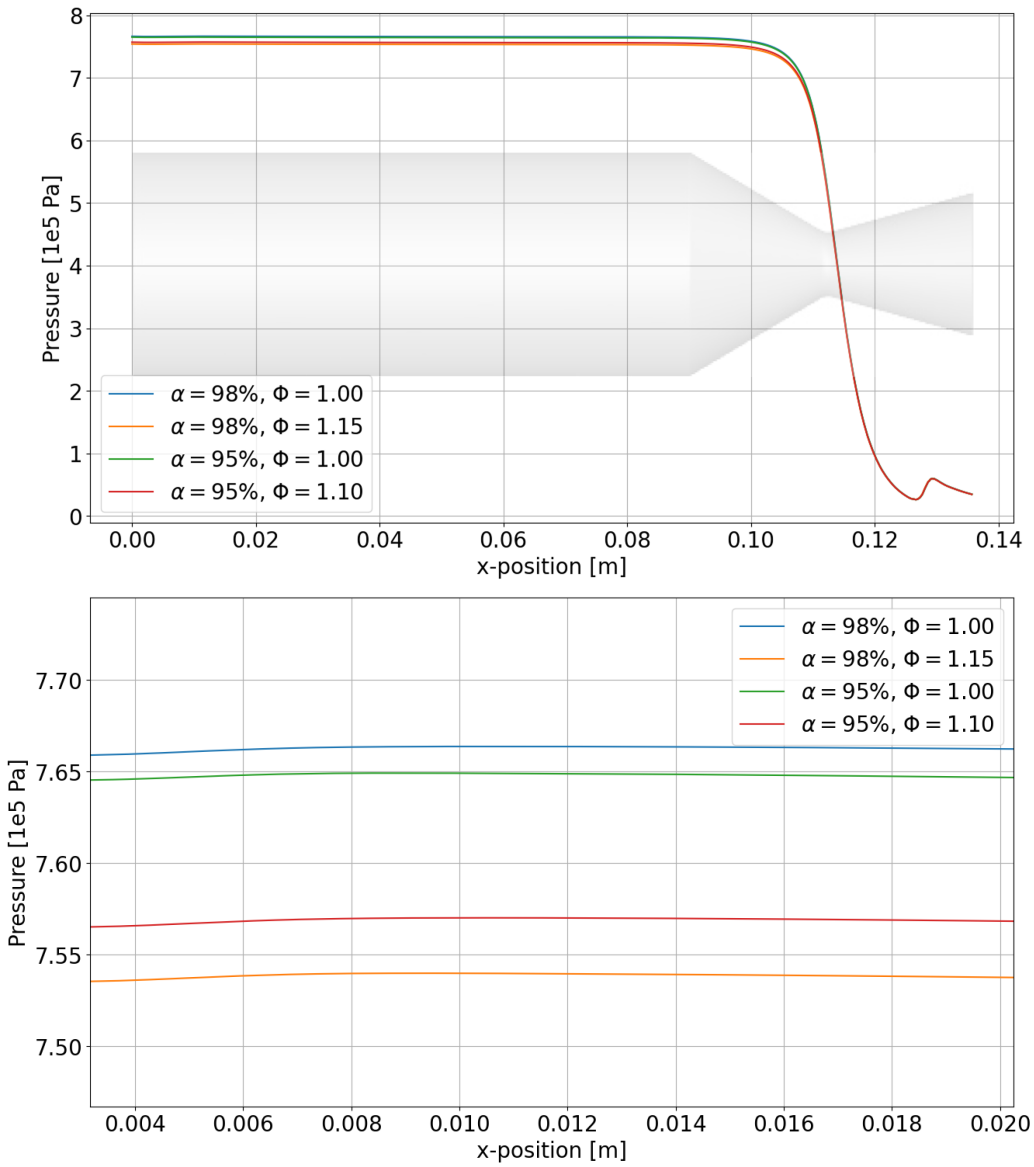

Figure 5.8: Absolute Static Pressure along the chamber symmetry axis for different propellants; whole chamber (top) and near injector (bottom)

5.2.3. Velocity Magnitude

Transient Velocity

At $t = 2ms$, a high-velocity region developed around the throat and continued to move in axial direction (Figure 5.9). At $t = 10ms$, a first oblique shock and subsequent flow separation were visible. At around $t = 22ms$, further shocks and expansion fans could be seen. From $t = 30ms$ to $t = 60ms$, the contour remained qualitatively unchanged, merely expanding in axial direction. Similar to the temperature contours, reactions could clearly be located at the first time step ($t = 1ms$), leading to a rapid increase in pressure and thus acceleration. The chamber velocity continued to match the temperature contour, as shown in Figure 5.10, until $t = 7ms$. For later time-steps, the velocity in the chamber was small compared to the velocity in the nozzle divergent.

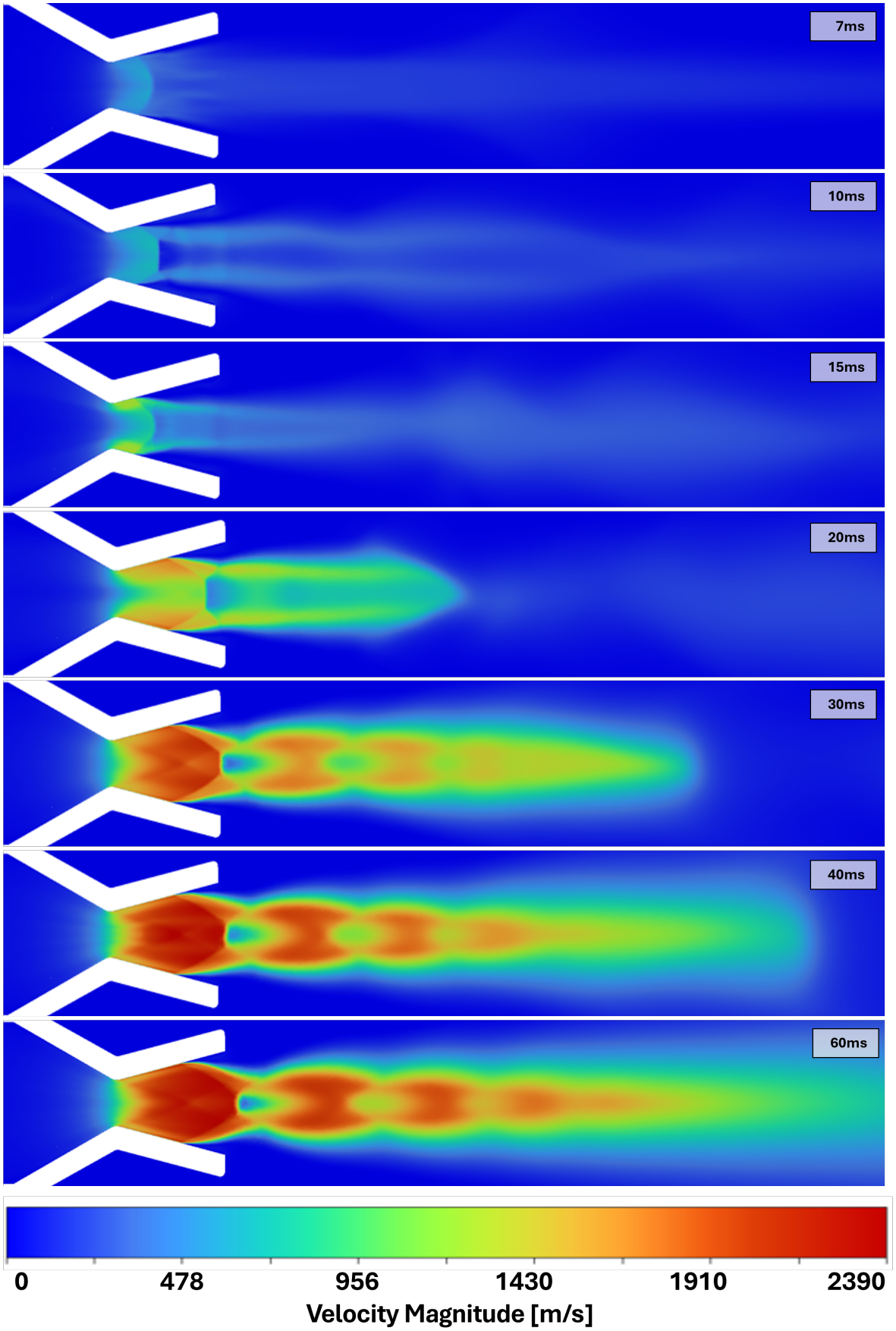

Figure 5.9: Nozzle Velocity Magnitude Contour over Time

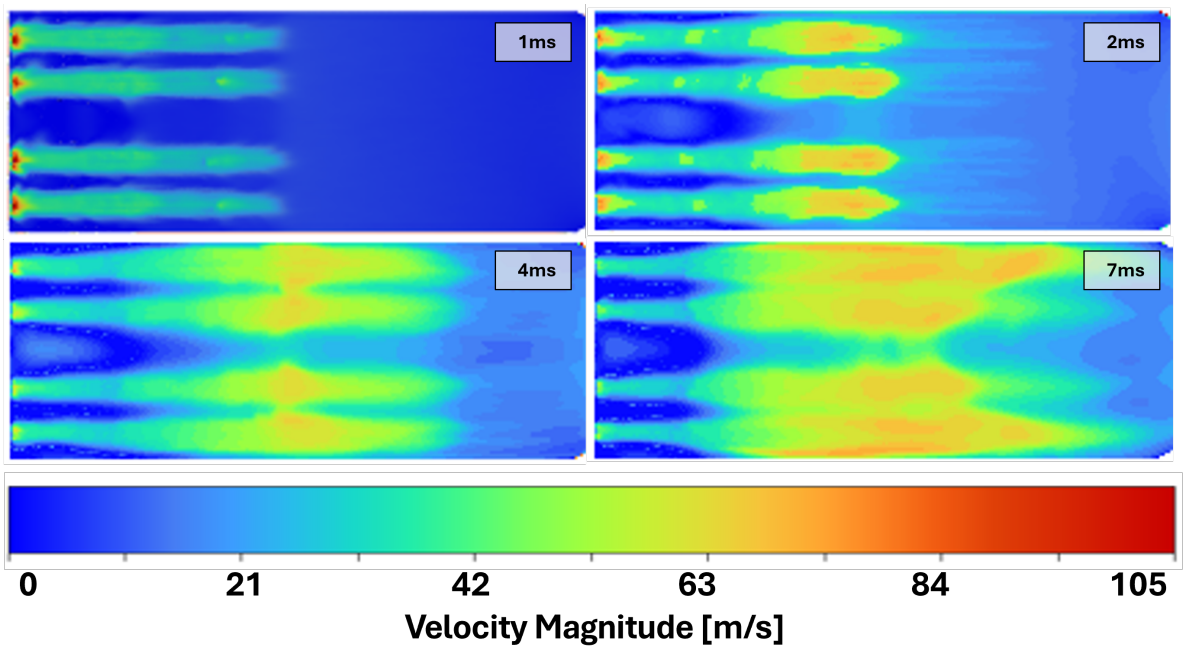

Figure 5.10: Chamber Velocity Magnitude Contour over Time

Velocity for different Propellants

Up to the throat, there appeared to be no difference between the velocity plots (Figure 5.11). Velocity rose across the throat ($x = 0.11m$), as expected for subsonic flow in a convergent and supersonic flow in a divergent nozzle. The highest velocity was reached in the divergent part of the nozzle, where the flow continued to accelerate until separation occurred ($x \approx 0.1265m$). The shock accompanying the separation led to a rapid increase in pressure and thus decrease in velocity. In the nozzle divergent, peak velocities varied from $2212\ m/s$ (*c98hp*) to $2261\ m/s$ (*c98st*), a deviation of 2.22%. As seen in the pressure curves, the stoichiometric mixtures led to a higher velocity.

5.3. Exhaust Composition

Since there were unexpected differences in thrust (section 5.1) and in temperature (Section 5.2.1), the exhaust species composition was analysed to find the cause for the deviations.

Looking at the exhaust composition, specifically, the mass fraction (or concentration) of kerosene at the throat and the nozzle exit (Table 5.4), showed that the fuel rich cases emitted more unburnt fuel than the stoichiometric cases. While a fuel-rich injection by definition must lead to incomplete combustion and thus was to be expected, the relative increase in kerosene mass fraction in the nozzle for these cases exceeded the relative increase in kerosene mass fraction at the injector, measured by equivalence ratio Φ. Almost all additional injected kerosene appeared to be ejected unburnt, leading to the lower temperatures. From Figure 5.12 it can be seen that the kerosene concentration was not uniform throughout the plane of the throat or the nozzle exit. The peak concentrations coincided with the injection pattern: Especially looking at the kerosene concentration for $\alpha = 98\%$, $\Phi = 1.15$ at the throat (Figure 5.12), the 18 oxidiser injections could be seen in blue, leading to kerosene concentrations in between the injector elements and in the centre of the chamber, since kerosene was injected from the annuli surrounding the oxidiser orifices (see Figure 4.2). The highest local concentration of kerosene in the nozzle exit plane was 5.67% and 5.02% for the 98% and 95% stoichiometric mixtures, respectively.

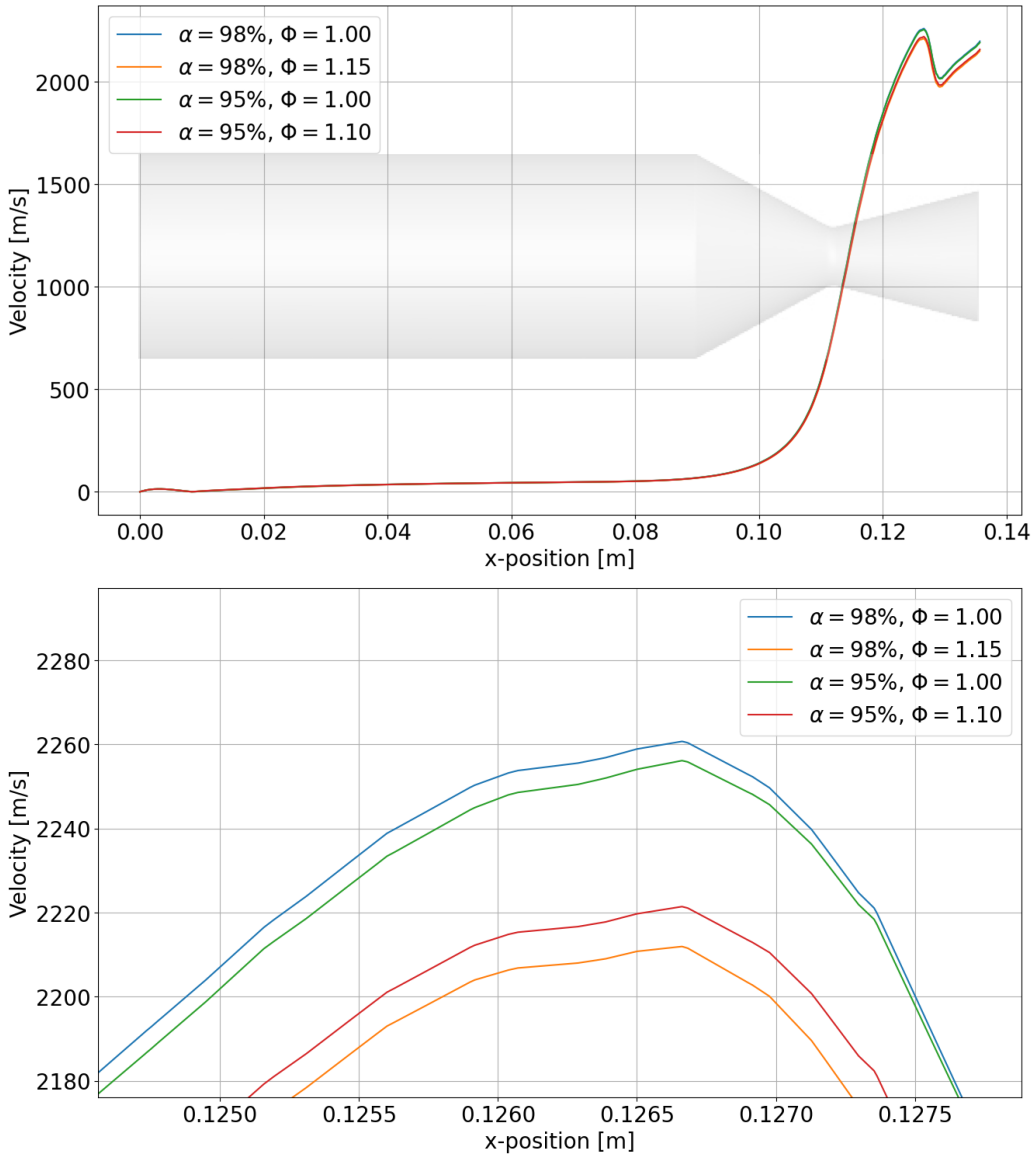

Figure 5.11: Velocity Magnitude along the chamber symmetry axis for different propellants; whole chamber (top) and at separation point (bottom)

Table 5.4: Peak kerosene concentration for different cases; relative values are given for fuel-rich cases with respect to the corresponding stoichiometric case

	$c_{C_{12}H_{23}}$ (Throat)	$c_{C_{12}H_{23}}$ (Exit)
$\alpha = 98\%$, $\Phi = 1.00$	6.47	5.67
$\alpha = 98\%$, $\Phi = 1.15$	7.84 (+21.20%)	7.10 (+25.29%)
$\alpha = 95\%$, $\Phi = 1.00$	5.77	5.02
$\alpha = 95\%$, $\Phi = 1.10$	6.68 (+15.66%)	6.01(+19.65%)

For the fuel-rich mixtures with 98% and 95%, the injected kerosene mass fractions were 15% and 10% higher, but the peak concentration at the exit was 25% and 20% higher, respectively. Figure 5.13 shows the mass fractions for kerosene and oxygen throughout the chamber. It can be seen that in the nozzle, the highest oxygen concentration remained close to the wall, whereas a high concentration of kerosene remained in the centre. So despite oxidiser being available in the chamber, incomplete combustion

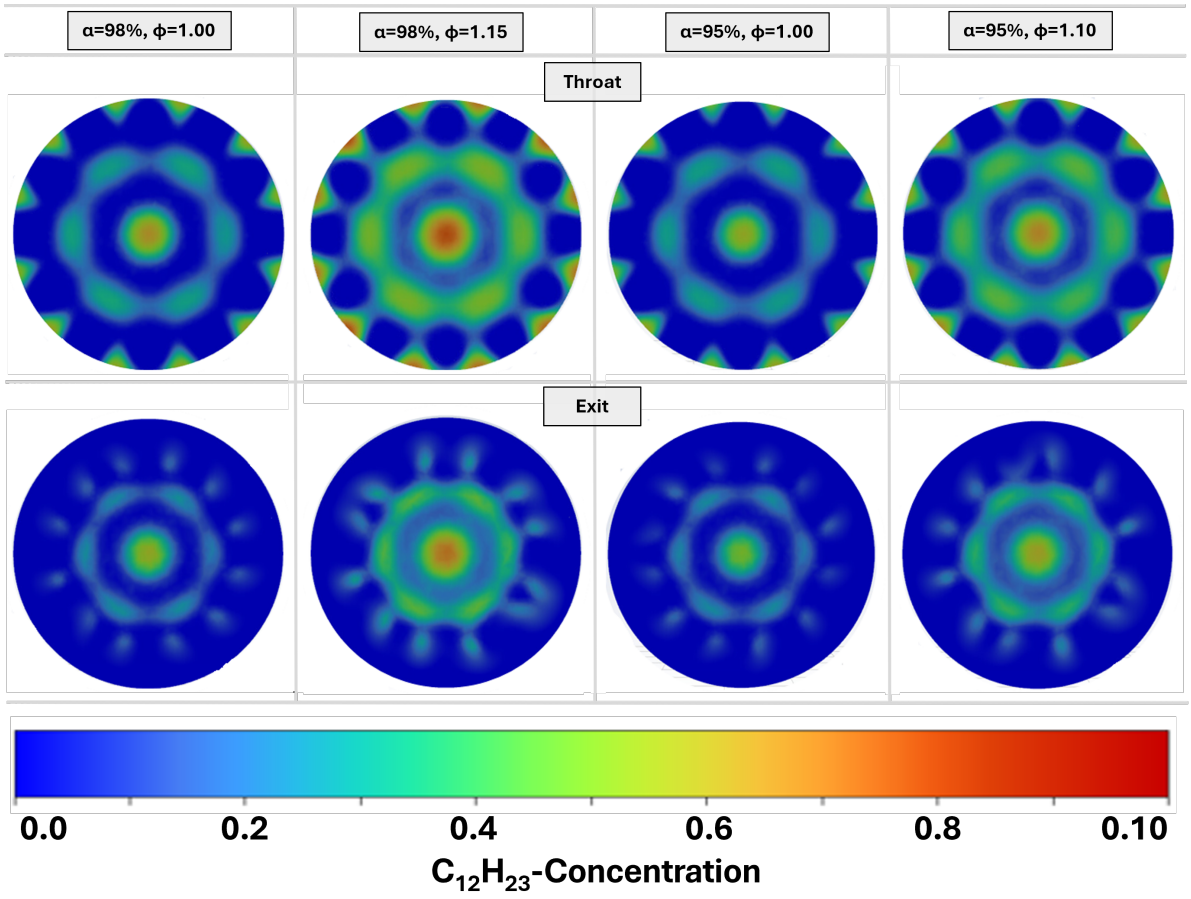

Figure 5.12: Kerosene mass concentration at throat (top) and nozzle exit (bottom) for different propellants

appeared to be caused due to insufficient mixing and hence a local lack of oxidiser. As explained in Section 4.2.6, increasing the equivalence ratio to a slightly fuel-rich mixture was expected to result in higher performance than a stoichiometric mixture. However, a further increase in equivalence ratio would lead again to a decrease (Figure 4.6). It appears that due to the insufficient mixing, the local equivalence ratios in the chamber were either beyond the optimal fuel-rich ratio or even below the stoichiometric ratio, thus overall resulting in inferior performance. This was assumed to be the cause for the lower thrust (Table 5.2) and temperature (Table 5.3) for the fuel-rich cases.

The uneven distribution of oxidiser and fuel also explains the uneven radial temperature distribution in all cases, since local peaks in oxidiser mass fraction lead to the lowest temperature and the mixing of both propellants to combustion, i.e., the highest temperature. Furthermore, the high kerosene concentration in the centre may have led to the delayed increase in temperature at the centre of the chamber (Figure 5.3, $10ms$ & $15ms$) as no decomposition and less combustion could happen there.

Table 5.5 displays the mass fractions of all species found at the nozzle exit ($x = 0.1357m$). Values displayed are not the peak concentrations but the average concentration over the whole exit area. The average composition was obtained by using a mass-weighted integral at the nozzle exit. H_2O_2 is listed for completeness, but was fully decomposed before leaving the engine in all cases. Flow separation occurred before the nozzle exit and led to atmospheric gases flowing into the nozzle. Since the atmosphere was considered to consist of 21% oxygen and 79% nitrogen, nitrogen is also part of the composition.

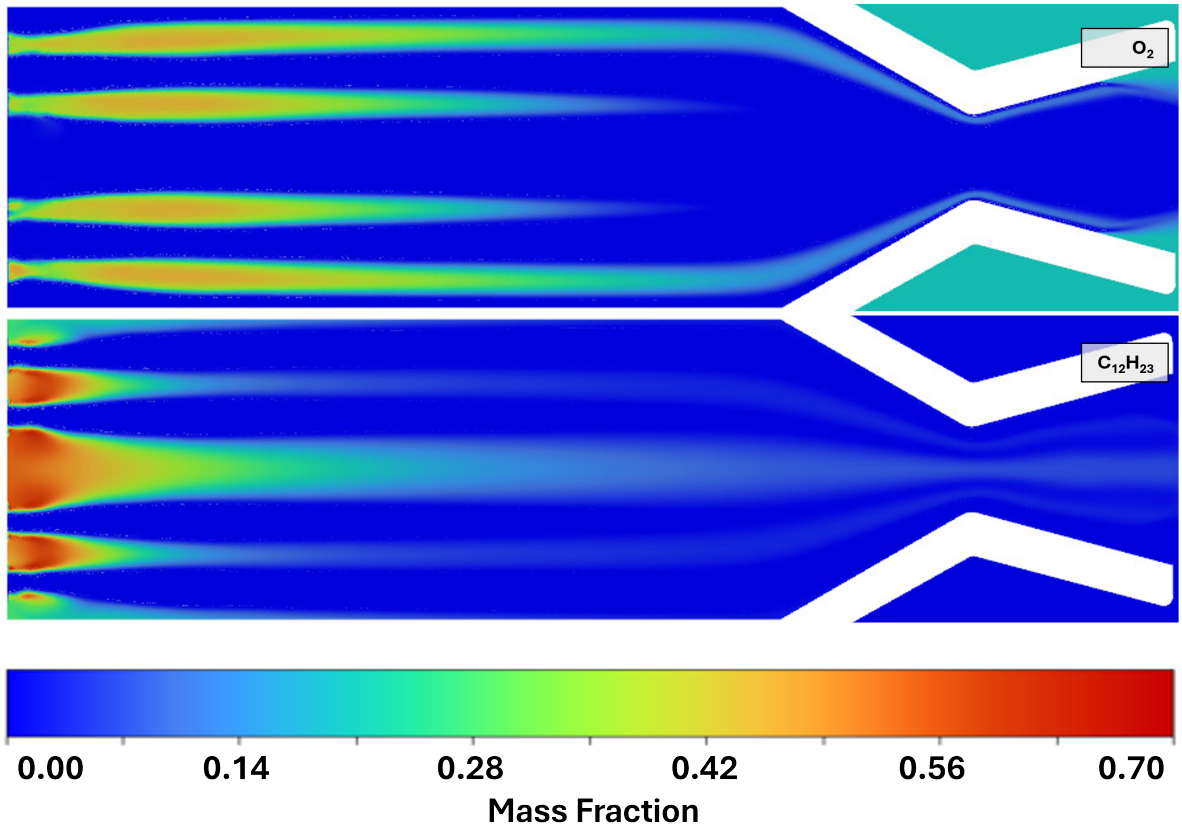

Figure 5.13: Oxygen and Kerosene mass fractions throughout the chamber

Table 5.5: Total Species Composition by mass at Nozzle Exit

	c98st	**c98hp**	**c95st**	**c95hp**
$C_{12}H_{23}$	0.81%	1.80%	0.76%	1.40%
H_2O_2	0.00%	0.00%	0.00%	0.00%
H_2O	45.09%	44.45%	45.78%	45.44%
O_2	6.40%	5.43%	6.44%	5.74%
CO_2	26.40%	26.75%	25.58%	25.92%
N_2	21.31%	21.57%	21.44%	21.51%
Σ	100.00%	100.00%	100.00%	100.00%

To be able to consider the exhaust gas without the atmosphere, the mass fraction of atmospheric gas at the nozzle exit was calculated based on the N_2 fraction and the exhaust gas composition was scaled accordingly (Table 5.6).

Table 5.6: Mass fraction - Correction for atmospheric backflow

	c98st	**c98hp**	**c95st**	**c95hp**
Atmosphere	26.97%	27.30%	27.14%	27.23%
Exhaust	73.03%	72.70%	72.86%	72.77%
O_2 **corrected**	0.74%	-0.30%	0.74%	0.02%

The atmospheric oxygen was subtracted from the total oxygen mass fraction, leading to negative values for one fuel-rich case. Negative mass fractions per se do not have a physical meaning. The negative

value was caused due to the scaling differentiating between the mass sources, either the engine or the atmosphere. A negative value means that the composition at the exit contained less oxygen than what was flowing in from the atmosphere, hence, in addition to the injected propellant, atmospheric oxygen was consumed and combustion must have happened all the way to nozzle exit (and likely beyond).

Table 5.7 shows the mass fractions for the exhaust. Comparing the fuel mass fractions of $C_{12}H_{23}$ and CO_2 allowed to derive how much fuel remained unburnt. While the fuel-rich mixtures had 15% and 10% more fuel injected, the amount of unburnt fuel increased by 100% and 70%, respectively, indicating that most of the additional fuel injected in the fuel-rich cases was simply vaporised and heated but not combusted, thus decreasing the performance. Overall, between 8.56% to 17.58% of the injected kerosene left the chamber unburnt.

Table 5.7: Exhaust Species Composition by mass at Nozzle Exit

	c98st	**c98hp**	**c95st**	**c95hp**
$C_{12}H_{23}$	1.10%	2.48%	1.04%	1.92%
H_2O_2	0.00%	0.00%	0.00%	0.00%
H_2O	61.74%	61.14%	62.83%	62.44%
O_2	1.01%	-0.42%	1.02%	0.03%
CO_2	36.14%	36.80%	35.11%	35.62%
Σ	100.00%	100.00%	100.00%	100.00%
Unburnt/Injected Fuel	8.80%	17.58%	8.56%	14.56%

Not just from the perspective of wall temperature but also considering the fuel efficiency, the coaxial injector did not appear to be optimal. As discussed, a pintle or impinging-jet injector would have likely improved the mixing.

5.4. Wall Loads

While higher loads during start-up are generally possible, for example due to combustion instability, they were found to be negligible in this setup. Hence, for the wall loads, thermal and mechanical steady-state loads were considered, as the steady-state loads exceeded the loads during start-up and thus are more relevant for the structural dimensioning and analysis. Furthermore, the time required to achieve a steady flow was small compared to the time required to reach steady state in the structure, thus the transient part could be neglected.

As discussed in Section 2.2.1, the resolution near the wall, quantified by y^+, is important to accurately model loads at the wall. Figure 5.14 shows the y^+ obtained in the final simulations. The viscous sublayer was resolved throughout most of the chamber up until the throat. The resolution at the throat itself was beyond a y^+ of 30, meaning, the first grid cell was positioned in the fully turbulent flow, where the wall function is used to model turbulence. The intermediate region ($5 < y^+ < 30$) is problematic for many turbulence models, which is why k-ω SST was selected. It is preferably used for near-wall modelling, but is rather insensitive to varying resolution due to its blending of k-ω and k-ϵ. Regardless, further increasing the near-wall resolution in the nozzle might improve the accuracy of results.

5.4.1. Wall Temperature

The maximum allowable temperature was defined as $2500°C$ or $2773K$, based on considerations made for the development of the UHTCMC. The simulations showed that while the temperature in the middle of the chamber, i.e., close to the symmetry axis, was in line with data obtained from CEA, the highest

temperatures were reached at the wall (Figure 5.15) and exceeded the temperature limit by about. $500K$. This was likely due to the adiabatic wall boundary condition. This choice of boundary condition may have had a minor influence on the engine performance, as much more energy left the chamber through the nozzle exit than through the walls. For the wall loads however, this had a significant impact, as no energy could be dissipated there. In reality, convection to the atmosphere (if on ground) and radiation (dominant in space), would cool the chamber walls, leading to a temperature gradient across the wall. In turn, the wall temperature obtained should not be higher than the flame temperature and temperature should generally decrease with distance from the reaction. While preliminary simulations

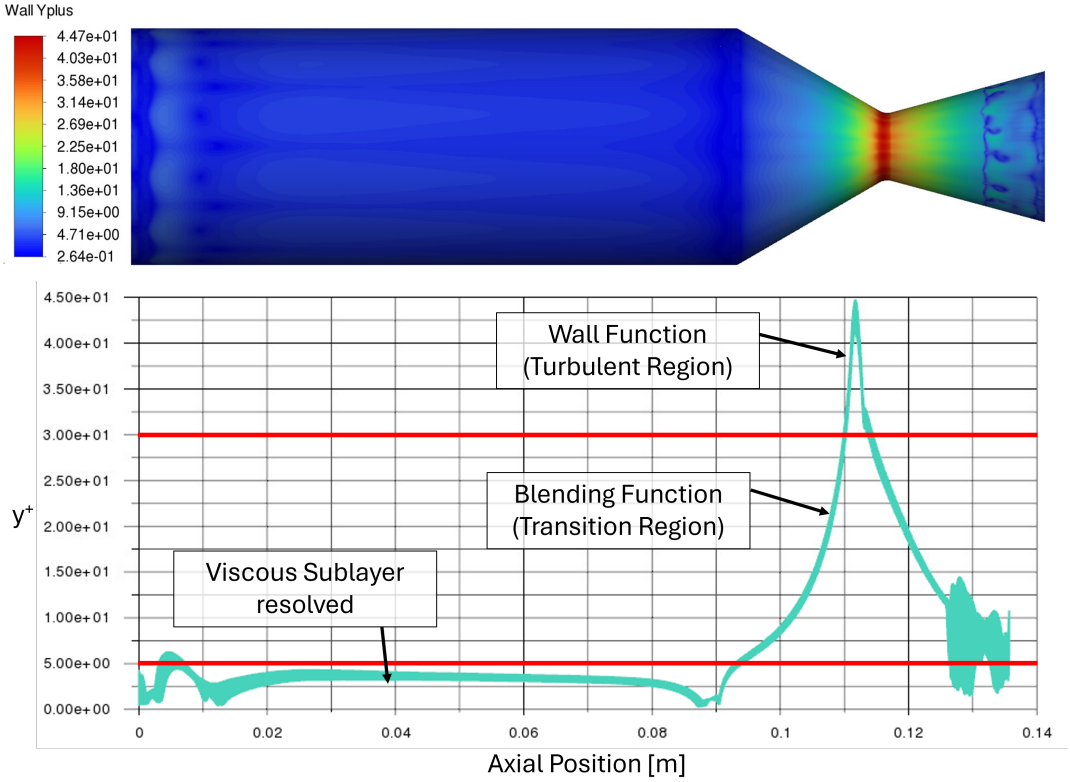

Figure 5.14: y^+ 3D contour (top) and plot over axial distance, highlighting different zones (bottom)

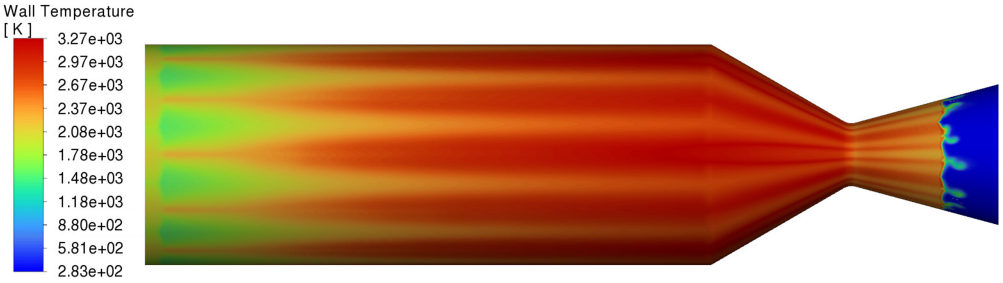

Figure 5.15: 3D-contour of temperature on the inside of the chamber wall (*c98st*)

were disregarded because the wall-temperatures of, e.g., $300K$ or $1800K$, could not be verified for the startup phase, the adiabatic condition clearly led to an unrealistic increase in thermal loads. Future simulations should attempt to accurately model the wall-heat-transfer, possibly resulting in acceptable wall temperatures.

Regardless of the thermal boundary condition, high temperature zones could be seen that reflected the

injection pattern. Having an injection more distributed around the circumference or more concentrated towards the centre could thus lead to more moderate wall temperatures in between the high (red) and low (yellow) zones visible in the contour. A pintle or impinging-jet injector could provide this distribution, while also potentially providing a film-cooling effect to the wall. The coaxial injector could be adapted by, e.g., adding a central injection element, injecting more propellant through the interior injection elements and removing or downsizing the outer ring of injectors.

Figure 5.16 shows wall temperature plots for the different propellants. The highest wall temperature was reached in the *c98st* case ($\alpha = 98\%$, $\Phi = 1.00$) with $3271K$, the lowest in *c95hp* ($\alpha = 95\%$, $\Phi = 1.10$) with $3194K$. The difference between equivalence ratios for a given concentration was less than a percent, whereas reducing the concentration made a difference of about 2%.

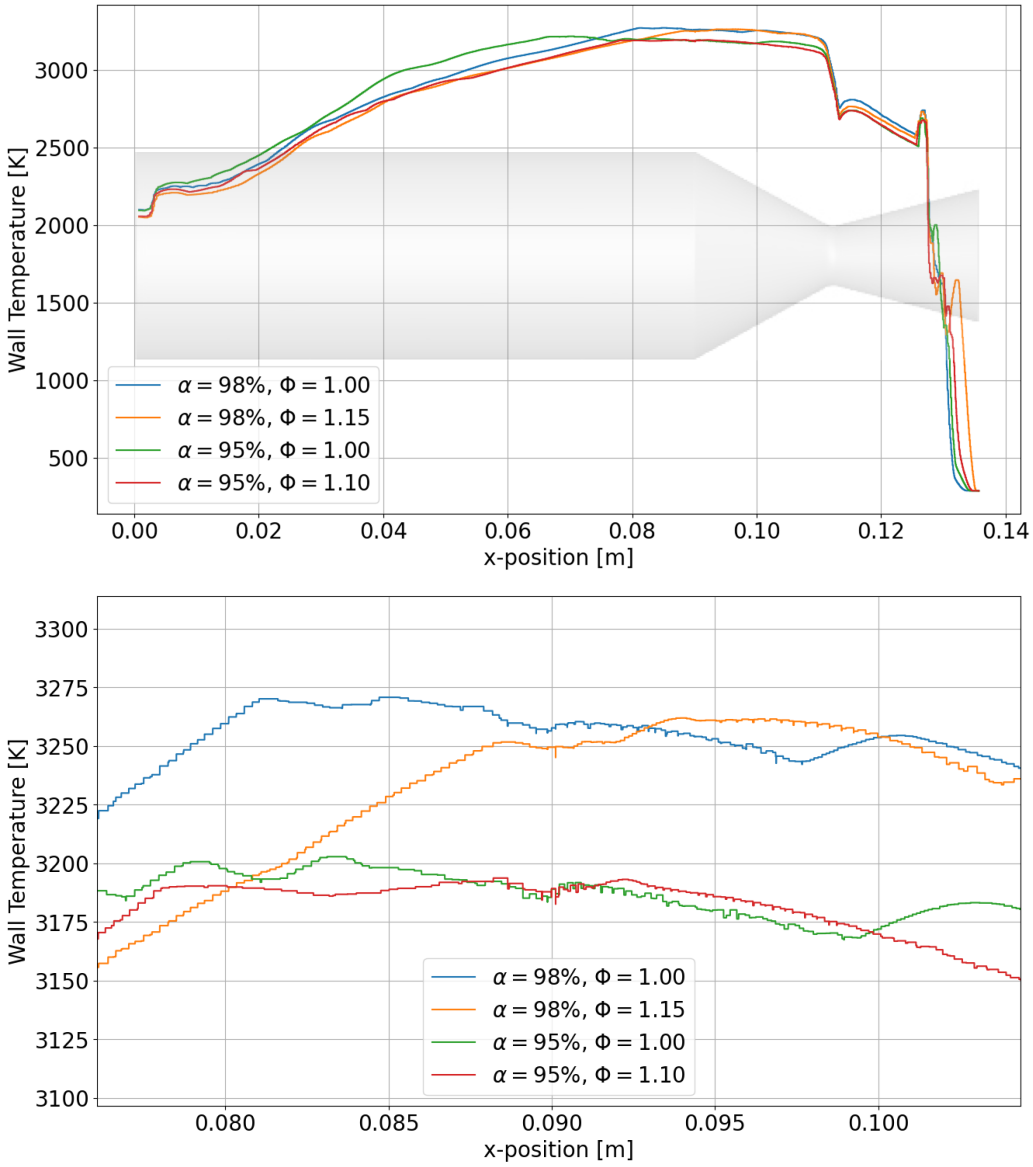

Figure 5.16: Wall temperature for different propellants; whole chamber (top) and nozzle entrance (bottom)

The higher concentration cases led to a higher maximum wall temperature. A possible cause could be the generally high concentration of oxidiser close to the wall (Figure 5.13). While the oxidiser streams

were not in direct contact with the wall, the higher decomposition temperature in the higher concentration cases may have led to a higher wall temperature. The axial shift of the wall temperature peak of a few millimetres between the stoichiometric and the fuel-rich mixtures could be due to the combustion being delayed in the fuel-rich cases, as the mixing of fuel and oxidiser was inferior compared to the stoichiometric cases. Due to the differences in pressure, temperature etc. inside the chamber, the separation in the nozzle likely occurred at slightly different locations and the overall compression-expansion pattern might have changed, causing the differences in wall temperature after the throat.

5.4.2. Heat Transfer Coefficient

Before the nozzle, the heat transfer coefficient was $750W/\left(m^2K\right)$. The maximum heat transfer occurred in the throat, as the local temperature was relatively high and the diameter is the lowest. The difference between the cases was less than 2%. The highest value was obtained for *c98hp* with $4676W/\left(m^2K\right)$, the lowest value for *c98st* with $4600W/\left(m^2K\right)$ (Figure 5.17).

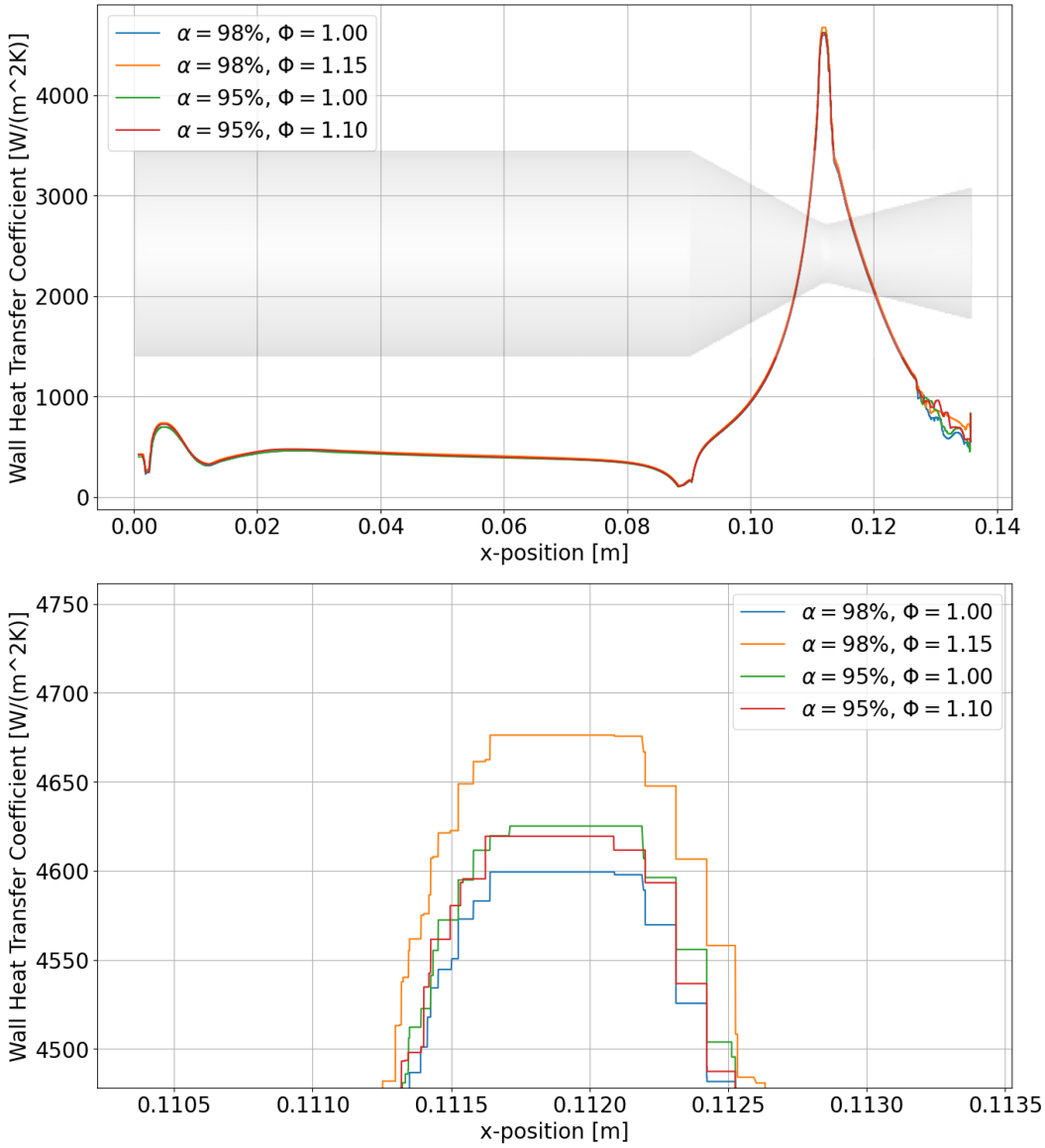

Figure 5.17: Conductive y^+-based Wall Heat Transfer Coefficient for different propellants; whole chamber (top) and throat (bottom)

As explained in Section 4.4.3, the y^+-based heat transfer coefficient generally showed good agreement with the result calculated with Bartz' formula (Equation 4.9), but led to an overestimation at the throat by a factor of 2. One reason for the discrepancy might be the higher $y+$-value throughout the nozzle and especially around the throat (see Figure 5.14). Furthermore, as evident from Equation 4.11, a higher wall temperature (or gas temperature at the wall) leads to a higher convective heat transfer. If the thermal wall boundary condition was non-adiabatic and consequently the wall temperature was lower, both the heat transfer calculated from Bartz' formula and the y^+-based estimation could become lower.

Radiative heat transfer has been neglected in this thesis.

5.4.3. Mechanical Loads

Wall Shear Stress

The wall shear stress was highest in the throat and varied from $2471Pa$ ($\alpha = 98\%$, $\Phi = 1.15$) to $2506Pa$ ($\alpha = 98\%$, $\Phi = 1.00$), a difference of 1.4% (Figure 5.18). The shear stress varied similarly to the velocity which also peaked in the throat, since shear stress is proportional to the velocity gradient (Equation 2.21).

Pressure

The static pressure was approximately constant throughout the chamber and approximately identical to the total pressure, since the velocity in the chamber was low (section 5.2). The maximum static pressure was between 7.54 and $7.66bar$, or between 6.53 and $6.65bar$ when considering gauge pressure, i.e., the differential pressure between the inside and the outside of the chamber. When dimensioning the chamber for ground tests, the gauge pressure is relevant. However, when launching the engine into space, the ambient pressure would decrease while chamber pressure would remain constant. Hence, the differential pressure would increase after launch.

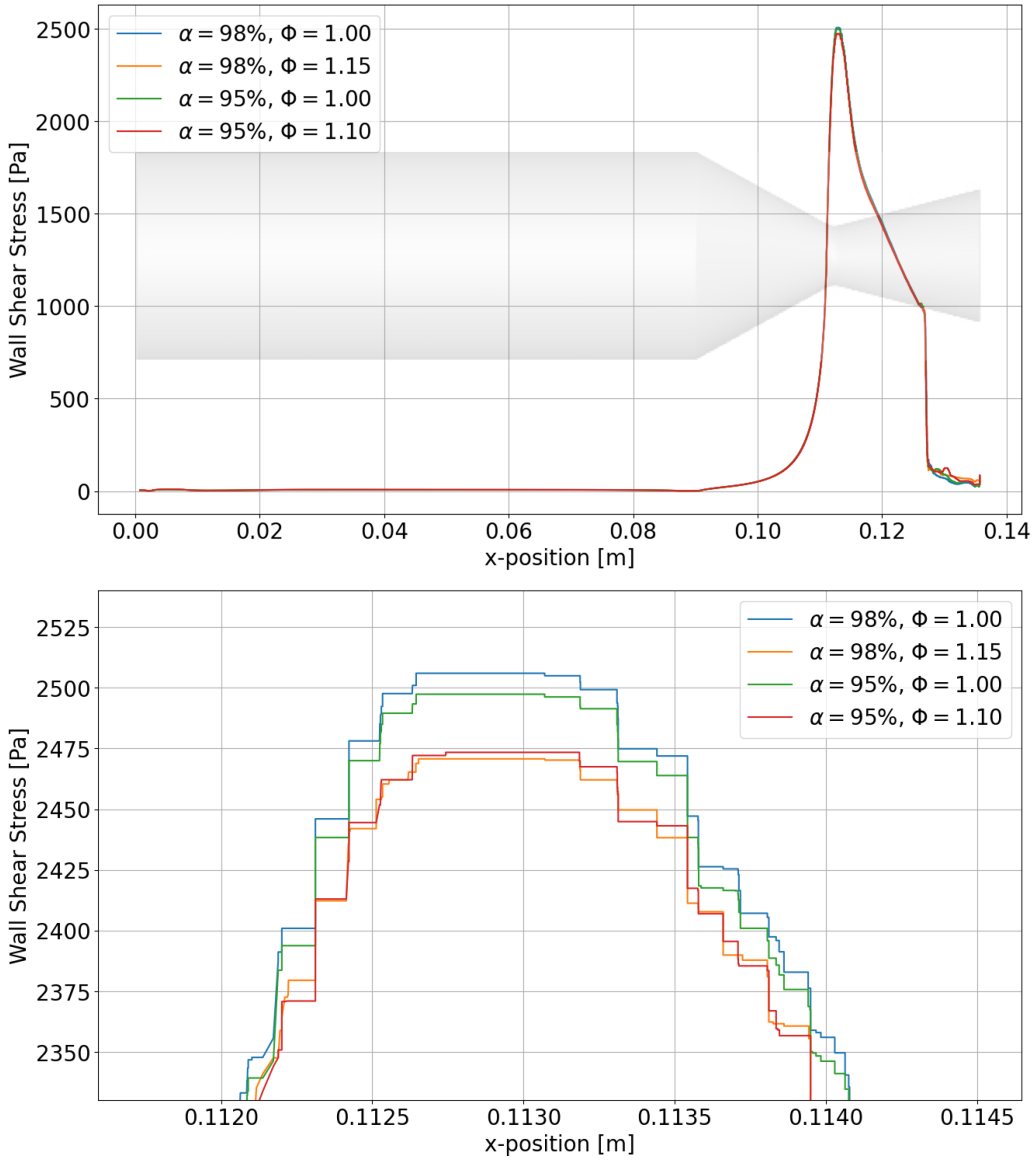

Figure 5.18: Wall Shear Stress for different propellants; whole chamber (top) and nozzle entrance (bottom)

5.5. Summary of Results with regard to the Research Questions

This section summaries the results and discusses to what extent they address the research questions defined in Section 3.1.3. Key results are listed in Table 5.8.

Table 5.8: Summary of results for different propellants

Mixture	$\alpha = 98\%$, $\Phi = 1.00$	$\alpha = 98\%$, $\Phi = 1.15$	$\alpha = 95\%$, $\Phi = 1.00$	$\alpha = 98\%$, $\Phi = 1.10$
Mass Flow Rate $[g/s]$	36.75	36.50	37.12	36.89
Thrust $[N]$	63.22	61.88	63.00	62.09
$I_{sp,sl}$ $[s]$	175.36	172.82	173.01	171.57
Temperature (Centre) $[K]$	2763	2682	2724	2666
Temperature (Wall) $[K]$	3271	3262	3216	3194
Heat Transfer Coefficient $[W/(m^2K)]$	4599	4676	4625	4619
Chamber Pressure $[bar]$	7.66	7.54	7.65	7.57
Velocity (Centre) $[m/s]$	2261	2212	2256	2222
Wall Shear Stress $[Pa]$	2506	2471	2497	2463
Unburnt Kerosene $[\%]$	8.80	17.58	8.56	14.56

5.5.1. What are the characteristics of the flow and combustion in the engine?

- *How do temperature, pressure and velocity change throughout the chamber?*
- *How do results differ for different propellant combinations?*
- *Are there any combustion instabilities?*
- *If so, where and to what extent? What causes these instabilities?*

The **flow characteristics**, namely, pressure, velocity and temperature were analysed looking at the development over time from start of injection up to steady-state and the difference between different propellants during steady state. Especially the analysis of **temperature** was insightful, directly reflecting the occurrence of reactions and translating to loads on the chamber structure. With the assumed Arrhenius parameters and the selected temporal and spatial resolution, ignition was visible within the first $10ms$, steady state was reached within $60ms$. For similar engines, an IDT between $4ms$ and $17ms$ [51] and a time to steady-state of $80ms$ [53] were reported, confirming the order of magnitude of the startup time. However, changing either Arrhenius rate parameters, time-step size or mesh resolution is expected to increase or reduce that time. The qualitative shape of the transient curve is expected to remain the same. A peak temperature of $2763K$ was reached on the symmetry axis, which is a deviation of less than 1% from the CEA prediction and just within the temperature limit defined for the wall. However, local temperatures of up to $3275K$ were found where oxidiser and fuel mix and react, which due to the injector geometry happens close to the wall. Overall higher temperatures were observed for higher HTP concentrations, and lower temperatures were observed for fuel-rich mixtures. This was attributed to a higher ratio of unburnt and thus colder fuel in the chamber. The fuel-rich propellant with lower HTP-concentration thus led to a temperature of approximately $97K$ less at the centre of the engine and $77K$ less at the wall, compared to the hottest propellant.

The peak **velocity** values lay between 2240 and $2300m/s$ and deviated more from the CEA results compared to the temperature, as CEA does not take into account the flow separation. Not much can be derived from these values. More insight could be gained from the velocity contour and its development over time. The first decomposition and consequent acceleration of the fluid could be seen. At the

nozzle, further acceleration with initially attached flow was visible, until the flow separated and Mach diamonds, a sign of stable, overexpanded supersonic flow, formed.

The chamber **pressure** required for the given thrust and the given chamber was found to be approximately 7.5 to $7.6bar$, and followed a curve which is common throughout most rocket engines, being highest and approximately constant throughout the chamber and rapidly decreasing across the throat. Due to the overexpansion, the pressure dropped below ambient pressure at the exit and subsequently also showed a Mach diamond pattern. A Mach diamond (or shock diamond) itself is a combination of an expansion fan and a compression wave (or oblique shock).

The complete animations of temperature, pressure and velocity can be found in section A.5.

While **engine performance** was not explicitly framed as a research question, it was a central requirement of the engine development and allowed to gain some insights. While all four mixtures resulted in slightly higher thrust than the analytical result ($3-5\%$), they also showed deviations between each other of up to 2%. In line with the results obtained for temperature, the fuel rich mixtures delivered less thrust than the stoichiometric mixtures. While the theoretical I_{sp} was higher for fuel-rich mixtures, the amount of unburnt fuel due to insufficient mixing was too large and hence led to decreased performance.

During the course of the thesis, the investigation of **combustion instability** was deemed infeasible. Different methods, both analytical and numerical, exist, and there is no general consensus on which methods work best to model and predict instability. Furthermore, it appears that a) combustion instability is an issue rather in larger combustion engines, and b) can be avoided by using appropriate injectors, especially pintle injectors.

5.5.2. What loads on the wall can be expected?

- *What structural loads, i.e., pressure and shear forces, are present?*
- *What thermal loads, i.e., convection and radiation, are present?*

While the central chamber temperatures were similar to the maximum allowable wall temperature, temperatures in all cases peaked at the walls for two reasons: the adiabatic boundary condition prevented the wall from cooling, and the injector setup led to a high fraction of the combustion happening close to the wall. Maximum wall temperatures were between $3194K$ and 3271, approximately $500K$ above the allowable temperature. From a simulation perspective, it is expected that these temperatures would lower significantly if the thermal boundary allowed for heat transfer to the exterior. From a design perspective, this could be addressed by changing the injector. Either a different injector type could be used, e.g., pintle or impinging-jet injector, or the coaxial injector could be adapted such that more propellant injection and mixing occur closer to the chamber symmetry axis.

Heat Transfer peaked at the throat with values between $h = 4600W/\left(m^2K\right)$ and $h = 4676W/\left(m^2K\right)$. Nothing could derived with regards to differences in heat transfer for different concentrations or equivalence ratios. The peak transfer exceeded the estimation made with Bartz by a factor of 2. In the chamber before the nozzle, the heat transfer was below $750W/\left(m^2K\right)$. As the heat transfer depends on the wall temperature, the heat transfer was likely higher than in reality with a lower wall temperature.

Shear stress was approximately identical for the four cases and peaked at the throat with $\tau \approx 2500\ Pa \pm 1\%$. Static gauge pressure was approximately $6.6 \cdot 10^5\ Pa \pm 1\%$.

5.5.3. What combustion products can be expected?

- *How does the chemical composition change throughout the engine?*
- *What is the composition of the exhaust?*
- *Is nozzle erosion to be expected, e.g., by high oxygen concentrations?*
- *Is nozzle clogging to be expected, e.g., by high soot concentrations?*

All hydrogen peroxide was decomposed in all cases. The exhaust consisted mostly of carbon dioxide and water, as no unsaturated combustion products were considered. As discussed above, all cases, whether fuel-rich or stoichiometrically mixed, still had unburnt kerosene in the exhaust, as no optimal mixing could be obtained with the coaxial injector. The ratio of unburnt to injected fuel was as high as 18.68% - too high from an environmental perspective but also from a perspective of efficiency, as the unburnt kerosene does not contribute thrust. Improved mixing, primarily achieved by adapting the injector design, could decrease the amount of unburnt fuel. Soot formation was not modelled in this thesis. However, especially fuel-rich combustion can generally lead to the formation of solid carbon particles, i.e., soot, which can lead to clogging. To analyse nozzle clogging, it would be necessary to introduce solid particles to the Discrete Phase Model and define how they are created. To analyse nozzle erosion, two phenomena would need to be considered: erosion can be caused by abrasion, i.e., the shear stress caused by the flow would need to be compared to the material strength. Furthermore, erosion can be caused by oxidation of the wall material, leading to changes in material and, for example, making it brittle. Hence, a more comprehensive wall material model would be required and the reaction mechanism would need to be more detailed to include radicals.

6

Conclusion

6.1. Summary

The objective of this thesis was to gain insight into and characterise the behaviour of the *Greenlam* engine. The engine is a non-staged hypergolic thruster using hydrogen peroxide and kerosene with a catalytic additive to produce up to $100N$ of vacuum thrust, and is currently under development at the Space Systems Engineering group at the Faculty of Aerospace Engineering, TU Delft. To that end, different models were identified, discussed, tried and validated and CFD simulations with different boundary conditions were performed.

Since the injector design had not been finalised prior to this thesis, three different existing injectors were taken from literature and considered for this engine: a coaxial injector, an impinging-jet injector and a pintle injector. Using Ansys Fluent, transient and three-dimensional simulations were performed to analyse the start-up behaviour and to accurately reflect the injector geometry, respectively. Thermal and catalysed decomposition of hydrogen peroxide as well as combustion of kerosene were modelled with the Finite Rate Species Transport model, as this model allowed to consider the Arrhenius rate parameters which are influenced by adding a catalyst to the propellants. The Arrhenius parameters assumed in this thesis were taken from previous cases of thermal and catalytic decomposition of hydrogen peroxide, although they may be different for a different catalyst. A deviation would have a significant impact on the transient engine behaviour, the prediction of which could consequently be improved by determining the real Arrhenius rate parameters, for example by performing drop-tests with oxidiser and propellant for different concentrations of HTP and catalyst, for different O/F ratios and for different temperatures. The steady-state characteristics are expected to remain unchanged. The liquid phase was modelled as a Lagrangian Discrete Phase to improve the simulation of the injection, breakup and evaporation. The Eulerian multiphase model was also considered, but showed that due its vaporisation model (Lee) not including evaporation, it could not represent the system. The gaseous phase was modelled as a continuous phase with the Peng-Robinson real gas model. Turbulence was modelled with k-ω SST to combine accurate mean flow modelling (k-ϵ) with accurate boundary layer modelling (k-ω). NASA Chemical Equilibrium with Applications was used to estimate the performance for varying H_2O_2-concentrations and equivalence ratios.

Following a mesh study, an unstructured tetrahedral mesh with 8.37 million nodes was used.

To validate the set of models, papers discussing experimental work on hydrogen peroxide-hydrocarbon engines were attempted to be replicated in Fluent. The replication did not work, possibly either due to insufficient information on propellant and boundary conditions or due to a mismatch between the spatial and temporal resolution necessary to simulate the droplet impingement in these papers, and the computational resources available. The coaxial injector was consequently the only injector that could be simulated due to the setup's inability to capture droplet impingement. Subsequently, validation was performed by quantitative comparison to CEA data and qualitative comparison to other engines, showing good agreement in both cases.

Four different propellant mixtures were simulated with a coaxial injector. Thrust for all cases was between 62 and $63N$, 5-7% higher than the theoretical sea level value. Temperatures at the centre of the engine were between 2666 and $2763K$, temperatures at the wall between $3194K$ and $3271K$. The higher performance compared to CEA was attributed to the reaction model, which did not consider intermediate combustion products but only saturated products, and only forward reaction rates rather than equilibrium. The increase in temperature towards the wall was attributed to the injection pattern, leading to strong mixing and combustion close to the wall rather than in the centre, and to the adiabatic boundary condition, preventing the engine wall from being cooled by the surroundings. The obtained wall temperature was approximately $500K$ higher than the estimated allowable wall temperature.

The stoichiometric mixtures showed higher thrust output, higher chamber temperature and higher wall temperature than the fuel-rich mixtures. The higher concentrations led to higher chamber and wall temperatures. Analysing the kerosene mass fraction in the exhaust showed that oxygen was still present at the nozzle exit, but was spatially separated from the kerosene and thus could not be consumed in the combustion. The fuel-rich mixtures ejected up to twice as much unburnt fuel ($15\% - 18\%$ versus 9%), meaning most of the fuel injected beyond the stoichiometric ratio was not oxidised and did not produce thrust.

6.2. Relevance

A set of models for the numerical analysis of a rocket engine using liquid hydrogen peroxide with a liquid hypergolic fuel was defined and validated, allowing to gain some insights into the flow characteristics and the resulting loads for the Greenlam engine. While the simulations confirmed a functioning and self-igniting engine, the results are strongly dependent on the injector design as well as the catalyst and its effect on the Arrhenius equation. Furthermore, the models have two major shortcomings: Firstly, the adiabatic thermal boundary condition presumably lead to an overestimation of the wall temperature. Hence, conclusions drawn about the wall temperature seem unreliable. Improving the wall boundary condition would lead to improved wall temperature predictions and, through a loss of energy, to a decrease in performance. Secondly, the only injector that could be modelled was the coax injector which in the present configuration showed to be an inferior design choice. Simulating other injectors such as an impinging-jet or pintle injector is desirable for the sake of improved mixing and stability, but could not be realised with the present setup.

Given the increasing growth of the space industry and simultaneously the increasing awareness of environmental issues, not least due to combustion products accelerating Climate Change, the use of *Green Propellants* in spaceflight is inevitable. HTP, especially in combination with kerosene, represents an important step towards environmentally friendly spaceflight, with the emissions containing much less

carbon dioxide compared to oxygen-kerosene engines and being less toxic compared to conventional upper-stage/orbital propellants, i.e., hydrazine-based propellants.

Compared to staged engines, the unstaged configuration investigated here promises significant savings in mass, reducing manufacturing and launch costs but also the material footprint. This thesis researched numerical analysis of the flow and combustion in such an engine, presented viable models and characterised the performance for different compositions of water, hydrogen peroxide and kerosene. More generally, the setup is applicable to bi-liquid hypergolic thrusters with subcritical injection.

6.3. Recommendations for Future Work

Injector Design

- A formal trade-off study between different injector types, e.g., coaxial, impinging and pintle, should be performed. The simplicity of the injector, coupled to cost and reliability, would be one criterion. Pintle injectors are simpler in the sense that they usually rely on a single injection element compared to the potentially numerous elements for a coaxial injector. More important criteria would be mixing, combustion stability and wall temperature. Considering the simulation results, the coaxial injector shown here does not seem suitable due to insufficient mixing and heat concentration near the wall. Angling the injector elements, effectively creating an impinging-jet injector, could improve mixing. Inserting more of the propellants near the centre could reduce the wall loads. Lastly, at the cost of performance, the equivalence ratio could be shifted to the oxidiser-rich regime.

Further Simulations

- To improve the estimation of wall temperatures, simulations with more elaborate thermal wall boundary conditions are necessary. The heat transfer coefficients obtained in this thesis could be used as preliminary values to setup further simulations.
- Simulations with ambient conditions equivalent to flight altitude should be performed to confirm that under ambient pressure close to zero, there would be no flow separation, no overexpansion and that thrust would reach the required $100N$. However, since the flow becomes supersonic after crossing the throat, flow and combustion inside the chamber would not change once sonic flow is achieved, except for heat transfer through walls.

Combustion Instability

- Combustion instability should be investigated. As this phenomenon can lead to rapid destruction of the chamber, this should preferably be done before hot fire testing, i.e., either through numerical or analytical methods.
- Feed fluctuations leading to instabilities could be modelled by performing a transient simulation with a sine or random fluctuation mass flow inlet function. Since instabilities can also be caused by vibrations induced by the vehicle, a Coupled Loads Analysis could eventually be considered.

Experimental Validation

- While simulations provide good insight and the setup has been validated, no experimental work has been conducted. Cold flow testing would allow to confirm a detailed injector design as well as provide accurate droplet sizing, enabling an improved simulation. Furthermore, the exact

reaction mechanism to date is unknown and only hot fire testing would confirm its accuracy and substantiate the overall setup. A trend generally rather seen in the New Space industry is to proceed with testing more quickly rather than improving the simulations.

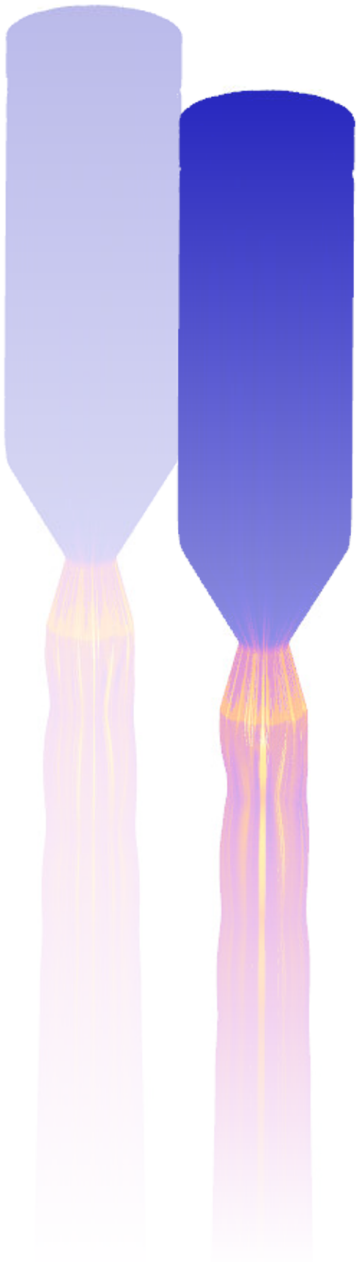

Bibliography

[1] Jonathan McDowell. Jonathan's Space Report, 2024. URL https://planet4589.org/space/gcat/data/derived/launchlog.html.

[2] J. Bouwmeester. *The Architecture of CubeSats and PocketQubes: Towards a Lean and Reliable Implementation of Subsystems and Their Interfaces*. PhD thesis, Delft University of Technology, 2021.

[3] Adam Okninski, Bartosz Bartkowiak, Kamil Sobczak, Dominik Kublik, Paweł Surmacz, Grzegorz Rarata, and Blazej Marciniak. Development of a Small Green Bipropellant Rocket Engine Using Hydrogen Peroxide as Oxidizer. *AIAA Spacecraft Propulsion Systems*, AIAA 2014-3592, 2014.

[4] satnews. Skyrora Completes Successful Test Firings Of Their LEO Engine, 2020. URL https://news.satnews.com/2020/11/17/skyrora-completes-successful-test-firings-of-their-leo-engine/.

[5] Prakhar Jindal. Lightweight, Cost-effective Composite and Green Bipropellant System for Space Transportation Applications (Greenlam). Research Proposal, 2023.

[6] K. E. Tsiolkovsky. *Collected Works of K. E. Tsiolkovskiy, Volume II - Reactive Flying Machines*. 1954.

[7] B.T.C. Zandbergen. *Thermal Rocket Propulsion*. Faculty of Aerospace Engineering, Delft University of Technology, 2022.

[8] Mechanical Aerospace Engineering. Incompressible, Compressible, and Supersonic Flow Fields: Static, Dynamic, and Total Pressure. *Utah State University*, 2021.

[9] Bruce Chehroudi, Doug Talley, and Vigor Yang. Liquid Propellants and Combustion: Fundamentals and Classifications. *Encyclopedia of Aerospace Engineering, Wiley & Sons*, 2010.

[10] G. P. Sutton and O. Biblarz. *Rocket Propulsion Elements*. Wiley, 2017.

[11] J.S. Mok, W.J. Helms, J.C. Sisco, and W.E. Anderson. Decomposition and Vaporization Studies of Hydrogen Peroxide. *AIAA/ASME/SAE/ASEE Joint Propulsion Conference*, 2022.

[12] MIT OpenCourseWare. Decomposition of H2O2 with MnO2, 2012. URL https://ocw.mit.edu/courses/res-hs-002-chemistry-behind-the-magic-chemical-demonstrations-for-the-classroom/steaming_gun.pdf.

[13] Claudio M. Lousada, Adam Johannes Johansson, Tore Brinck, and Mats Jonsson. Mechanism of H2O2 Decomposition on Transition Metal Oxide Surfaces. *The Journal of Physical Chemistry*, 2012.

[14] Cláudio M. Lousada, Miao Yang, Kristina Nilsson, and Mats Jonsson. Catalytic Decomposition of Hydrogen Peroxide on Transition Metal and Lanthanide Oxides. *Journal of Molecular Catalysis*, 2013.

[15] Eric Croiset, Steven F. Rice, and Russel.G. Hanush. Hydrogen Peroxide Decomposition in Supercritical Water. *Applied Thermal Engineering*, 2010.

[16] S. Bonifacio and A. Russo Sorge. Modelling Hydrogen Peroxide Decomposition in Monolithic Beds. *Proceedings of 3rd International Conference on Green Propellant for Space Propulsion and 9th International Hydrogen Peroxide Propulsion Conference*, 2006.

[17] Si-Hyun Do, Bill Batchelor, Hong-Kyun Lee, and Sung-Ho Kong. Hydrogen Peroxide Decomposition on Manganese Oxide (Pyrolusite): Kinetics, Intermediates, and Mechanism. *Chemosphere 75 (2009) 8–12*, 2009.

[18] Dongwook Jang, Shinjae Kang, and Sejin Kwon. Preheating Characteristics of H2O2 Monopropellant Thruster using Manganese Oxide Catalyst. *Aerospace Science and Technology 41 (2015) 24–27*, 2015.

[19] Sungkwon Jo, Sungyong An, Jonghak Kim, Hosung Yoon, and Sejin Kwon. Performance Characteristics of Hydrogen Peroxide/Kerosene Staged-Bipropellant Engine with Axial Fuel Injector. *JOURNAL OF PROPULSION AND POWER*, Vol. 27, No. 3, May–June 2011, 2011.

[20] Jakusz SpaceTech. 85 URL `https://jakusz-spacetech.com/products/98-hydrogen-peroxide-htp/`.

[21] Irfan Javed, Seung Wook Baek, and Khalid Waheed. Autoignition and Combustion Characteristics of Kerosene Droplets with Dilute Concentrations of Aluminum Nanoparticles at Elevated Temperatures. *Combustion and Flame*, 162, 2015.

[22] Yu Cong, Tao Zhang, Tao Li, Jiwen Sun, Xiaodong Wang, Lei Ma, Dongbai Liang, and Liwu Lin. Propulsive Performance of a Hypergolic H2O2/Kerosene Bipropellant. *JOURNAL OF PROPULSION AND POWER*, Vol. 20, No. 1, January-February 2004, 2004.

[23] S.A. Frolik and B.L. Austin. Development of Hypergolic Liquid Fuels for Use With Hydrogen Peroxide. *39th AIAA Aerospace Sciences Meeting & Exhibit*, 2001.

[24] Thomas J. Bruno and Beverly L. Smith. Improvements in the Measurement of Distillation Curves. 2. Application to Aerospace/Aviation Fuels RP-1 and S-8. *Industrial & Engineering Chemistry Research*, 2006.

[25] A. Coclite, L. Cutrone, P. De Palma, and G. Pascazio. Numerical Investigation of High-Pressure Combustion in Rocket Engines using Flamelet/Progress-variable models. *AIAA SciTech Forum*, 53rd AIAA Aerospace Sciences Meeting, 2015.

[26] Chi-Ming Lee, Krishna Kundu, and Bahman Ghorashi. Simplified Jet-A Kinetic Mechanism for Combustor Application. *31st Aerospace Sciences Meeting, AIAA*, 1993.

[27] John W. Slater. Uncertainty and Error in CFD Simulations, url = https://www.grc.nasa.gov/www/wind/valid/tutorial/errors.html, urldate = 2021-02-10, year = 2024.

[28] J. Warnatz, U. Maas, and R. W. Dibble. *Combustion - Physical and Chemical Fundamentals, Modeling and Simulation, Experiments, Pollutant Formation*. Springer, 2006.

[29] Princeton University. Transition and Turbulence, 2024. URL https://www.princeton.edu/~asmits/Bicycle_web/transition.html.

[30] Zhen-Guo Wang. *Internal Combustion Processes of Liquid Rocket Engines - Modeling and Numerical Simulations*. Wiley, 2016.

[31] ANSYS Inc. Introduction to ANSYS Fluent - Turbulence Modelling. Dec. 2010, 2010.

[32] ANSYS Inc. *Ansys Fluent Theory Guide, Release 2023 R2*. Ansys Inc., 2023.

[33] Sen Li, Yifei Ge, Xiaolin Wei, and Teng Li. Mixing and Combustion Modeling of Hydrogen Peroxide/Kerosene Shear-Coaxial Jet Flame in Lab-scale Rocket Engine. *Aerospace Science and Technology*, 56 (2016), 2016.

[34] Seyed Reza Taghavi, Mohammad Ali Dehnavi, and Ali Ghafouri. Numerical Analysis of Reactive Turbulent Flow in the Thrust Chamber of RD-108 Engine Rocket. *Defence Technology*, pages 565–575, 2018.

[35] Y.M. Kim, C.P. Chen, J.P. Ziebarth, and Y. S. Chen. Prediction of High Frequency Combustion Instability in Liquid Propellant Rocket Engines. *AIAA/SAE/ASME/ASEE*, 28th Joint Propulsion Conference and Exhibit, 1992.

[36] Pasquale Eduardo Lapenna, Giuseppe Indelicato, Rachele Lamioni, and Francesco Creta. Modeling the Equations of State using a Flamelet Approach in LRE-like Conditions. *Acta Astronautica*, Acta Astronautica Volume 158, May 2019, Pages 460-469, 2019.

[37] Gary C. Cheng and Richard Farmer. Real Fluid Modeling of Multiphase Flows in Liquid Rocket Engine Combustors. *Journal of Propulsion and Power*, Vol. 22, No. 6, 2006.

[38] Zhang HuiQiang, Ga YongJing, Wang Bing, and Wang XiLin. Analysis of Combustion Instability via Constant Volume Combustion in a LOX/RP-1 Bipropellant Liquid Rocket Engine. *SCIENCE CHINA Technological Sciences*, Vol. 55, 2012.

[39] ANSYS Inc. *Ansys Fluent User's Guide, Release 2023 R2*. Ansys Inc., 2023.

[40] Marcelo A. Veloso. Thermodynamic Properties of Water in the Critical Region. *International Nuclear Atlantic Conference*, 2009.

[41] Xunfeng Li, Fengquan Zhong, Xuejun Fan, Xiulan Huai, and Jun Cai. Study of Turbulent Heat Transfer of Aviation Kerosene Flows in a Curved Pipe at Supercritical Pressure. *Applied Thermal Engineering*, 2010.

[42] Guodong Zhang, Guangxi Li, Longfei Li, and Guihua Tang. Thermal Performance of MMH/NTO Rocket Thrust Chamber based on Pintle Injector by using Liquid Film Cooling. *Applied Thermal Engineering*, 223, 2023.

[43] Gary A. Flandro, Joseph Majdalani, and Joseph D. Sims. On Nonlinear Combustion Instability in Liquid Propellant Rocket Engines. *AIAA Journal*, AIAA 2004-3516, 2004.

[44] Jianxiu Qin and Huiqiang Zhang. Numerical Analysis of Self-Excited Combustion Instabilities in a Small MMH/NTO Liquid Rocket Engine. *International Journal of Aerospace Engineering*, Volume 2020, 2020.

[45] T. Govaert, W. Armbruster, J. S. Hardi, D. Suslov, M. Oschwald, and B. T. C. Zandbergen. Wall Heat Loads in a Cryogenic Rocket Thrust Chamber During Thermoacoustic Instabilities. *Journal of Propulsion and Power*, Vol. 37, Nov.-Dec. 2021, 2021.

[46] Rocket & Space Technology. Atmosphere Properties, 2024. URL `http://www.braeunig.us/space/atmos.htm`.

[47] Kent A. Watson and John W. Connell. *Carbon Nanotechnology, Chapter 19 - Polymer and Carbon Nanotube Composites for Space Applications*. Elsevier B.V., 2006.

[48] G. K. Bahr and P. J. Disimile. Space Vehicle Propulsion Systems: Environmental Hazards of Low Earth Orbit-Lunar Domain. *Journal of Spacecraft and Rockets*, Vol. 32, no. 6, Nov.-Dec.1995, 1995.

[49] Pengfei Fu, Lingyun Hou, Zhuyin Ren, Zhen Zhang, Xiaofang Mao, and Yusong Yu. A droplet/wall Impact Model and simulation of a Bipropellant Rocket Engine. *Aerospace Science and Technology*, 88, 2019.

[50] Ilja Müller, Markus Kuhn, Ivaylo Petkov, Sebastian Bletsch, Koen Huybrechts, and P. Van Cauwenbergh. 3D-Printed Coaxial Injector For A Lox-Kerosene Rocket Engine. *SPACE PROPULSION 2018*, 2018.

[51] Hongjae Kang, Dongwook Jang, and Sejin Kwon. Demonstration of 500 N scale Bipropellant Thruster using Non-toxic Hypergolic Fuel and Hydrogen Peroxide. *Aerospace Science and Technology 49*, 2016.

[52] Hongjae Kang, Eunkwang Lee, Yongjun Moon, and Sejin Kwon. Development Status of a 500-N Scale Green Hypergolic Bipropellant Thruster using Hydrogen Peroxide as an Oxidizer. *51st AIAA/SAE/ASEE Joint Propulsion Conference AIAA Propulsion and Energy Forum*, 2015.

[53] B. L. Austin, S. D. Heiser, and W. E. Anderson. Characterization of Pintle Engine Performance for Nontoxic Hypergolic Bipropellants. *Journal of Propulsion and Power*, 2005.

[54] Guodong Zhang, Guangxi Li, Longfei Li, and Guihua Tang. TRW Pintle Engine Heritage and Performance Characteristics. *AIAA/ASME/SAE/ASEE Joint Propulsion Conference*, 36th, 2000.

[55] Delft High Performance Computing Centre (DHPC). DelftBlue Supercomputer (Phase 2). `https://www.tudelft.nl/dhpc/ark:/44463/DelftBluePhase2`, 2024.

[56] Mark Wade. H2O2/Kerosene, 2019. URL `http://www.astronautix.com/h/h2o2kerosene.html`.

[57] O. Maass and P. G. Hiebert. The Properties of Pure Hydrogen Peroxide: V. Vapor Pressure. *Journal of the American Chemical Society*, 1924.

[58] Jeffrey I. Steinfeld, Joseph Salvadore Francisco, and William L. Hase. *Chemical Kinetics and Dynamics*. Pearson, 1998.

[59] Sanford Gordon and Bonnie McBride. Chemical Equilibrium with Applications, 2013. URL `https://cearun.grc.nasa.gov/`.

[60] Felix Lauck, Jan Witte, Michele Negri, Dominic Freudenmann, and Stefan Schlechtriem. Design and first results of an Injector Test Setup for Green Hypergolic Propellants. *AIAA Propulsion and Energy Forum*, 2019.

[61] P. Rosin and E. Rammler. The Laws governing the Fineness of Powdered Coal. *Journal of the Institute of Fuel*, 1933.

[62] Martin Hersch. Hydrogen-Oxygen Chemical Reaction Kinetics in Rocket Engine Combustion. *NASA Technical Note, NASA Lewis Research Center*, 1967.

[63] Maziar Shafaee, Abbas Elkaie, Hamed Fallah, and Jebraiel Bayramlu. Numerical Investigation of Propellant Flow and Finite Element Analysis of Wall Structure for a Bi-propellant Thruster, Compared to Proposed Analytical Results. *International Journal of Mechanical Engineering and Robotics Research Vol. 5*, 2016.

[64] Weiqiang Huang, Chunguang Wang, Kaining Zhang, Zhihong Wang, and Weiping Tian. Study on the Influence of Nozzle Ablation on the Performance of the Solid Rocket Motor. *MDPI Aerospace 2023*, 2023.

[65] Prateek Garg, Abhishek Sharma, Deepak Kumar Agarwal, and Mohan Varma. Numerical Modelling of Liquid Oxygen and Kerosene Combustion at High Pressures. *55th AIAA Aerospace Sciences Meeting*, 2017.

[66] D. R. Bartz. A Simple Equation for Rapid Estimation of Rocket Nozzle Convective Heat Transfer Coefficients. *JPL Technical Notes*, 1957.

A

Appendix

A.1. Propellant Inlet Conditions - Python Code

```
### ENVIRONMENT
import numpy as np

### INPUTS
## PERFORMANCE
# required thrust level [N]
thrust = 100
# sea level propellant specific impulse [s]
isp_sl = 273
# vacuum propellant specific impulse [s]
isp_vac = 319
# gravitational acceleration [m/s**2]
G_0 = 9.80665
# ideal total mass flow [kg/s]
m_total = thrust / (isp_sl * G_0)
print(f"Total Mass Flow: {m_total} kg")


# htp-concentration [-]
alpha = 1

## CHEMISTRY
# molar masses
M_C = 14 # kg/mol
M_H = 1 # kg/mol
M_O = 16 # kg/mol
M_H2O2 = 34 # kg/mol
```

```
M_H2O = 18 # kg/mol
M_O2 = 32 # kg/mol
M_C12H23 = 191 # kg/mol
M_CO2 = 46 # kg/mol

# ratios between species for stoichiometric combustion
# m2/m1 = n2/n1 * M2/M1
o2_k = 17.75 * M_O2/M_C12H23 # from combustion
h2o2_o2 = 2 * M_H2O2/M_O2 # from decomposition
ox_h2o2 = 1/alpha
of = ox_h2o2*h2o2_o2*o2_k
print(f"O/F: {of}")

# fuel mass flow rate [kg/s]
m_f = m_total * 1 / (1 + of)
print(f"Fuel Mass Flow: {m_f} kg")

# oxidiser mass flow rate [kg/s]
m_o = m_total * of / (1 + of)
print(f"Oxidiser Mass Flow: {m_o} kg")
```

A.2. NASA CEA Data

For the sake of brevity, only the input files for the CEA code are provided here. Inserting them in the online tool [59] will provide the data used in this research.

A.2.1. RP-1 & 90% HTP

```
### CEA analysis performed on Mon 27-May-2024 11:53:15

# Problem Type: "Rocket" (Finite Area Combustor)

prob case=_____________5727 ro equilibrium    fac

!Contraction Ratio:
ac/at=12.25

# Pressure (11 values):
p,bar= 5, 5.5, 6, 6.5, 7, 7.5, 8, 8.5, 9, 9.5, 10
# Supersonic Area Ratio (1 value):
supar= 5

# Equivalence based on Fuel/Oxid. wt ratio (Eq 9.19*) (5 values):
phi= 0.9, 0.95, 1, 1.05, 1.1
```

```
# You selected the following fuels and oxidizers:
reac
fuel RP-1              wt%=100.0000  t,k= 288.150
oxid H2O(L)            wt%= 10.0000  t,k= 288.150
oxid H2O2(L)           wt%= 90.0000  t,k= 282.000

# You selected these options for output:
# short version of output
output short
# Proportions of any products will be expressed as Mass Fractions.
output massf
# Heat will be expressed as siunits
output siunits

# Input prepared by this script:/var/www/sites/cearun.grc.nasa.gov/cgi-bin/CEARUN/prepareInputFile.c

### IMPORTANT:  The following line is the end of your CEA input file!
end
```

A.2.2. RP-1 & 95% HTP

```
### CEA analysis performed on Mon 27-May-2024 11:52:11

# Problem Type: "Rocket" (Finite Area Combustor)

prob case=_____________5727 ro equilibrium    fac

!Contraction Ratio:
ac/at=12.25

# Pressure (11 values):
p,bar= 5, 5.5, 6, 6.5, 7, 7.5, 8, 8.5, 9, 9.5, 10
# Supersonic Area Ratio (1 value):
supar= 5

# Equivalence based on Fuel/Oxid. wt ratio (Eq 9.19*) (5 values):
phi= 0.9, 0.95, 1, 1.05, 1.1

# You selected the following fuels and oxidizers:
reac
fuel RP-1              wt%=100.0000  t,k= 288.150
oxid H2O(L)            wt%=  5.0000  t,k= 288.150
oxid H2O2(L)           wt%= 95.0000  t,k= 282.000

# You selected these options for output:
```

```
# short version of output
output short
# Proportions of any products will be expressed as Mass Fractions.
output massf
# Heat will be expressed as siunits
output siunits

# Input prepared by this script:/var/www/sites/cearun.grc.nasa.gov/cgi-bin/CEARUN/prepareInputFile.c

### IMPORTANT:  The following line is the end of your CEA input file!
end
```

A.2.3. RP-1 & 98% HTP

```
### CEA analysis performed on Mon 27-May-2024 11:49:49

# Problem Type: "Rocket" (Finite Area Combustor)

prob case=_____________5727 ro equilibrium    fac

!Contraction Ratio:
ac/at=12.25

# Pressure (11 values):
p,bar= 5, 5.5, 6, 6.5, 7, 7.5, 8, 8.5, 9, 9.5, 10
# Supersonic Area Ratio (1 value):
supar= 5

# Equivalence based on Fuel/Oxid. wt ratio (Eq 9.19*) (5 values):
phi= 0.9, 0.95, 1, 1.05, 1.1

# You selected the following fuels and oxidizers:
reac
fuel RP-1              wt%=100.0000  t,k= 288.150
oxid H2O(L)            wt%=  2.0000  t,k= 288.150
oxid H2O2(L)           wt%= 98.0000  t,k= 282.000

# You selected these options for output:
# short version of output
output short
# Proportions of any products will be expressed as Mass Fractions.
output massf
# Heat will be expressed as siunits
output siunits

# Input prepared by this script:/var/www/sites/cearun.grc.nasa.gov/cgi-bin/CEARUN/prepareInputFile.c
```

```
### IMPORTANT:  The following line is the end of your CEA input file!
end
```

A.3. Validation Setup

Below, additional data on the setup of the two validation cases is provided.

A.3.1. Case 1 Data

Parameter	Value
Performance	
Oxidizer	90 wt.% H2O2
Reactive fuel	Stock 2
Design thrust	500 N
Design chamber pressure	30 bar
Ideal vacuum specific impulse (Isp)	306.5 s
Ideal characteristic velocity (C□)	1579.2 m/s
Theoretical O/F ratio	5.48
Design oxidizer mass flow	131.4 g/s
Design fuel mass flow	24 g/s
Combustor	
Nozzle type	15° conical nozzle
Nozzle throat diameter	10.2 mm
Nozzle expansion area ratio	4
Chamber length without converging section	80.2 mm
Chamber diameter	32.5 mm
Converging angle	30°
Injector	
Injector type	Pentad unlike-impinging jets
Configuration of injection element	Single element (1 fuel orifice + 4 oxidizer orifices)
Impinging oxidizer jet angle	60°
Fuel orifice diameter	1.2 mm
Oxidizer orifice diameter	1.25 mm

Table A.1: Impinging-jet injector engine geometry and propellant parameters [51, 52]

A.3.2. Case 2 Data

Parameters	Value
Propellant	
Oxidiser	90% H2O2, 10% H2O
Fuel	CH3OH, Mn3O4
General	
Vacuum thrust	662.7848 N
Vacuum specific impulse	231 s
Chamber pressure	27.57904 bar
Characteristic velocity	1572.463 m/s
Characteristic length	751.84 mm
Mass flow rates	
Oxidiser	0.213642 kg/s
Fuel	0.078018 kg/s
O/F	2.74
Pintle	
Pintle diameter	9.525 mm
Pintle length	11.43 mm
Primary hole diameter	0.57912 mm
Secondary hole diameter	0.381 mm
Number of hole pairs	16
Fuel exit area	6.038698 mm^2
Fuel injection velocity	14.35608 m/s
Annulus	
Injector face hole diameter	10.5918 mm
Gap distance	0.5588 mm
Oxidiser exit area	17.29029 mm^2
Oxidiser injection velocity	8.65632 m/s
Chamber	
Chamber diameter	44.3484 mm
Chamber length	76.2381 mm
Wall thickness	6.35 mm
Nozzle	
Throat diameter	14.4526 mm
Throat area	163.8706 mm^2
Exit diameter	19.3675 mm
Exit area	294.8381 mm^2
Expansion ratio	1.799 -

Table A.2: Pintle-injector engine geometry and propellant parameters [53]

A.4. Final Simulation Setup

Setup

- **General**
  - Solver: Pressure-Based
  - Time: Transient
  - Gravity: On
- **Models**
  - Multiphase: Off

  - Energy: On
  - Viscous: SST k-omega
  - Reactions: Species Transport
    * Volumetric Reactions
    * Finite Rate/No TCI
    * Diffusion Energy Source
  - Discrete Phase: On
    * Interaction with Continuous Phase
    * Update DPM Source Every Flow Iteration
    * Pressure Dependent Boiling
    * Temperature Dependent Latent Heat
    * Breakup
    * Unsteady Particle Tracking
    * Consider Children in the Same Tracking Step
    * High-Res Tracking
    * Injections
      · Discrete Random Walk Model
      · Breakup: TAB
      · Diameter Distribution: rosin-rammler
      · Min Diameter: 1e-6 m
      · Mean Diameter: 1e-5 m
      · Max Diameter: 1e-4 m
      · Spread Parameter: 3.5
      · Number of Diameters: 10
      · Temperature: 300 K
      · Scale Flow Rate by Face Area
      · Inject Using Face Normal Direction

- **Materials**
  - Mixture (gas phase): Kerosene-Air
    * Species: c12h23, o2, co2, h2o, h2o2, n2
    * Reaction: finite-rate
    * Density: real gas PR
  - Droplet (DPM fuel injection): Kerosene
    * Species: c12h23<l>
  - Particle Mixture (DPM oxidiser injection): HTP

        * Species: h2o<l>, h2o2<l>

- **Operating Conditions**
  - Pressure: 101325 Pa
  - Temperature: 288.15 K
  - Gravity: -9.80665 m/s^2 (z-direction)
  - Real Gas State: Vapor
- **Cell Zone Conditions**
  - Material: Kerosene-Air
  - Reactions: On
- **Boundary Conditions**
  - Inlet
    * Fuel & Oxidiser, Continuous
      · Initial Gauge Pressure: 15e6 Pa
      · Acoustic Wave Model: Off
      · Total Temperature: 300 K
      · DPM BC Type: reflect
    * Fuel DPM Injection:
      · Material: kerosene-droplet
      · Velocity: 60 m/s
    * Oxidiser DPM Injection:
      · Material: HTP-mixture
      · Velocity: 45 m/s
  - Outlet: Pressure Outlet
    * Acoustic Wave Model: Off
    * Backflow Total Temperature: 288.15 K
    * Backflow Species Mass Fractions: o2: 0.21, n2: 0.79
    * DPM BC Type: escape
  - Wall: Stationary Wall, No Slip, Standard Roughness
    * Heat Flux: 0
    * Wall Thickness: 0.005 m
    * Material: aluminum (injector plate), uhtcmc (others)
    * DPM BC Type: reflect

Solution

- **Methods**
  - Pressure-Velocity Coupling: SIMPLE
  - Gradient: Least Square Cell Based
  - Pressure: PRESTO!
  - Density: Second Order Upwind
  - Momentum: Second Order Upwind
  - Turbulent Kinetic Energy: Second Order Upwind
  - Specific Dissipation Rate: Second Order Upwind
  - Species: Second Order Upwind
  - Energy: Second Order Upwind
  - Pseudo Time Method: Off
- **Controls** (Under-Relaxation Factors)
  - Pressure: 0.3
  - Density: 0.9
  - Body Forces: 1
  - Momentum: 0.7
  - Turbulent Kinetic Energy: 0.8
  - Specific Dissipation Rate: 0.8
  - Turbulent Viscosity: 1
  - Species: 0.9
  - Energy: 0.7
  - Discrete Phase Sources: 0.9
- **Calculation Activities** (Time-Step)
  - Type: Fixed
  - Size: 0.001 s

A.5. Transient Contours

Shown below are animated contours for Static Temperature (Figure A.1), Absolute Static Pressure (Figure A.2) and Velocity Magnitude (Figure A.3) for the final simulation of the case with $\alpha = 98\%, \Phi = 1.0$. Playing the sequence is possible for example with the free Adobe Acrobat Reader. Simulation time step is $\Delta t = 1ms$. In the animations, each time step is displayed for $100ms$. Total simulation run time is $60ms$, hence animation run time is $6s$.

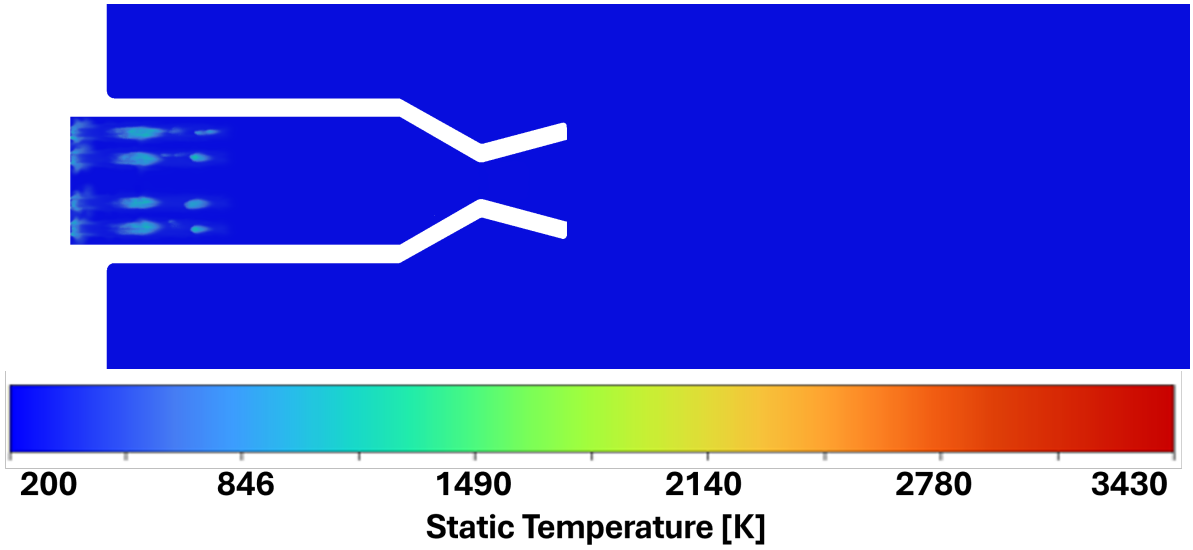

Figure A.1: Static Temperature Contour (animated)

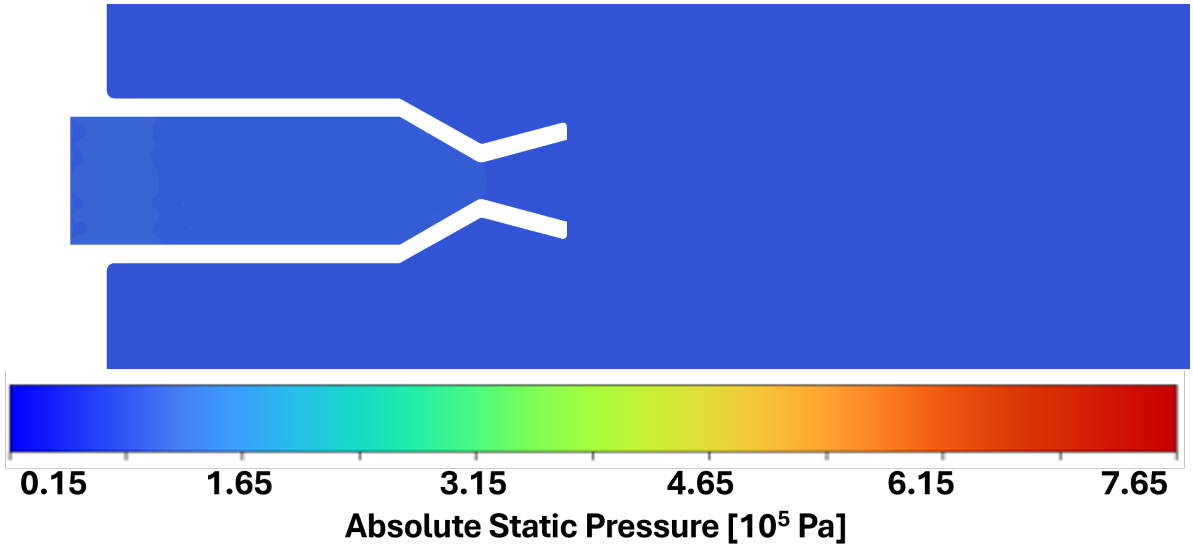

Figure A.2: Absolute Static Pressure Contour (animated)

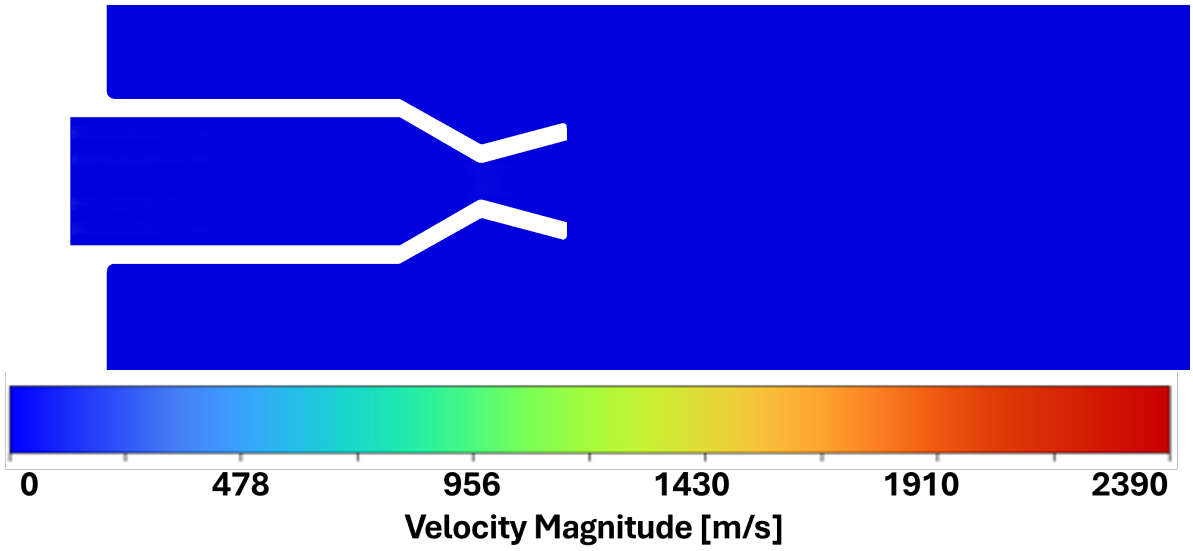

Figure A.3: Velocity Magnitude Contour (animated)